

MICRO/NANOSCALE TRIBOLOGY OF LINEAR TAPE DRIVES

DISSERTATION

Presented in Partial Fulfillment of the Requirements for
the Degree Doctor of Philosophy in the Graduate
School of The Ohio State University

By

Anton Viktorovich Goldade, M.S.

* * * * *

The Ohio State University

2003

Dissertation Committee:

Professor Bharat Bhushan, Adviser

Professor Donald R. Houser

Professor Anthony F. Luscher

Approved by

Adviser
Department of Mechanical Engineering

ABSTRACT

To increase storage capacity, future high performance linear tape systems will require the use of smoother and thinner magnetic tapes, lower head-tape spacing, lower track width, and higher track densities. In the case of magnetic tapes, smoother surfaces lead to increased static/kinetic friction, and low flying heights lead to partial contact between the head and the tape both of which result in the head and the media degradation and failure due to tribological aspects. Miniaturization of magnetic recording heads requires better understanding of wear mechanisms on a nanometer size scale. Better tape guiding and tape dimensional stability is needed for better tracking performance as track widths are reduced and track densities are increased. Higher track density necessitates the use of narrower data tracks that are placed closer to the tape edge; tape edge damage becomes a concern. During drive operation, damage to the tape edge may result in tape dimensional changes, leading to problems in tracking, generation of loose tape debris, which may show up at the head-tape interface and cause signal loss.

An attempt is made to employ micro/nanotribological techniques to detect wear precursors for the tape head materials. Nano-Kelvin probe is used to detect changes (structural and/or chemical) occurring at the surface top most layers under wear at ultra low loads, which precede appearance of wear debris and/or measurable wear scars.

The effect of environmental conditions on the durability of the head-tape interface is studied for a commercial tape drive with a magnetoresistive head and belt driven cartridge loaded with metal particle tape. Possible failure mechanisms are discussed.

An increase in the pole tip recession (a spacing between a head and a tape) results in a signal loss in magnetic tape drives. Test results and analytical modeling suggest that three-body abrasion is the operative wear mode. We study three-body abrasion in detail, by injecting loose particles into the head-tape interface. An experimental setup has been developed. This study of the root cause provides some information about what ultimately needs to be controlled (particle size, concentration, hardness) to minimize pole tip recession.

The research also addresses tape guiding and associated tape edge damage by correlating the occurrence and severity of edge damage with the type of the guides, edge guiding forces, operating conditions and number of file passes. An experimental setup has been developed to measure tape displacement (tape lateral motion) perpendicular to the direction of tape motion and normal forces at the tape edge-flange interface. A methodology has been developed for evaluation of magnetic tape edge quality. The proposed methodology allows quantitative evaluation of the quality of tape edges.

Dedicated to my daughter

ACKNOWLEDGMENTS

I first thank my advisor for my Ph.D. degree, Professor Bharat Bhushan. He provided tools, resources, his expertise, and moral support which were all essential to the work reported in this dissertation. The experience I got under his guidance is one can dream about. I thank Professor Donald Houser and Professor Anthony Luscher for serving on both my final and candidacy exam committees. I also appreciate the work that Professor Emeritus Bernard Hamrock has kindly performed as a member of my candidacy exam committee.

I would like to express my sincere gratitude to the colleagues and friends in the laboratory who offered many discussions that were helpful for this work. I thank Xiaodong Li, Huiwen Liu, William W. Scott, Teijin Ma, Sriram Sundararajan, and other friends. My special thanks are for Joseph West (ME), who always had a good piece of advice on electronics repair and circuitry development. Keith Rogers (ME) helped me a lot with machining parts, which I greatly appreciate. Cameron Begg and Hendrik Colijn (of CEOF in Material Science and Engineering) provided their know-how in scanning electron microscopy and Auger electron spectroscopy, respectively. I also thank Jerry Kingzett, Robert Frank, Gary Gardiner, and others in the ME Dept. for assistance in machining, equipment, and in fixing problems in the lab.

Our lab sponsors were also extremely helpful. Financial support for this study was provided in part by the membership of the Nanotribology Laboratory for Information Storage and MEMS/NEMS. Part of this research was supported by the Imation Corp.- Advanced Technology Program (Program Manager, Ted Schwarz, Peregrine Technology, St. Paul, Minnesota), National Institute of Science and Technology, as part of Cooperative Agreements 70NANB5H1116 and 70NANB2H3040. I express my gratitude to Richard E. Jewett of Imation Corp. for fruitful discussions throughout the study and for providing magnetic tape and head specimens. I express my gratitude to Steve Gavit of Segway Systems, LLC (Littleton, CO) for providing the tape drive with single flanged guides with porous air bearings. The financial support for part of the research was provided by the National Science Foundation (Contract No. ECS-9820022). The content of this information does not necessarily reflect the position of the U.S. Government, and no official endorsement should be inferred.

VITA

- October 7, 1971..... Born – Gomel, Republic of Belarus
- 1994.....M.S. Physics, St. Petersburg State Technical University,
St. Petersburg, Russia
- October 1994-June 1998.....Research Scientist, V.A. Biely Institute of Mechanics of
Metal-Polymer Systems, Gomel, Belarus
- June 1998 – present.....Graduate Research Associate, The Ohio State University

PUBLICATIONS

1. Chizhik, S. A., Goldade, A. V. and Myshkin, N. K. (1998), “Levels of Topography in Mechanics of Precision Joints,” *International Journal of Machine Tools & Manufacture*, **38**, 495-502.
2. Chizhik, S. A., Goldade, A. V., Korotkevich, S. V. and Dubravin, A. M (2000), “Friction of Smooth Surfaces with Ultrafine Particles in the Clearance,” *Wear*, **238**, 25-33.
3. Bhushan, B. and Goldade, A. V. (2000), “Kelvin Probe Microscopy Measurements of Surface Potential Change Under Wear at Low Loads,” *Wear*, **244**, 104-117.
4. Bhushan, B. and Goldade, A. V. (2000), “Measurements and Analysis of Surface Potential Change during Wear of Single-Crystal Silicon (100) at Ultralow Loads using Kelvin Probe Microscopy,” *Applied Surface Science*, **157**, 373–381.
5. Amelio, S., Goldade, A. V., Rabe, U., Scherer, V., Bhushan, B. and Arnold, W. (2001), “Measurements of Mechanical Properties of Ultra-Thin Diamond-Like Carbon Coatings Using Atomic Force Acoustic Microscopy,” *Thin Solid Films*, **392**, 75-84.
6. Goldade, A. V. and Bhushan, B. (2002), “Effect of Operating Environment on Failure Mechanism of a Head-Tape Interface in a Linear Tape Drive with a Belt-Driven

Cartridge,” Proceedings of Institution of Mechanical Engineers. Part J: Journal of Engineering Tribology, **216**, 159-176.

7. Goldade, A. V. and Bhushan, B. (2002), “Effect of Particulate Contamination on Pole Tip Recession in a Linear Tape Drive,” Tribology Letters, **12**, 235-245.

8. Goldade, A. V. and Bhushan B. (2002), “Measurement and Origin of Tape Edge Damage in a Linear Tape Drive,” Tribology Letters, **14**, 167-180.

9. Reinstädler, M., Rabe, U., Scherer, V., Hartmann, U.; Goldade, A.; Bhushan, B., Arnold, W. (2003), “On the nanoscale measurement of friction using atomic-force microscope cantilever torsional resonances,” Applied Physics Letters, **82**, 2604-2606.

10. Goldade, A. V. and Bhushan B. (2003), “Tape Edge Study in a Linear Tape Drive with Single Flanged Guides,” Journal of Magnetism and Magnetic Materials, (submitted for publication).

FIELDS OF STUDY

Major Field: Mechanical Engineering

TABLE OF CONTENTS

Abstract.....	ii
Acknowledgments.....	v
Vita.....	vii
List of Tables	xii
List of Figures.....	xiii
Chapters:	
1 Introduction.....	1
1.1 Objectives of research and overview of research efforts	3
2 Kelvin Probe Microscopy measurements of surface potential change under wear at low loads	4
2.1 Introduction.....	4
2.2 Principles of the Kelvin probe microscope.....	6
2.3 Experimental details.....	10
2.3.1 Experimental technique	10
2.3.2 Test specimens.....	13
2.3.3 AES analysis	15
2.4 Results and discussion	15
2.4.1 Influence of interleave scan parameters on surface potential measurements.....	15
2.4.2 Silicon and silicon lubricated with fully bonded Z-DOL	19
2.4.2.1 Wear mechanisms of silicon at ultralow loads	27
2.4.3 Gold.....	28
2.4.4 Aluminum	30
2.4.5 Alumina.....	30
2.4.6 Some explanations for the sign of surface potential	33
2.5 Summary	33
3 Effect of Operating Environment on Failure Mechanism of a Head-Tape Interface in a Linear Tape Drive with a Belt Driven Cartridge	35
3.1 Introduction.....	35
3.2 Experimental details.....	38
3.2.1 Experimental apparatus and procedure.....	38
3.2.2 Operating envelope	42

3.2.3	Analysis of heads and tapes	45
3.2.4	Head and tape specimens	47
3.3	Experimental results and discussion	50
3.3.1	Tests at ambient conditions	50
3.3.1.1	Tests run continuously at ambient conditions	50
3.3.1.2	Test with intermittent stops at ambient conditions	56
3.3.2	Tests performed at extreme operating conditions	59
3.3.2.1	Test at 10° C and 20% RH	64
3.3.2.2	Test at 10° C and 80% RH	66
3.3.2.3	Test at 30° C and 80% RH	67
3.3.2.4	Test at 45° C and 20% RH	69
3.4	Discussion of environmental effects	71
3.5	Summary	75
4	Effect of Particulate Contamination on Pole Tip Recession in a Linear Tape Drive	76
4.1	Introduction	76
4.2	Experimental	80
4.2.1	Test apparatus and procedures	80
4.2.2	Test specimen	84
4.2.3	Analysis of the worn heads	85
4.3	Results and discussion	86
4.3.1	Airborne particulate contaminants	86
4.3.2	Effect of particulate contamination on PTR	89
4.3.2.1	Effect of particle concentration	91
4.3.2.2	Effect of particle size	94
4.3.2.3	Effect of particle hardness	95
4.3.3	Comparison with analytical model	96
4.3.4	Mechanism of PTR with contaminant particles from the environment	100
4.4	Summary	101
5	Measurement and Origin of Tape Edge Damage in a Linear Tape Drive	102
5.1	Introduction	102
5.2	Experimental details	104
5.2.1	Description of tape transport and test procedure	104
5.2.2	Measurement techniques	109
5.2.3	Head and tape specimens	112
5.3	Results and discussion	114
5.3.1	Wear tests	114
5.3.2	Analysis of tape edge degradation	119
5.3.3	Origin of tape edge damage	130
5.4	Summary	132

6	Tape Edge Study in a Linear Tape Drive with Single Flanged Guides	134
	6.1 Introduction.....	134
	6.2 Experimental details.....	137
	6.2.1 Description of tape transport.....	137
	6.2.2 Measurement techniques.....	139
	6.2.3 Test procedure.....	144
	6.2.4 Tape edge analysis.....	145
	6.2.5 Head and tape specimens	149
	6.3 Results and discussion	149
	6.3.1 Effect of tape path geometry during short term tests.....	150
	6.3.1.1 Single flanged vs. dual flanged guides	150
	6.3.1.2 Effect of head orientation.....	153
	6.3.1.3 Different cartridges and reel locations.....	156
	6.3.1.4 Effect of speed and tension.....	160
	6.3.2 Changes in LTM during long term testing.....	160
	6.3.2.1 Effect of speed and tension.....	160
	6.3.2.2 Effect of edge quality of factory-slit tapes.....	165
	6.3.2.3 Effect of tape thickness.....	172
	6.4 Summary.....	174
7	Conclusions.....	175
	7.1 Kelvin Probe Microscopy measurements of surface potential change under wear at low loads	175
	7.2 Effect of operating environment on failure mechanism of a head-tape interface	176
	7.3 Effect of particulate contamination on pole tip recession.....	176
	7.4 Tape edge studies.....	177
	References.....	179
	Appendices:	
	Appendix A Tape edge quality measurement methodology.....	184
	Appendix B Tape cupping measurements	190

LIST OF TABLES

Table		
2.1	Comparison of EWF of samples studied against the Co/Cr coated tip and measured surface potential (reversed bias voltage applied to the tip).....	14
3.1	Roughness statistics of virgin MP tape measured using an AFM (10×10 μm). Roughness data are based on five sets of measurements.....	48
3.2	Roughness statistics of virgin and worn MP tape measured using an AFM (80×80 μm). Roughness data are based on five sets of measurements.....	54
3.3	Summary of the measured read head recession, and calculated and measured separation loss.....	64
4.1	Particles used in the study.....	83
4.2	Model parameters for derivation of curves in Fig. 4.8.	98
5.1	Tape width measurement data for unworn and worn tapes. Each number represents an average of 300 measurements obtained over a 3 mm tape length. The width was measured at three different locations for both unworn tape and tape worn for 5000 cycles.	118
5.2	Number of pixels constituting edge damage. Optical micrographs of 112 μm along length (640 pixels) and 11.2 μm along width (64 pixels) were analyzed. Most of the damage occurs in the 0.5 μm (magnetic coating, lower edge) to 3-5 μm (backcoat, both edges) region from the edge. The number of pixels is based on ten measurements of each view.	128

LIST OF FIGURES

Figure		
2.1	Energy diagrams for electrons in two metal plates (M1 and M2) separated by a small vacuum gap, E_{F1} and E_{F2} are the Fermi energy levels, E_{vac} is the surface potential barrier, (a) metal plates are isolated, and (b) plates are connected electrically and charged.	8
2.2	(a) Electrostatic potential and interaction force between a conducting tip and a sample (for illustration assume that $\phi_{tip} > \phi_{sample}$), (b) external DC voltage applied to nullify the force, and (c) external AC voltage with adjustable DC offset is applied to the tip which leads to its vibration.	8
2.3	(a) Topography measurements in tapping mode. The cantilever is vibrated by a piezo at the resonant frequency of its free vibrations. Feedback adjusts tip-surface separation to maintain constant amplitude. The feedback output is recorded by the computer and becomes the surface height map. (b) Surface potential measurements during interleave scan in lift mode. The cantilever is scanned across the surface at a constant height. An oscillating voltage is applied to the tip. The KPM feedback adjusts DC bias to nullify vibration amplitude at the operating frequency. The nano-Kelvin probe feedback output is recorded by the computer and by reversing the sign becomes the surface potential map.	12
2.4	(a) Surface height map and surface potential map of wear mark on single crystal silicon measured at different lift scan height (tip-sample separation) and constant (5 V) AC voltage applied to the tip, and (b) change in surface potential as a function of interleave scan parameters.	16
2.5	(a) Surface height and surface potential maps of wear regions, and effect of number of cycles on (b) wear depth and (c) change in surface potential for single crystal silicon.	20
2.6	(a) Surface height and surface potential maps of wear regions, and effect of number of cycles on (b) wear depth and (c) change in surface potential for single crystal silicon lubricated with fully bonded Z-DOL.	22

2.7	AES spectra for (a) silicon and (b) silicon lubricated with fully bonded Z-DOL.....	26
2.8	(a) Effect of load on wear depth and change in surface potential for gold film deposited on single crystal silicon, and (b) surface height and surface potential maps of wear regions.....	29
2.9	(a) Effect of load on wear depth and change in surface potential for aluminum, and (b) surface height and surface potential maps of wear regions.....	31
2.10	Surface height and surface potential maps of wear regions on alumina sample at different loads.....	32
3.1	Schematic of the experimental apparatus.....	39
3.2	Number of dropouts per minute as a function of number of cycles for the test performed at 22°C and 45 % RH. The frequency of the symbols on all graphs for the class with the duration of greater then 12 μ s is less then the actual number of the data points.....	43
3.3	Environmental operating conditions used in the study.....	44
3.4	(a) Schematic and (b) optical micrograph of the thin-film region of the unworn MR head.....	49
3.5	AFM images of the unworn tape.....	49
3.6	(a) Head output, coefficient of friction, and number of dropouts per minute (> 12 dB, 6-9 μ s) as a function of number of cycles for the test performed at 22 °C and 45 % RH. (b) Head output, coefficient of friction, and number of dropouts per minute as a function of number of cycles for another test performed at 22 °C and 45 % RH showing reproducibility of the results. (c) Data at an expanded scale for the first 2500 cycles from (a).	51
3.7	(a) AFM analysis (averaged cross sections and the gray scale AFM images) of the thin-film region of the MR head before and after the test performed at 22 °C and 45 % RH. Vertical scale from black to white is 200 nm. Brighter areas correspond to higher points. (b) AES analysis of virgin head and the head worn for 10000 cycles at 22° C and 45% RH.....	55

3.8	(a) Read head recession as a function of number of cycles of the head used in the test with intermittent stopping performed at 22 °C and 45 % RH; (b) optical micrographs of the thin-film region; and (c) the averaged cross sections and the gray scale AFM images of the thin-film region. Vertical scale from black to white is 200 nm. Brighter areas correspond to higher points.	57
3.9	Head output, coefficient of friction, and number of dropouts per minute (> 12 dB, 6-9 μs) as a function of number of cycles for the tests performed at extreme operating conditions.	60
3.10	AFM analysis (averaged cross sections and gray scale AFM images) of the thin-film region of the MR head before and after the tests performed at extreme operating conditions. Vertical scale from black to white is 200 nm. Brighter areas correspond to higher points.	61
3.11	Optical images of different regions of worn tape heads.	62
3.12	AFM images of the unworn and worn MP tape.	63
3.13	Head output and the number of dropouts per minute (6-9 dB, 3-6 μs) as a function of number of cycles for the test performed at 30 °C and 80 % RH.	68
3.14	Head output, coefficient of friction and the number of dropouts per minute (> 12 dB, 6-9 μs) as a function of number of cycles for all tests.	72
3.15	Durability of the tests, the range of variation for head output and coefficient of friction, and the change in the read head recession during the tests performed at different environmental conditions.	73
3.16	AFM images of the head air-bearing surface at the end of the tests performed at different environmental conditions after cleaning with a dry cotton swab.	74
4.1	Cross-section schematic of a thin-film inductive tape head showing the definitions of PTR and overcoat recession.	77
4.2	Schematic of the experimental setup.	81
4.3	Optical micrograph and AFM image of the thin-film structure of the heads used in the study. The transition from black to white in the AFM image covers height range of 100 nm. Brighter areas correspond to higher points.	85

4.4	Number of airborne particle versus time: (a) in laboratory environment; (b) in laboratory environment and during flushing by clean air; (c) for a period before head-tape contact, followed by two hour long period of head-tape contacts, and followed by a period of no head-tape contact.	87
4.5	PTR vs. sliding distance. (a) Summary of the wear tests performed and 2-dimensional AFM scans across the thin-film region for the test performed in class 10,000 laboratory environment; (b) effect of contaminant particle concentration, size, and hardness on PTR.	90
4.6	Secondary electron SEM images of the tape heads run in the wear tests with different contaminant particles: (a) thin-film region; (b) pole pair at high magnification.	92
4.7	AFM images of the tape heads run in the wear tests with different contaminant particles and 2-dimensional AFM scans along the pole. The transition from black to white in the gray scale image covers height range of 100 nm. Brighter areas correspond to higher points.	93
4.8	Results generated by the model showing the effect of particle size and thin-film wear coefficient. Model parameters are listed in Table 4.2.	99
4.9	Schematic showing head-tape interface with large and small particles entrapped. Large particles lift the tape.	100
5.1	(a) Schematic of the tape transport, (b) Schematic showing details of the tape lateral motion measurement technique, (c) Schematic showing details of the lateral force measurement technique, and (d) Cross-sections of the guide used in wear tests and for force measurements.	105
5.2	Definition of tape edge views used for imaging. (b) Sample optical micrographs illustrating edge quality measurement technique.	110
5.3	(a) General view and thin-film region of the tape head. (b) Schematic diagram of MP tape.	113
5.4	Variation of head output, number of dropouts per minute, coefficient of friction, and tape lateral motion peak-to-peak amplitude as a function of number of cycles.	115
5.5	Cupping of the unworn tape and after use in tape drive. Magnetic coating is at the bottom (negative cupping).	119

5.6	Optical analysis of degradation of tape edge under normal drive operation. Examples of cracks, tears and scratches are shown in the figure for clarity.	121
5.7	AFM analysis of degradation of the tape edge under normal drive operation. Surface profiles presented in (a) were measured along one scan line and in (b) were average over the entire scan. An example of the ridge and an isolated island are shown in the figure for clarity.....	122
5.8	SEM analysis of degradation of tape edge under normal drive operation.	126
5.9	Variation of (a) lateral force and (b) tape lateral motion during one cycle. Both measurements were performed at location “Cantilever beam” shown in Fig. 5.1 (a) near the modified guide B.	129
5.10	Schematic showing formation of tape edge during slitting and after drive use.	131
6.1	(a) Schematic of the tape transport. (b) Origin of downward force.	138
6.2	Schematics showing details of (a) lateral tape motion measurement technique, (b) lateral force measurement technique, and (c) friction force measurement and free-body diagrams of tape. (d) Lateral force measurement.	140
6.3	(a) Definition of tape edge views used for imaging. Sample optical micrographs illustrating edge quality measurement technique: (b) unworn tape and (c) tape worn for 5000 cycles.	146
6.4	(a) General view and thin-film region of the tape head. (b) Schematic diagram of MP tape.	150
6.5	(a) Comparison of guiding performance of drives with different guide types. (b) Effect of tape path geometry (head zenith and wrap angles) on lateral tape motion peak-to-peak amplitude and lateral (guiding) force at 1 N and 4 m/s. (c) Power spectral density of the lateral tape motion. Transition from black to white on the spectral map covers range from $10^{-5} \text{ nm}_{\text{peak}}^2/\text{Hz}$ to $1 \text{ nm}_{\text{peak}}^2/\text{Hz}$ in logarithmic scale. Brighter areas correspond to higher values of power spectral density.....	151
6.6	LTM variation versus cartridges, radial reel locations and edge quality of unworn tape at 1 N and 4 m/s. The relative edge contour length was averaged over four tape edges for each tape sample.	157

6.7	(a) Sample optical micrographs of unworn tape edges from two different cartridges. (b) Tape edge statistics. Optical micrographs of 112 μm along length (640 pixels) and 11.2 μm along width (64 pixels) were analyzed. MC - magnetic coating, BC - backcoat.....	158
6.8	Effect of tape tension and speed on lateral tape motion peak-to-peak amplitude and coefficient of friction.....	161
6.9	Variation of lateral tape motion peak-to-peak amplitude and coefficient of friction as a function of number of cycles. Effect of (a) tape speed and (b) tape tension.....	162
6.10	Sample optical photographs taken at the end of testing showing formation of staggered layers at high tape speed.....	164
6.11	Effect of edge quality of factory-slit tape on lateral tape motion during long term wear tests. (a) Variation of lateral tape motion peak-to-peak amplitude as a function of number of cycles for two tapes with different initial edge quality. (b) Tape edge statistics. Optical micrographs of 112 μm along length (640 pixels) and 11.2 μm along width (64 pixels) were analyzed. MC - magnetic coating, BC - backcoat. (c) AFM maps and SEM images of tape edge (edge view). Surface profiles presented for AFM images were averaged over the entire scan. (d) Measured cupping profiles at 0 N and 1 N tensions. Magnetic coating is at the bottom (negative cupping). (e) Head contamination close to tape edges after 5000 cycles.....	166
6.12	(a) Variation of lateral tape motion peak-to-peak amplitude as a function of number of cycles for thin media. (b) Tape edge statistics. Optical micrographs of 112 μm along length (640 pixels) and 11.2 μm along width (64 pixels) were analyzed. MC - magnetic coating, BC - backcoat.....	173
A.1	Definition of tape edge views.....	185
A.2	Sample optical micrographs, AFM maps and SEM images of tape edges.....	185
A.3	Sample optical micrographs illustrating edge quality measurement technique: (a) unworn tape and (b) tape worn for 5000 cycles.....	187
A.4	Sample optical micrographs of tape edges and tape edge statistics for two tapes with different edge quality.....	189
B.1	Sample cupping profiles. Magnetic coating is at the bottom.....	191

CHAPTER 1

INTRODUCTION

According to some estimates, 95% of information today is stored on paper, 3% on microfiche, and only 2% on magnetic/optical and semiconductor storage devices.

Magnetic storage devices include hard disk, flexible disk, and tape drives. Estimate for worldwide storage is 12,000 petabytes (12 million terabytes). It is estimated that magnetic tapes store about 95% of the information, and the balance is stored equally by magnetic hard disk and optical disk drives [Bhushan, 2000]. Magnetic recording devices are commonly used to store large amounts of information in a nonvolatile manner for audio, video and digital applications. The types of magnetic media for digital recording are: flexible media (tapes and floppy disks) and rigid disks. Some of the advantages of the tape media are the low cost per megabyte of the stored information, high volumetric density, and portability of the media. Tape drives are primarily used to store and archive information on the order of terabytes, which imposes strict requirements on the high reliability and excellent performance of both drives and tapes.

The requirements for high-quality information storage system are virtually error-free recording and faithful reproduction of the recorded signal. Both magnetic recording and retrieval processes are accomplished by relative motion between a magnetic head and

a magnetic medium, which raises a number of tribological issues. Need for a high linear storage density requires that the surfaces be as smooth as possible and flying heights be as low as possible [Bhushan, 1996, 2000]. In the case of magnetic tapes, smoother surfaces lead to increased static/ kinetic friction, and low flying heights lead to partial contact between the head and the tape both of which result in head and media degradation (wear) and failure due to tribological aspects. Numerous factors contribute to signal reproduction. In linear and rotary head tape drives, with particulate and metal evaporated media tribological aspects such as adhesion and friction at the head-tape interface, and differential wear of the head were found to be responsible for the generation of the loose debris, the formation of the head stains, and pole-tip recession (PTR), resulting in signal degradation and causing errors during the signal reproduction [Bhushan and Hahn, 1995; Patton and Bhushan, 1997a; Scott and Bhushan, 1999a, 1999b, 2000].

In order to achieve high volumetric storage density thinner media, narrower tracks and thus smaller head dimensions (on the order of a hundred microns), and higher track densities are used. The latter is achieved by the usage of multichannel heads and by moving head along the tape width. With the track widths reducing, better tape guiding and tape dimensional stability is needed for better tracking performance [Bhushan, 2000]. Lateral (cross-track) motion of the tape can cause the desired data track to move away from the magnetic head and cause a so-called track misregistration (TMR) error. Consequently, tape lateral motion needs to be minimized. Higher track density necessitates the use of narrower data tracks that will be placed closer to the tape edge; tape edge damage becomes a concern. During drive operation, damage to the tape edge

may result in tape dimensional changes, leading to problems in tracking, generation of loose tape debris, which may show up at the head-tape interface and cause signal loss.

1.1 Objectives of research and overview of research efforts

This research is aimed at evaluation of the tribological and magnetic performance of the head-tape interface of a linear tape drive as well as tape guiding and associated tape edge damage. The research activities will allow us to better understand basic tribological issues of the interface and work out guidelines and recommendations for the improvement of the existing and development of the future products. The approach is based on experimental studies of head-tape interface performance using both commercial tape drives and advanced tape transports. It also employs nanotribological techniques to provide the insight into the mechanisms responsible for the performance degradation.

Chapter 2 describes a study of wear precursors (precursors to measurable wear) by means of Kelvin probe microscopy, an atomic force microscopy based technique, on nanoscale. Effect of operating environment (temperature and humidity) on long-term tribological and magnetic performance and the effect of airborne contaminations on wear of tape heads is studied in Chapters 3 and 4, respectively. Chapter 5 describes a methodology for evaluation of tape edge. This methodology is applied to study the origin of the tape edge damage during factory slitting and to monitor degradation of the tape edges during normal drive operation to reveal wear mechanisms. Tribological and guiding performance of single flanged guides with porous air bearings is evaluated in Chapter 6. Chapter 7 summarizes the conclusions drawn from the study.

CHAPTER 2

KELVIN PROBE MICROSCOPY MEASUREMENTS OF SURFACE POTENTIAL CHANGE UNDER WEAR AT LOW LOADS

2.1 Introduction

Miniaturization in the magnetic recording industry and rapid developments in the microelectromechanical systems (MEMS) industry require better understanding of wear mechanisms on a nanometer size scale. The interaction of the moving parts of MEMS or slider-disk interaction in magnetic disk drives under normal operating conditions leads to physical and chemical changes of interfacial surfaces. It is desirable to detect these changes at very early stages in order to understand the mechanism of failure initiation. The electronic work function is one of the material properties sensitive to both physical and chemical conditions of the surface. It is sensitive to almost all processes which occur during the rubbing of metallic and semiconductor surfaces.

The contact potential difference or simply surface potential between two surfaces is the potential difference arising between them as they are brought together in electrical contact and thermodynamic equilibrium is achieved. The contact potential difference (CPD) between two materials depends on a variety of parameters such as electronic work function (ϕ), adsorption, oxide layers, and dopant concentration in semiconductors. In a

simple model the contact potential between two materials is equal to the difference of the electronic work functions of the conductors including charges due to adsorption layers on the surface divided by the magnitude of the charge of one electron.

Since 1898, a Kelvin probe based on capacitor plates has been used for CPD measurements [Kelvin et al., 1898]. This was modified later by employing vibrating capacitor plates [Zisman, 1932]. Baumgärtner and Liess [1988] developed a miniaturized Kelvin probe with a lateral resolution of 40 μm ; this allowed microscopic imaging of the difference of the work functions between the Kelvin probe and a sample.

Scanning probe microscopy (SPM), first developed by Binnig and Rohrer [1982], provided the ability to measure material properties with high spatial resolution. The principle of operation of an atomic force microscope (AFM), a family of SPM, is based on detecting a minute force between the sample and the scanning tip attached to a small cantilever. Martin et al. [1988] and Weaver and Abraham [1991] demonstrated the usefulness of atomic force microscopy for imaging surface dielectric properties and for potentiometry through the detection of electrostatic forces. This was followed by several researchers such as Nonnenmacher et al. [1991] and Jacobs et al. [1997], who reported measurements of the surface potential between different materials using scanning probe microscopy with high lateral (< 50 nm) and surface potential (better than 0.1 mV) resolution.

The Kelvin technique for measuring contact potential differences has been adapted for monitoring tribological changes taking place during operation of magnetic recording media [Zanoria et al., 1995; Novotny et al., 1997]. The Kelvin technique can be used to investigate tribological materials for a wide range of conditions and provides a

method for continuous non-destructive monitoring of changes in the work function of a rubbing surface that is sensitive to various events which accompany friction and wear [Zharin and Rigney, 1998].

DeVecchio and Bhushan [1998] were first to develop a Kelvin probe microscope (KPM, also referred to as nano-Kelvin probe) for detecting wear precursors (precursors to measurable wear) that precede wear debris and/or measurable wear scars at very low loads. The technique was based on atomic force microscopy (AFM) and allowed mapping of surface potential simultaneously with topography measurements. It was shown that even in the cases where there was little or no damage to the surface, as observed by the topography scans of an AFM, there was a change in surface potential of the sample. On the basis of data obtained the authors concluded that the change in surface potential during friction and wear at ultralow loads might be due to chemical and structural changes in the first few nanometers of the sample.

This study discusses recent results, leading to improved understanding of the KPM technique itself and the changes which occur at early stages of wear. The influence of the KPM operating parameters on the measured change in surface potential and the reproducibility of the experimental results are investigated. The effect of load and number of cycles at very low loads on surface potential change has been studied. Mechanisms that may be responsible for the change in surface potential are discussed.

2.2 Principles of the Kelvin probe microscope

Let us consider two metal plates separated by a small vacuum gap. The energy diagram is presented in Fig. 2.1 (a). The Fermi energy level (E_F) is the kinetic energy of the most energetic electron at the absolute zero of temperature [Condon and Odishaw,

1967; Michels et al., 1968]. The free electrons in a metal are prevented from escaping from it by electrical forces, which give rise to a surface potential barrier. The electronic work function is the energy required for removing an electron from the metal; it is determined as the difference between the Fermi energy level of a metal and the energy of the free electron in vacuum (E_{vac}). When the two plates are connected electrically, thermodynamic equilibrium is achieved when the Fermi energy levels for the two metal plates are equal (Fig. 2.1 (b)). Electrons just outside the metal surfaces have different potentials since the equality of the Fermi levels is obtained by the flow of electrons from the plate with the lower work function (metal 1) to that with the higher one (metal 2). The first metal surface is charged positively and the second is charged negatively. The difference in the two potentials, known as the contact potential difference (or surface potential) $\Delta\Phi$, is the difference between the work functions of the metals, divided by the magnitude of the charge of one electron. If an external compensating potential is used to establish the equilibrium of the surface potential barrier, this external potential will be equal in magnitude, but opposite in sign to the contact potential difference. If the work function of one of the plates can be maintained constant (reference surface), the changes in the work function of the other plate will manifest themselves as a change in contact potential difference (referred to as change in surface potential). The change can be measured by detecting the charge flow between the plates of the capacitor [Kelvin et al., 1898; Zisman, 1932; Woodruff and Delchar, 1994].

Let us consider a conducting AFM tip and conducting sample with different work functions (Fig. 2.2 (a)). If the tip and the sample are electrically connected, electrons flow from the material with the smaller work function to the material with higher work

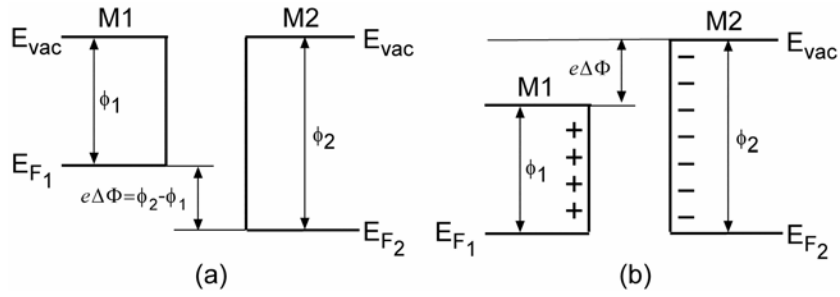


Figure 2.1: Energy diagrams for electrons in two metal plates (M1 and M2) separated by a small vacuum gap, E_{F1} and E_{F2} are the Fermi energy levels, E_{vac} is the surface potential barrier, (a) metal plates are isolated, and (b) plates are connected electrically and charged.

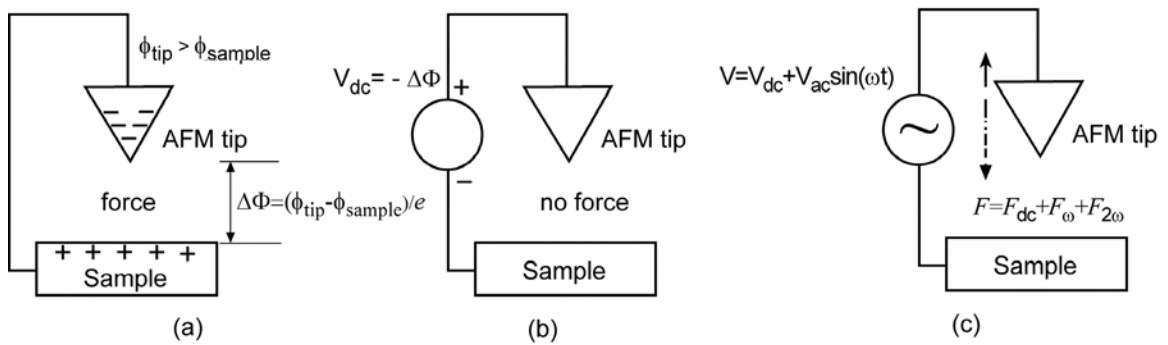


Figure 2.2: (a) Electrostatic potential and interaction force between a conducting tip and a sample (for illustration assume that $\phi_{tip} > \phi_{sample}$), (b) external DC voltage applied to nullify the force, and (c) external AC voltage with adjustable DC offset is applied to the tip which leads to its vibration.

function. This diffusion current builds up a double layer at the interface resulting in an electrostatic potential (contact potential difference) $\Delta\Phi$ given as

$$\Delta\Phi = (\phi_{\text{tip}} - \phi_{\text{sample}}) / e. \quad (2.1)$$

Any adsorption layers present on the surface would alter the charge and that would modify the measured $\Delta\Phi$.

Between the two bulk materials different surface potentials cause electrostatic forces due to the separation-dependent capacitance C between the tip and the sample. This force F takes the form of

$$F = \frac{1}{2} (\Delta\Phi)^2 \frac{\partial C}{\partial z}, \quad (2.2)$$

where z is the tip-sample distance. An external potential V can be applied to zero the force (Fig. 2.2 (b)). If an AC voltage, $V_{\text{ac}} \sin(\omega t)$ with adjustable offset V_{dc} is applied to the conducting AFM tip (Fig. 2.2 (c)) the electrostatic force interaction between the two electrodes (Eq. (2.2)) becomes

$$F = \frac{1}{2} \frac{\partial C}{\partial z} \{ \Delta\Phi + [V_{\text{dc}} + V_{\text{ac}} \sin(\omega t)] \}^2. \quad (2.3)$$

The spectral components at DC and frequencies ω and 2ω are

$$F_{\text{dc}} = \frac{1}{2} \frac{\partial C}{\partial z} \left\{ (\Delta\Phi + V_{\text{dc}})^2 + \frac{V_{\text{ac}}^2}{2} \right\}, \quad (2.4)$$

$$F_{\omega} = \frac{\partial C}{\partial z} (\Delta\Phi + V_{\text{dc}}) V_{\text{ac}} \sin(\omega t), \quad (2.5)$$

$$F_{2\omega} = -\frac{1}{4} \frac{\partial C}{\partial z} V_{\text{ac}}^2 \cos(2\omega t). \quad (2.6)$$

As a result of the F_ω and $F_{2\omega}$, the tip starts vibrating. If the frequency of the applied AC voltage equals the resonant frequency of the cantilever free vibrations, the vibration amplitude at frequency ω is directly proportional to the spectral component of electrostatic force at frequency ω [Sarid, 1994]. The tip vibration amplitude can be easily monitored during operation of the AFM. If the DC offset V_{dc} applied to the tip is equal in magnitude and opposite in sign to the contact potential difference $\Delta\Phi$ of the sample, the spectral components at frequency ω of the tip vibration amplitude, as well as of the force acting on the tip (see Eq. (2.5)) will become zero. The principle of operation of KPM is based on nullifying tip vibration amplitude at the resonant frequency by applying an adjustable DC voltage.

2.3 Experimental details

2.3.1 Experimental technique

All measurements were performed with a commercial AFM (NanoScope[®] IIIa MultiMode[™] with Extender[™] Electronics Module, Digital Instruments) in ambient air. The detailed description of the experimental procedure for measurement of surface potential change at initial stages of wear employing three modes of this microscope operation is presented by DeVecchio and Bhushan [1998].

Contact mode was used to abrade the specimen surface to simulate wear. The diamond tip used in these experiments was a three-sided pyramidal tip [Bhushan, 1999] with an apex angle of 60° and a tip radius of about 100 nm. The tip was attached to the stainless steel cantilever having a stiffness of 30 N/m. Wear marks $2 \times 2 \mu\text{m}$ were created at loads ranging from 1 μN to 30 μN depending on material hardness. A set of wear scars

at a distance of 10 μm from each other at constant load and different number of cycles or at varying load and one cycle was created to obtain one experimental curve. The scanning speeds of the tip during wear simulation were 4 $\mu\text{m/s}$ in the fast scan direction and 8 nm/s in the slow scan direction. Scanning speeds were increased up to 16 $\mu\text{m/s}$ in the fast scan direction and 32 nm/s in the slow scan direction when the effect of number of cycles on surface potential change was studied.

Mapping of the surface potential was made in the so-called "lift mode". These measurements were made simultaneously with the topography scan in the tapping mode (Fig. 2.3 (a)), using an electrically conducting tip. After each line of topography scan was completed, the feedback loop controlling the vertical piezo was turned off, and the tip was lifted from the surface and traced over the same topography at constant distance (lift scan height), (Fig. 2.3 (b)). During this "interleave" scan, a DC bias potential and an oscillating (AC) potential was applied to the tip. The frequency of oscillating potential (operating frequency) was chosen to be equal to the resonant frequency of cantilever free vibrations ($\sim 65\text{-}90$ kHz). The KPM feedback loop provided by the ExtenderTM Electronics Module was used to adjust the DC bias on the tip to nullify the force and hence the vibration amplitude of the cantilever at operating frequency (see Eq. (2.5)). The required bias voltage followed the localized potential of the surface and was recorded by the computer and by reversing the sign the surface potential map was obtained. It should be noted that some authors who use AFM based Kelvin probe microscopy use a different sign convention.

The tips used in these experiments were cobalt/chrome-coated tips (Digital Instruments, model MESP). KPM measurements were performed approximately 1 hour

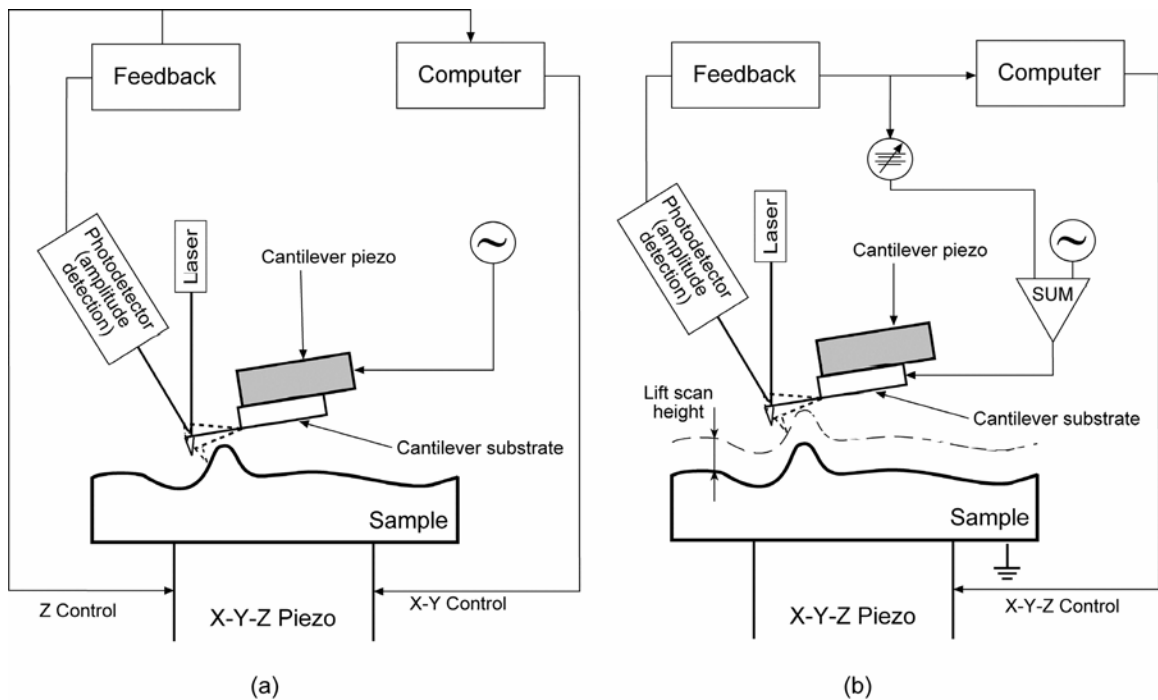


Figure 2.3: (a) Topography measurements in tapping mode. The cantilever is vibrated by a piezo at the resonant frequency of its free vibrations. Feedback adjusts tip-surface separation to maintain constant amplitude. The feedback output is recorded by the computer and becomes the surface height map. (b) Surface potential measurements during interleave scan in lift mode. The cantilever is scanned across the surface at a constant height. An oscillating voltage is applied to the tip. The KPM feedback adjusts DC bias to nullify vibration amplitude at the operating frequency. The nano-Kelvin probe feedback output is recorded by the computer and by reversing the sign becomes the surface potential map.

after the scars were created. On all the plots the change in surface potential between worn and unworn regions is shown. Measured wear depth and surface potential were averaged over an area of about $1.8 \times 1.8 \mu\text{m}$ in the center of the wear scars. The data presented on each graph were obtained with the same coated tip, unless otherwise mentioned.

2.3.2 Test specimens

Samples studied include single crystal silicon (100), single crystal silicon (100) lubricated with fully bonded Z-DOL (a perfluoropolyether), gold, aluminum, and alumina. Silicon samples were cut to a size of $10 \times 10 \text{ mm}$ from a silicon wafer of 1 mm thickness. Z-DOL (chemical structure $\text{HO-CH}_2\text{-CF}_2\text{-O-(CF}_2\text{-CF}_2\text{-O)}_m\text{-(CF}_2\text{-O)}_n\text{-CF}_2\text{-CH}_2\text{-OH}$, $m/n \sim 2/3$, molecular weight ~ 2000) is used for the boundary lubrication of magnetic disks as well as metal-evaporated magnetic tapes. Silicon samples were lubricated with fully bonded Z-DOL using the technique for lubrication of magnetic hard disks [Bhushan and Zhao, 1999]. The lubricant was measured with an ellipsometer to be 1 nm thick. Gold was chosen as an example of a noble metal. The gold film 110 nm thick was produced by sputter deposition onto a silicon substrate. The aluminum and alumina samples were mechanically lapped. For final lapping, $0.25 \mu\text{m}$ METADI[®] diamond paste (Buehler[®]) was used. For the aluminum sample, $0.06 \mu\text{m}$ MASTERMET[®] colloidal silica suspension in water base (Buehler[®]) was used. The RMS roughness of polished the aluminum and alumina samples as measured by an AFM were $15 \pm 5 \text{ nm}$ for a $10 \times 10 \mu\text{m}$ scan.

The samples were cleaned in ultrasonic baths with acetone and methanol for 20 minutes each and were kept at constant temperature of $22 \pm 1^\circ\text{C}$ and relative humidity (RH) of $45 \pm 5\%$. The measurements were performed in ambient air within 12 hours after

the samples were cleaned or lubricated. The electron work functions (EWF) for various samples and tip coating material are presented in Table 2.1 for later discussion.

Sample	EWF range (recommended) (eV) ^{a)}	$EWF_{\text{tip}} - EWF_{\text{sample}}$ (eV) ^{b)}	Measured surface potential for unworn region (V)	Sign of change in surface potential due to wear
Silicon	4.2 to 4.8 (4.8)	-0.3	-0.1 to -0.2	Negative
Gold	4.3 to 4.92 (4.3)	+0.2	+0.2	Positive
Aluminum	3.38 to 4.34 (4.25)	+0.25	-0.8	Negative
Alumina	4.7	-0.2	-	-
Tip coating				
Cobalt	3.90 to 5.44 (4.41)			
Chromium	3.72 to 4.7 (4.58)			

^{a)} Fomenko, 1966

^{b)} Recommended values for the sample were taken and average value of 4.5 eV for the probe was taken.

Table 2.1: Comparison of EWF of samples studied against the Co/Cr coated tip and measured surface potential (reversed bias voltage applied to the tip).

2.3.3 AES analysis

The single crystal silicon and single crystal silicon lubricated with fully bonded Z-DOL with wear marks were analyzed using Auger electron spectroscopy (AES) (Physical Electronics 680 scanning Auger nanoprobe) to detect elemental composition changes inside and outside the worn regions. AES spectra were obtained at an accelerating voltage of 10 kV and a probe current of 3.6 nA. A scan area of $0.8 \times 0.8 \mu\text{m}$ was rastered inside and outside wear marks with beam diameter of about 20 nm while the analyzer averaged over the area. An Auger spectrum of the virgin surface was first obtained and then the specimen surface was etched by using argon ions at beam energy of 2 keV with an etching rate of about 0.07 nm/s for 30 s and the spectra inside and outside the wear marks were taken.

2.4 Results and discussion

2.4.1 Influence of interleave scan parameters on surface potential measurements

The manufacturer of the microscope recommends using an initial set of parameters (lift scan height and amplitude of the AC voltage applied to the tip) for surface potential measurements during "interleave" scan. However, while running the experiments we found that the measured change in the surface potential is strongly affected by these parameters. We studied the influence of the lift scan height and the AC voltage applied to the tip on the measured change in surface potential. First, a wear mark was created on the silicon sample at 3 μN for 5 cycles. Then the surface potential map was obtained at different tip-sample separations (lift scan height was varied). Three images were captured with one tip and AC voltage set at 3V, 5V and 7V. The measurements were repeated for another tip. Examples of the experimental data are

shown in Fig. 2.4 (a). Fig. 2.4 (b) shows measured values of the change in surface potential as a function of interleave scan parameters. The absolute values of the measured change in surface potential decrease with increasing lift scan height (tip-sample distance) and change dramatically when the measurements are performed with different tips (the variation is 30-50%). The effect of the applied AC voltage is much less.

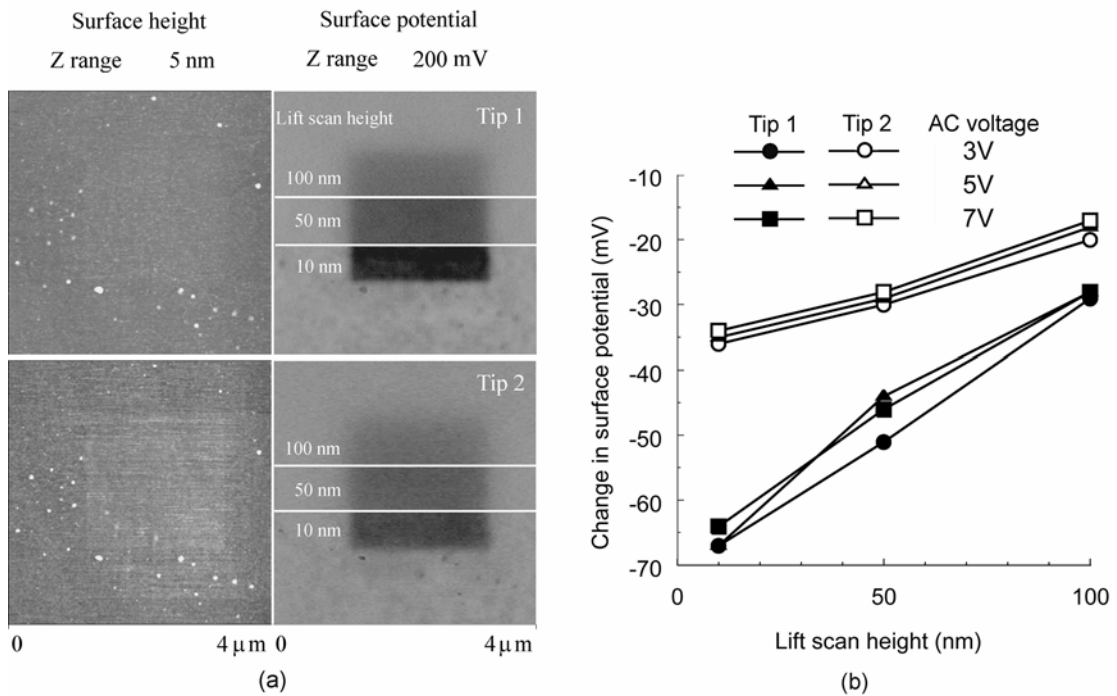


Figure 2.4: (a) Surface height map and surface potential map of wear mark on single crystal silicon measured at different lift scan height (tip-sample separation) and constant (5 V) AC voltage applied to the tip, and (b) change in surface potential as a function of interleave scan parameters.

In order to explain the variation in surface potential with changes in operating parameters (lift scan height, AC voltage) and the variations with the tip (chemical composition of the tip coating, tip shape), we examine their effect on the electrostatic force acting between the tip and the sample surface with n inhomogeneous regions, which is given by [Jacobs et al., 1998]

$$F_{\omega} = \sum_{i=1}^n \frac{\partial C_i}{\partial z} (\Delta\Phi + V_{dc}) V_{ac} \sin(\omega t), \quad (2.7)$$

where $\partial C_i/\partial z$ is the derivative of the capacitance between the tip and the area of the sample surface with the potential $\Delta\Phi_i$, V_{dc} and $V_{ac}\sin(\omega t)$ are the DC bias and oscillating potential applied to the tip. Obviously, for a homogeneous sample the measured potential (the signal provided by the KPM feedback) is equal in magnitude and opposite in sign to the surface potential, which is independent of the lift scan height and the tip shape. For an inhomogeneous sample, there are variations in surface potential on the sample surface. Since the capacitance between the probe and the sample and its derivative depend on the tip shape, the tip-sample separation (lift scan height) and the position of the tip over various regions on the sample surface, the measured potential is averaged over all potentials $\Delta\Phi_i$ on the surface, with the capacitance derivatives being the weighting factors [Jacobs et al., 1998; Yokoyama and Inoue, 1994]. In the present study, the sample surface is inhomogeneous due to the changes which occur during sliding. The measured change in surface potential is averaged over the unworn and worn areas of the sample surface and is affected by the lift scan height. Furthermore, the tips used are commercially available cobalt/chrome coated ones. The coating thickness, chemical

composition and tip shape can vary from one probe to another due to the coating deposition technique, which affects the measured change in surface potential.

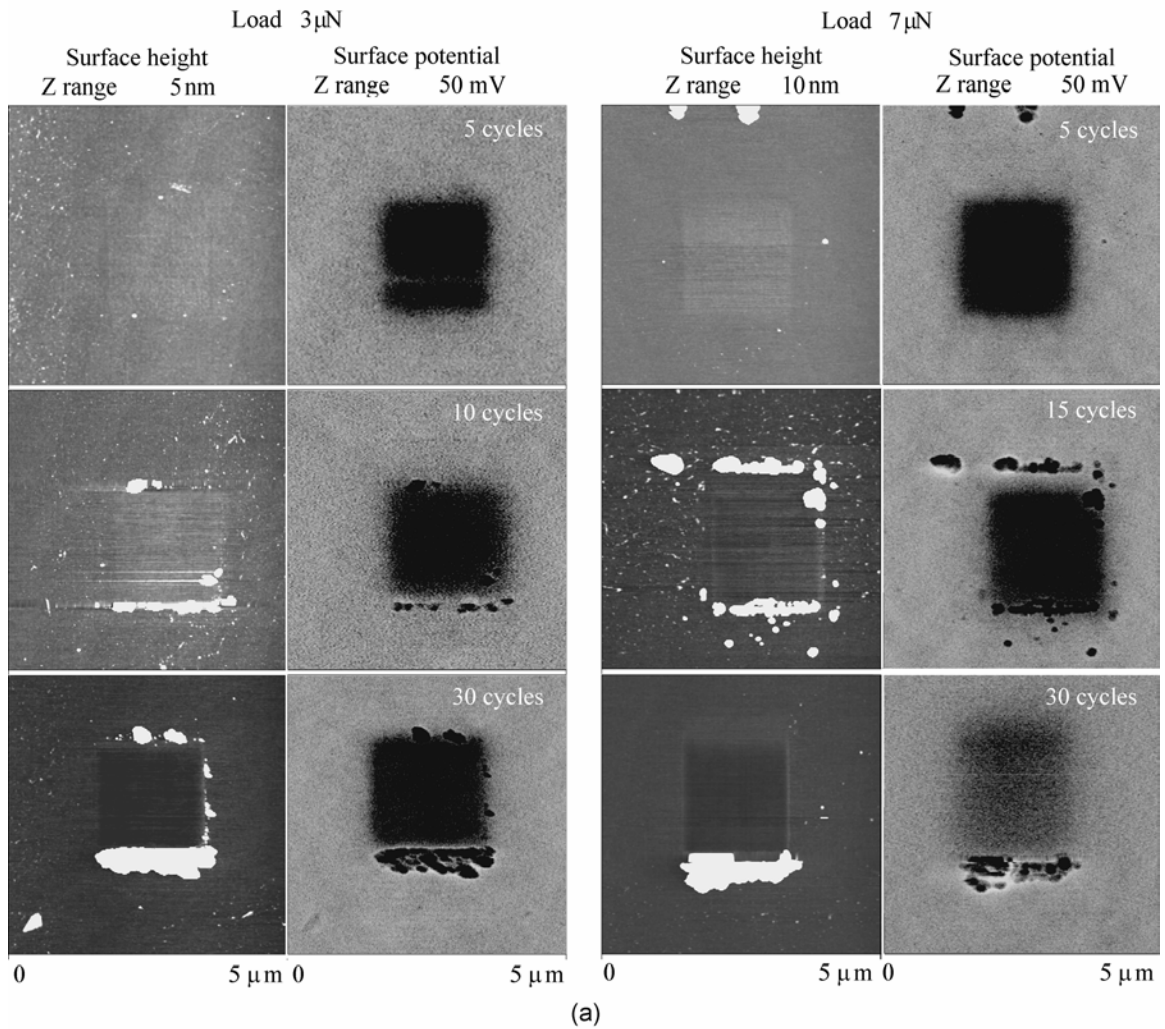
All later KPM measurements were performed at a lift scan height of 50 nm and AC voltage of 5 V. These parameters resulted in good lateral and potential resolution and allowed us to capture with some probes up to 20 images without damaging the tip. It should be noted that the durability of the coated probes is very low. We used about 30 probes to obtain the data presented. The data plotted on one graph were always obtained with the same probe. We checked the reproducibility of the data on silicon. The variation of the measured values of surface potential was in the range of 50-100 % as measured using different coated tips. We will observe later (e.g. Fig. 2.5 (a)), that surface potential changes gradually at the edges of the wear scar due to the averaging of the measured signal over worn and unworn areas, which possibly results from the long-range electrostatic interaction between the probe and the sample [Jacobs et al., 1998; Yokoyama and Inoue, 1994] and reaches constant value at a distance on the order of 50 to 150 nm from the edge. The gradual change may also result from structural changes, which extend beyond the worn region.

On the basis of these investigations we have concluded that in the present study KPM is not adequate for routine quantitative measurements and provides qualitative information on surface potential change. The measured change in surface potential is a weighted average of the potentials of worn and unworn areas present on the surface, the derivatives of the capacitances between the tip and these areas being the weighting factor [Jacobs et al., 1998].

2.4.2 Silicon and silicon lubricated with fully bonded Z-DOL

A sample of single crystal silicon was abraded at loads of 3 μN and 7 μN . Wear scars were created at 5, 10, 15, 20 and 30 cycles. Surface topography and surface potential change were measured using KPM. Fig. 2.5 (a) shows representative topography and surface potential images of the scars. As observed from Fig. 2.5 (a), there are no signs of wear for 3 μN at 5 cycles. However, surface potential changes. With an increase in number of cycles the scratched region first rises and then the surface begins to wear after 20 cycles. In the case when the scratched area was raised rather than depressed as compared to the unworn surrounding region we used negative values to plot the wear depth. It should also be noted, that wear depth of the wear scar created at a load of 3 μN after 15 cycles was measured to be zero; some debris particles were present around the worn region. With a load of 7 μN the average height of the worn region monotonically increases from -0.5 to 1 nm with increasing number of cycles. The change in surface potential with the number of cycles (Fig. 2.5 (c)) is negative in sign for both loads.

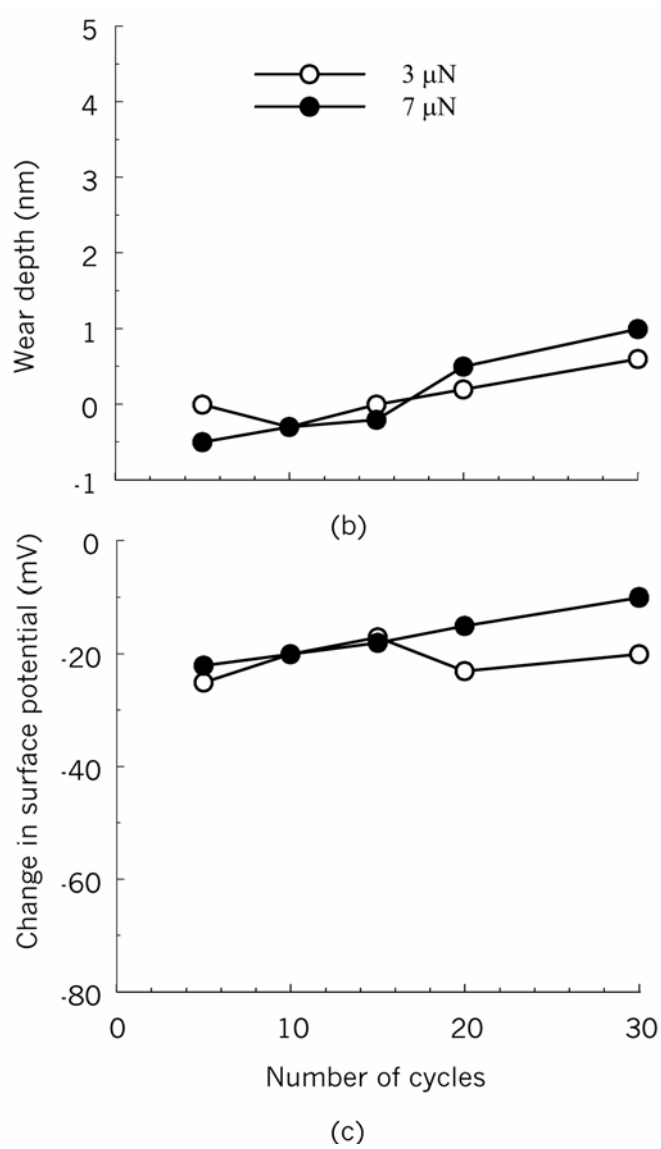
Wear marks were created at 3 μN , 7 μN and 10 μN on silicon samples lubricated with 1 nm thick fully bonded Z-DOL. Surface potential was measured for the wear scars created at 1, 3, 5, 10, 15, 20 and 30 cycles. Fig. 2.6 (a) shows representative topography and surface potential maps of the scars. Fig. 2.6 (b) and (c) show wear depth and surface potential change as a function of number of cycles, respectively. Negative wear depth was registered in all cases except at a load of 10 μN and 30 cycles. For the same load and number of cycles negative wear depth is larger for the lubricated samples compared with bare silicon. It is known that water molecules penetrate the lubricant film and cause debonding of the polymers attached to the silicon oxide surface (see e.g., Binggeli and

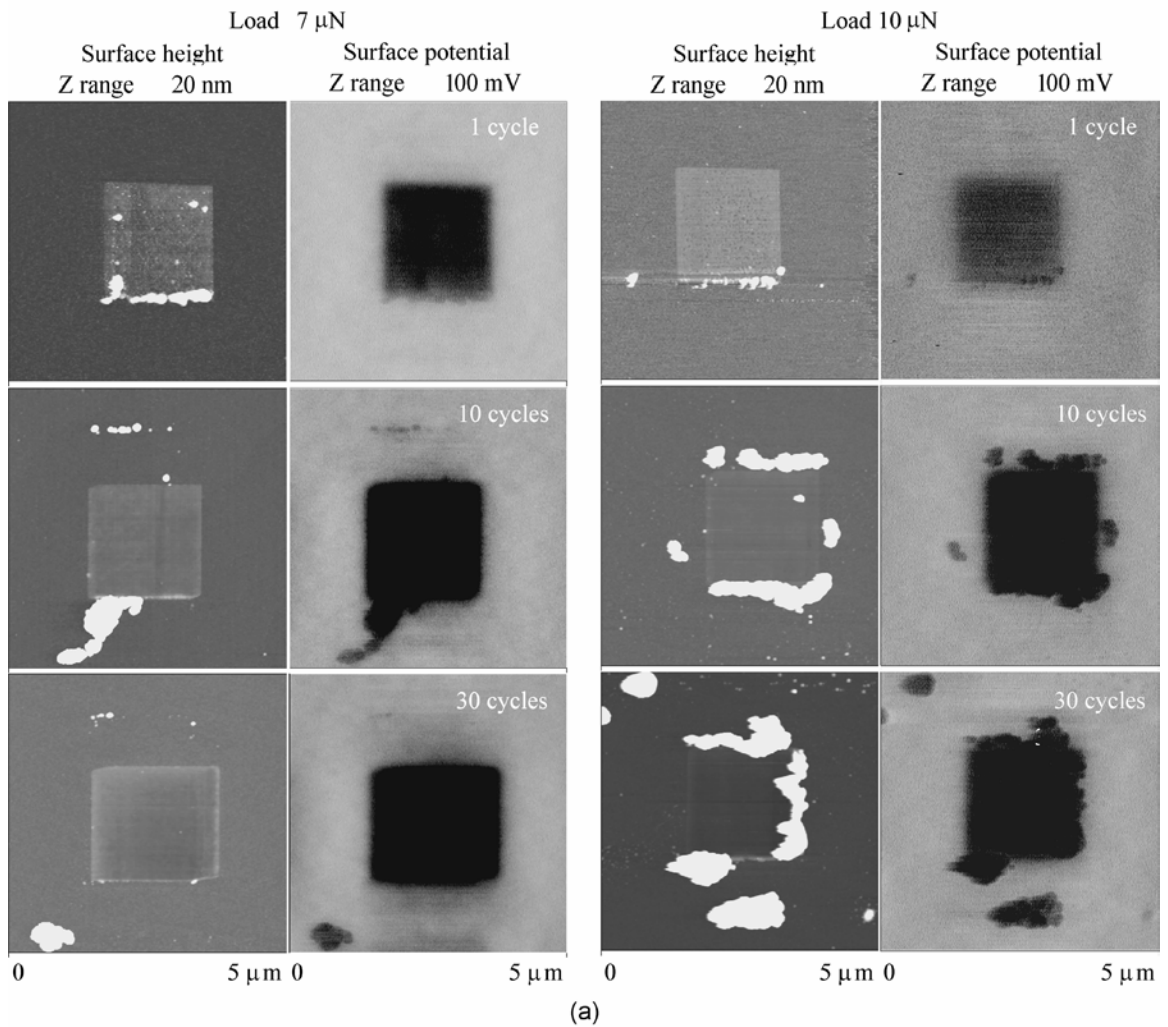


Continued

Figure 2.5: (a) Surface height and surface potential maps of wear regions, and effect of number of cycles on (b) wear depth and (c) change in surface potential for single crystal silicon.

Figure 2.5 continued

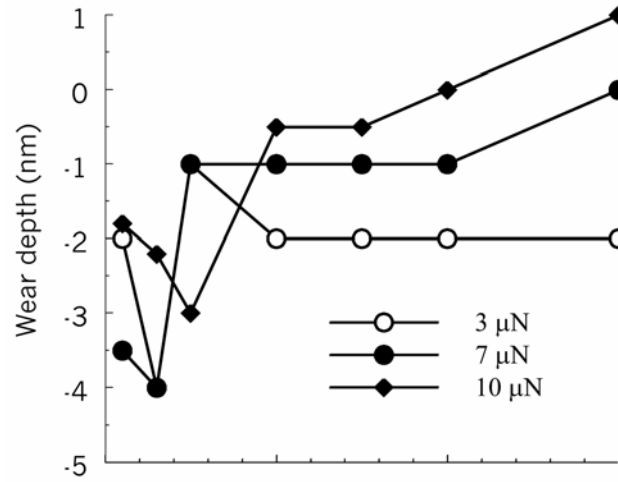




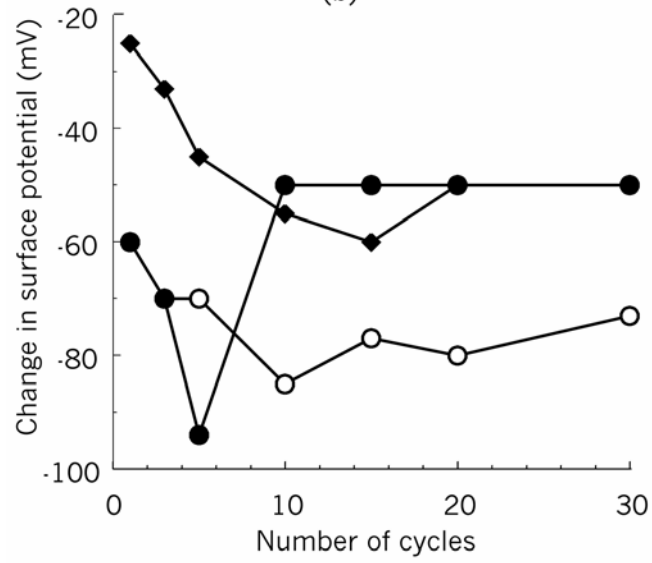
Continued

Figure 2.6: (a) Surface height and surface potential maps of wear regions, and effect of number of cycles on (b) wear depth and (c) change in surface potential for single crystal silicon lubricated with fully bonded Z-DOL.

Figure 2.6 continued



(b)



(c)

Mate [1995]). Polymer swelling might be one of the phenomena responsible for greater upheaval of the scratched area as compared to bare silicon, but as the lubricant film becomes unbonded, it could be easily removed during the very first scratching cycle. Surface potential changes in the range from -100 to -20 mV but there is no strong correlation with load. However, as the number of cycles increases both negative wear depth and surface potential change go through minima.

DeVecchio and Bhushan [1998] reported that a silicon surface scratched with a low load stuck above the surface of the sample and the change in surface potential was observed. The authors speculated on three possibilities for this phenomenon. First, a phase change under pressure resulting from physical and chemical changes produces a rise in surface topography. A second possibility is the relaxation of residual stresses. Third is that the rubbing of the sample by the diamond tip has caused a reoxidation of the sample surface resulting in a slightly thicker silicon oxide region in the abraded area.

We observed changes in the surface potential for both negative and positive wear depths on the silicon samples. In order to understand what changes (chemical, structural or both) occur on the silicon surface, we performed AES analysis of bare and lubricated silicon samples. It should be noted that AES is commonly used to determine elemental composition at the surface with high lateral resolution. However, a chemical shift due to oxidation can be registered for silicon [Handbook of Auger Electron Spectroscopy, 1995]. The peak at 96 eV in the AES spectrum corresponds to elemental silicon. That at 86-89 eV stands for the oxidized silicon.

AES measurements averaged over a scan area of approximately $0.64 \mu\text{m}^2$ were conducted on areas inside and outside wear scars created on single crystal silicon and

single crystal silicon lubricated with 1 nm thick fully bonded Z-DOL. The sampling depth was less than 2 nm. Samples were scratched at loads of 3 μN and 7 μN during 5, 10 and 30 cycles. Fig. 2.7 (a) shows representative AES spectra obtained on a silicon sample. Both silicon (peak at 96 eV) and silicon oxide (peak at 89 eV) were detected on the initial surface (Fig. 2.7 (a), virgin surface). The area where wear scars were located was etched for 30 s by using argon ions at beam energy of 2 keV with an etching rate of about 0.07 nm/s. After etching, no silicon oxide was found inside and outside wear marks with both positive and negative wear depth, which indicates that silicon oxide is very thin.

The AES results obtained on single crystal silicon lubricated with 1 nm thick fully bonded Z-DOL are similar to those for bare silicon (Fig. 2.5 (b)). After etching no silicon oxide was found inside and outside wear marks with both positive and negative wear depth, which indicates that silicon oxide is very thin. It should be noted that AES spectra did not show any of fluorine from Z-DOL lubricant on the surface, perhaps because of low film thickness as compared to the sampling depth.

Based on AES data there appear to be no chemical changes during these experiments; therefore, structural changes should be responsible for the changes in surface potential due to sliding. However, during early stages of sliding, very thin contaminant film, natural oxide or lubricant gets removed which can give rise to the initial change in surface potential. In ambient air the contaminant film and oxide layer are reformed after the wear scars are created. Based on AES, the films are expected to be thin and may only slightly affect the measured change in the surface potential. Therefore, we believe that structural changes should primarily be responsible for the surface potential

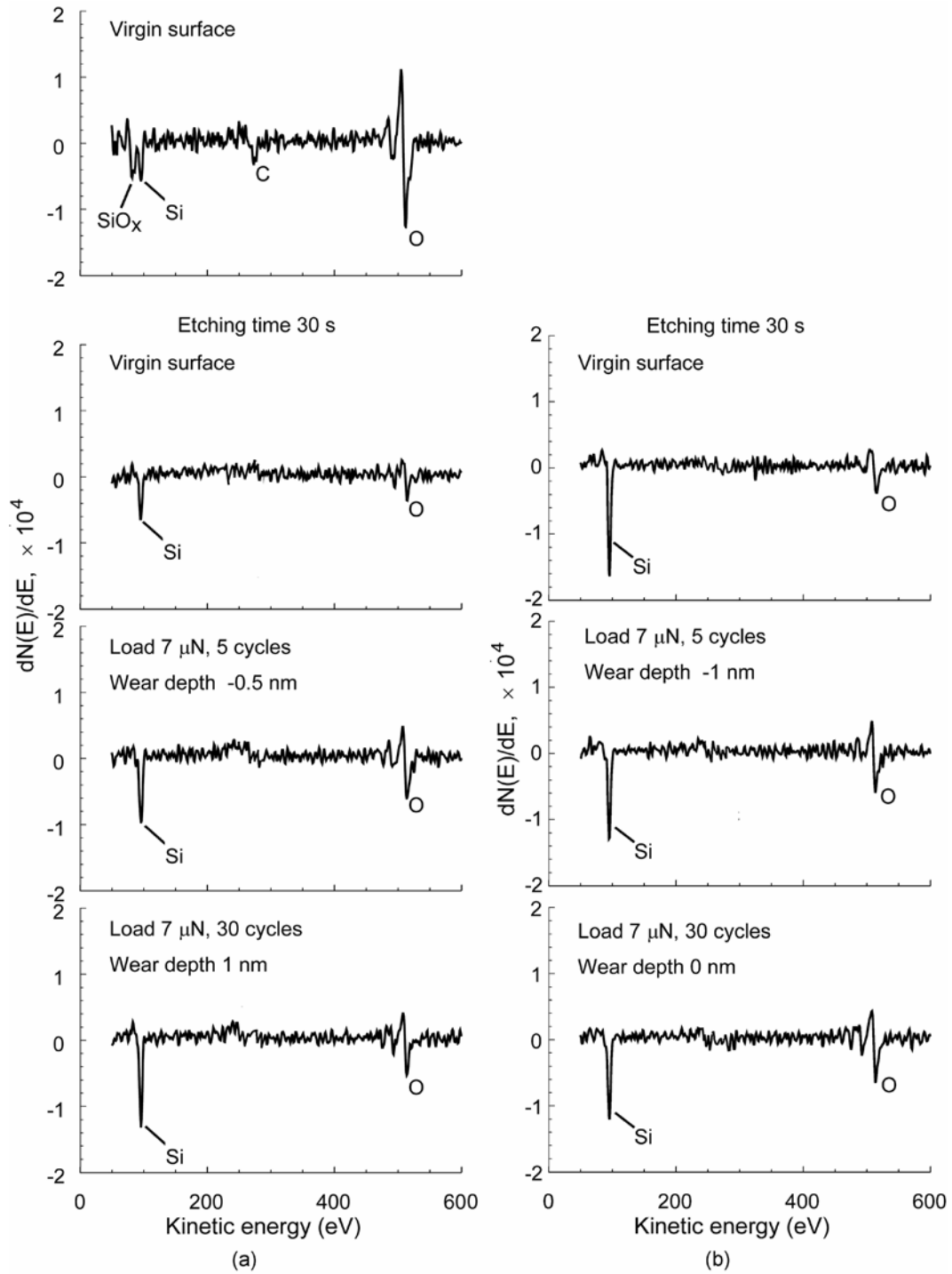


Figure 2.7: AES spectra for (a) silicon and (b) silicon lubricated with fully bonded Z-DOL.

change. To better understand what structural changes occur during rubbing of the sample surface against the AFM tip, we examine the mechanisms responsible for the wear of the silicon samples at ultralow loads.

2.4.2.1 Wear mechanisms of silicon at ultralow loads

Silicon is a brittle material. Contact damage in brittle materials is usually discussed in terms of elastic and elastic/plastic deformations. In order to determine deformation mode, we calculated contact stresses. Using Hertzian analysis of a hard spherical body in contact with a flat surface we calculated maximum Hertzian pressure by using the following equations:

$$p_{\max} = \frac{3W}{2\pi a^2} \quad (2.8)$$

and

$$a = \left\{ \frac{3WR}{4} \left[\frac{1-\nu_1^2}{E_1} + \frac{1-\nu_2^2}{E_2} \right] \right\}^{1/3}, \quad (2.9)$$

where p_{\max} is the maximum Hertzian contact pressure, W is the applied normal load, a is the radius of the contact area, R is the radius of the diamond tip (approximately 100 nm), $E_{1,2}$ and $\nu_{1,2}$ are Young's moduli of elasticity and Poisson's ratios of the two contacting bodies, respectively. For the diamond tip in contact with a silicon (100) surface, the Young's moduli of elasticity and Poisson's ratios are $E_{\text{Si}} = 130$ GPa, $E_{\text{diamond}} = 1140$ GPa, $\nu_{\text{Si}} = 0.28$, and $\nu_{\text{diamond}} = 0.07$.

The calculated maximum Hertzian contact pressure by using Eqs. (2.8) and (2.9) at normal loads of 3 μN and 7 μN are 9.73 GPa and 12.9 GPa. The microhardness of silicon is about 11.5 GPa [Bhushan and Koinkar, 1994]. Based on contact mechanics it is

known that the maximum stress in sliding contact occurs beneath the surface if the friction coefficient is in the range of 0 - 0.3 and its magnitude increases with an increase in the coefficient of friction [Bhushan, 1999b]. The coefficient of friction of diamond versus single crystal silicon (100) in ambient air is about 0.05 [Bhushan, 1999a]. The onset of plastic deformation can be estimated using the equation from [Bhushan, 1999b, p. 206]

$$(p_{\max})_y = 1.60Y = 0.64H . \quad (2.10)$$

For silicon, onset of plastic deformation occurs at $(p_{\max})_y$ of 7.4 GPa which is approached in our experiments. Thus, we believe that in ambient air, material is removed from the silicon surface by subsurface fatigue wear and stresses beneath the silicon surface can result in subsurface structural changes.

2.4.3 Gold

A 110-nm thick gold film sputter deposited onto a silicon substrate was chosen as a sample of noble metal. Wear marks were created at 1, 3, 5 and 7 μN during one cycle. Fig. 2.8 (a) shows the effect of load on wear depth and surface potential change. Note that the change in potential is positive rather than negative as observed in the other samples. As the load increases, the surface potential change increases as well. It is reasonable to assume that there is no chemical reaction on the sample surface. As seen from Fig. 2.8 (b), the sample surface undergoes structural changes. The initial grain structure is preserved for 1 μN ; however, the surface was slightly “pushed” down and adsorbed contaminants were removed. As the load increases, plastic deformation occurs and its magnitude increases with an increase in load, which is believed to be responsible for an increase in the surface potential change.

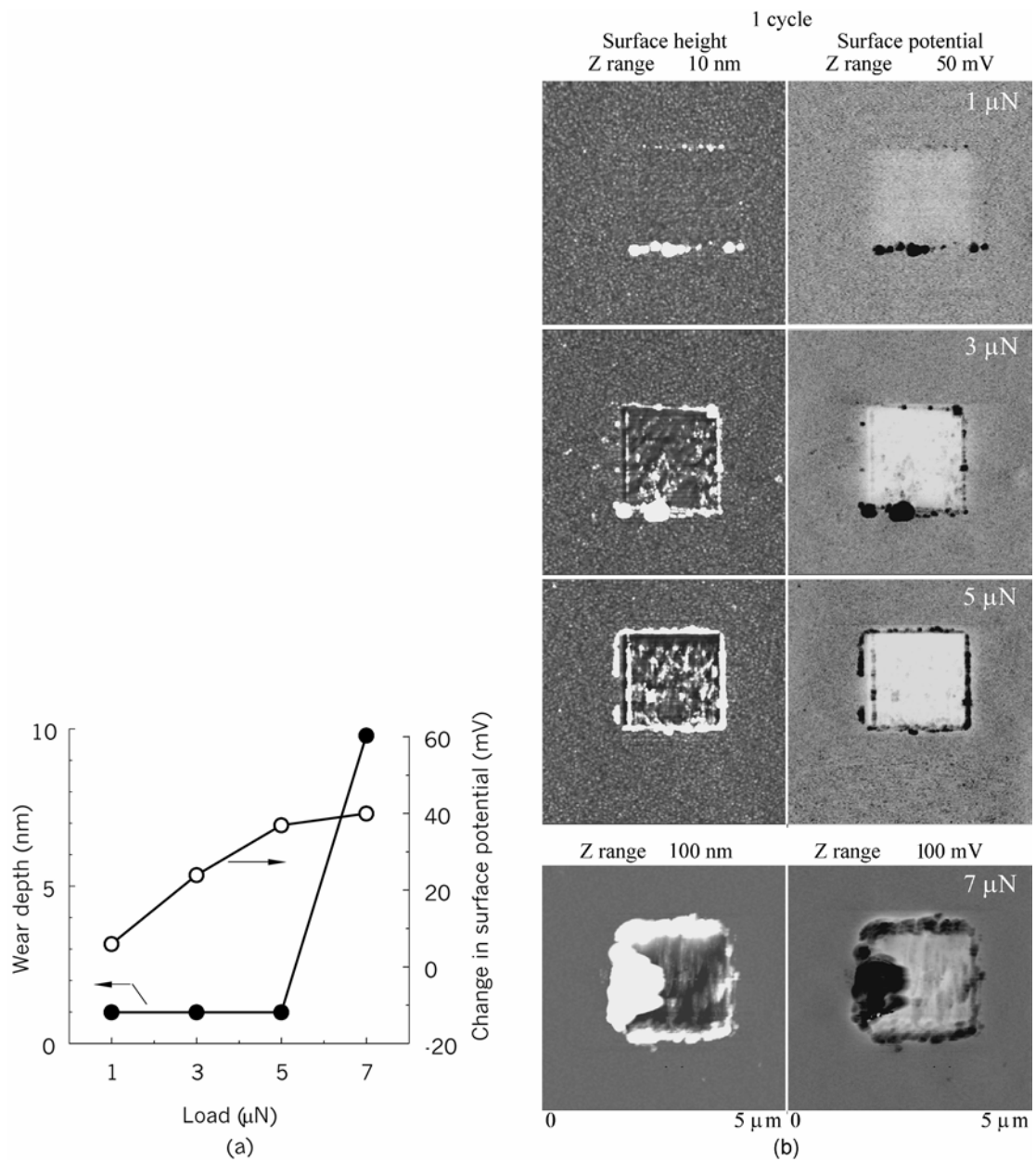


Figure 2.8: (a) Effect of load on wear depth and change in surface potential for gold film deposited on single crystal silicon, and (b) surface height and surface potential maps of wear regions.

2.4.4 Aluminum

Surface potential change with load was studied for a sample of aluminum. Wear marks were created at 3, 5 and 7 μN during one cycle. Fig. 2.9 (a) shows the effect of load on wear depth and change in surface potential. The abraded regions show large potential contrast (Fig. 2.9 (b)). However, surface potential change is not strongly correlated to load. The specimen we used was a polished one. The metal surface undergoes both chemical and structural changes during polishing. As the average wear depth for all the loads does not exceed 1 nm, we can assume that we have studied properties of the mechanically modified layer. Further increase in load up to 9 μN in order to remove this layer mechanically resulted in large wear depth that made surface potential measurements unstable resulting in tip damage. We believe that the variation of surface potential may be due to both structural and chemical changes at the surface.

2.4.5 Alumina

An alumina sample was chosen as an insulating material. Wear marks were created at 15, 20, 25 and 30 μN at 1 cycle. It is observed from Fig. 2.10 that there is no significant change in surface potential due to wear. Large wear particles or agglomerates of wear particles are clearly seen on the potential maps. The variation of the surface potential over the scan area was estimated to be in the range of 30-40 mV even for the unworn regions. It is worth mentioning that in the case of metals, work function affects the surface potential, whereas, in the case of dielectrics isolated surface charges and polarization dominate the surface potential [Yokoyama and Inoue, 1994]. As a result, this technique is not suitable for measurements of physical and chemical changes of dielectrics.

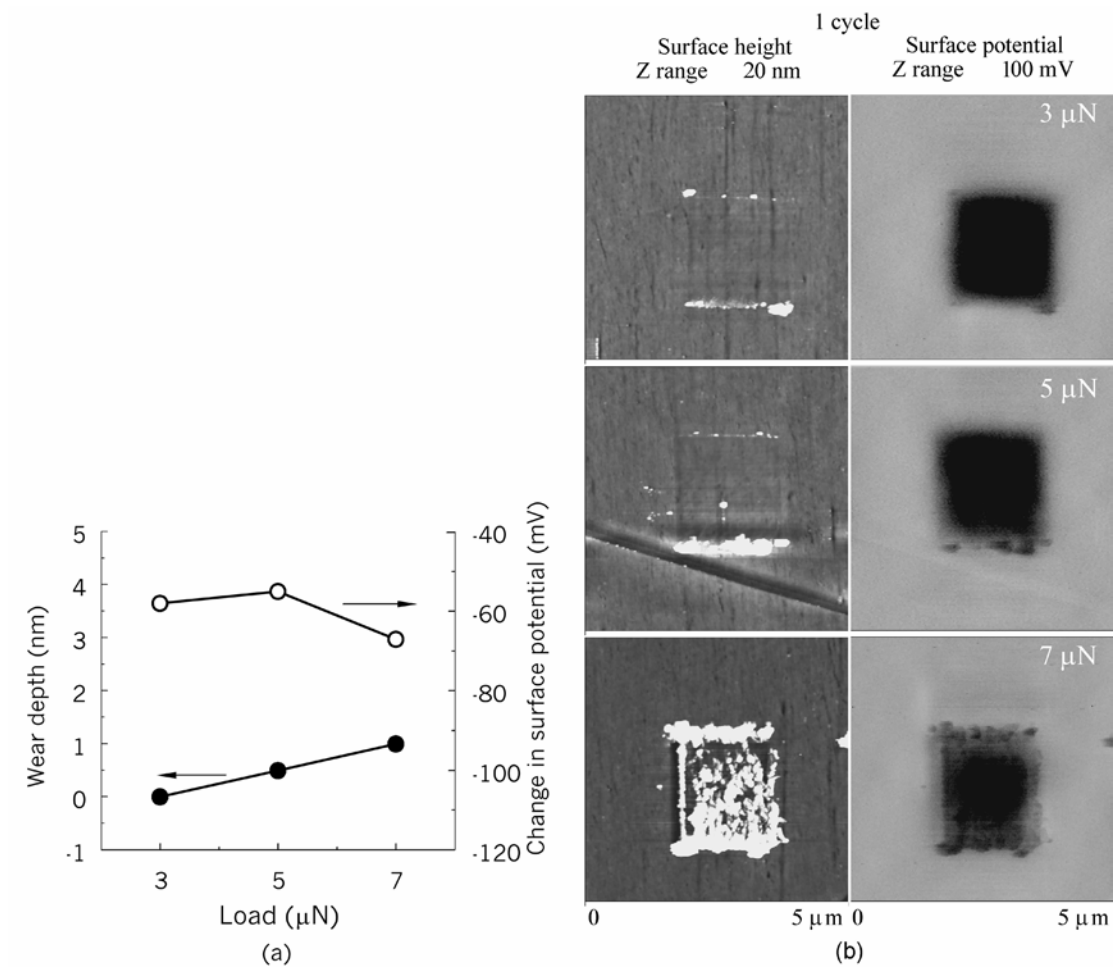


Figure 2.9: (a) Effect of load on wear depth and change in surface potential for aluminum, and (b) surface height and surface potential maps of wear regions.

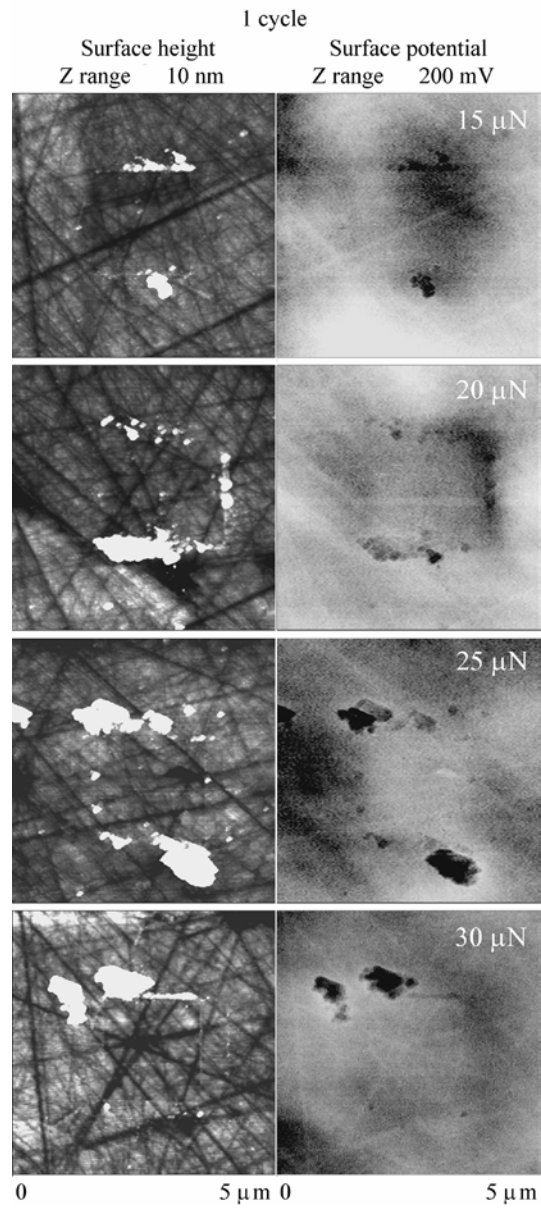


Figure 2.10: Surface height and surface potential maps of wear regions on alumina sample at different loads.

2.4.6 Some explanations for the sign of surface potential

Table 2.1 shows EWF, the difference in EWF of the tip minus that of the sample [Fomenko, 1966] and measured surface potential for various materials. Based on the comparison between the difference in EWF and measured surface potential for unworn region, we note that in the case of silicon and gold, the sign of the difference and that of the measured surface potential is the same. However, in the case of aluminum this does not hold true because aluminum gets oxidized readily and forms alumina. The dielectric alumina layer possibly affects the surface potential.

Next, regarding the changes in the surface potential due to sliding, the structural changes and deformation affect the energy levels of the solid [Fawcett et al., 1980]. For metals, the EWF is reported to decrease when plastic deformation occurs [Zharin et al., 1995]. Gold being soft goes through significant plastic deformation, which would likely decrease EWF and increase surface potential of worn area as compared to that of unworn region, which is the case in our measurements. No comments can be made for the other samples.

2.5 Summary

A Kelvin probe microscope (nano-Kelvin probe technique) was successfully employed for study of early stages of wear at ultralow loads on a variety of samples of different nature such as single crystal silicon (100), single crystal silicon (100) lubricated with fully bonded Z-DOL, gold, aluminum and alumina. The effect of load and number of cycles on surface potential change was studied. Even in the case of “zero wear” (no measurable deformation of the surface), there can be a significant change in surface potential inside the wear mark. This allows for the study of the onset of wear in the

ultralow wear regimes that is not possible with other techniques. We found that the technique allows only qualitative measurements of surface potential change.

Negative wear was registered for single crystal silicon (100) and single crystal silicon (100) lubricated with fully bonded Z-DOL at ultralow loads and low number of cycles. The initial surface potential change can result from removal of a thin contaminant layer, natural oxide or lubricant, during the few first wear cycles. Structural changes occurring beneath the surface due to subsurface fatigue wear are believed to be responsible for the subsequent potential change and Kelvin probe microscopy is sensitive to them. The results obtained for gold suggest the KPM is sensitive to the change of material work function under plastic deformation. In the case of aluminum no significant trend in surface potential change is observed. This might be explained by the presence of a mechanically modified layer on the sample surface resulting from polishing. In the case of dielectrics, isolated surface charges and polarization dominate the surface potential components; therefore, this technique is not suitable for measurements of dielectrics.

The measurements were performed in ambient air and we can not exclude the possibility of production of chemical compounds by reaction with molecules in air on the sample surface, except for gold. Further research is required with controlled environmental conditions to obtain quantitative nano-Kelvin probe results.

CHAPTER 3

EFFECT OF OPERATING ENVIRONMENT ON FAILURE MECHANISM OF A HEAD-TAPE INTERFACE IN A LINEAR TAPE DRIVE WITH A BELT DRIVEN CARTRIDGE

3.1 Introduction

Magnetic recording devices are commonly used to store large amounts of information in a nonvolatile manner for audio, video and digital applications. The types of magnetic media for digital recording are: flexible media (tapes and floppy disks) and rigid disks. Some of the advantages of the tape drives are the low cost per megabyte of the stored information, high volumetric density and portability. Tape drives are primarily used to store and archive information on the order of terabytes. This area of usage imposes strict requirements on the high reliability and excellent performance of both the drives and tapes even when they are stored and used under extreme operating conditions. Both magnetic recording and retrieval processes are accomplished by relative motion between a magnetic head and a magnetic medium. Need for a high storage density requires that the surfaces be as smooth as possible and flying heights be as low as possible [Bhushan, 1996, 2000]. In the case of magnetic tapes, smoother surfaces lead to increased static/kinetic friction, and low flying heights lead to partial contact between the

head and the tape both of which result in the head and the media degradation and failure due to tribological aspects. Thus, the understanding of these tribological aspects of the head-tape interface becomes important for the design and manufacture of the tape drives and tapes.

The requirements for high-quality information storage systems are virtually error-free recording and faithful reproduction of the recorded information. Numerous factors contribute to signal reproduction. In linear and rotary head tape drives, with particulate and metal evaporated tapes tribological aspects such as adhesion and friction at the head-tape interface are found to be responsible for the generation of the loose debris and stain, and pole-tip recession (PTR), which lead to head medium spacing losses [Bhushan and Hahn, 1995; Patton and Bhushan, 1997a; Scott and Bhushan, 1999, 2000, 2001]. It was also found that the short-term head signal losses (dropouts) correlated to friction force and debris passing between the head and the tape [Anderson and Bhushan, 1996; Patton and Bhushan, 1997b]. Kattner and Bhushan [2000a, 2000b] evaluated the magnetic reliability of a linear tape drive with a belt driven cartridge and magnetoresistive (MR) head, and Co- γ Fe₂O₃ and metal particle (MP) tape. Coefficient of friction, head output and number of dropouts per minute were measured to determine wear mechanism at the head-tape interface. It was found that a process of formation, accumulation and removal of the stain on the head was one of the contributors to the variations in the magnetic performance of the interface. However, the presence of a thin layer of stain was found to be beneficial for decreasing head wear. Previous studies have shown that operating environment (temperature and humidity) has a dramatic effect on tribological and magnetic performance and durability of the head-tape interface in a rotary head drives

using particulate and metal evaporated tape [Anderson and Bhushan, 1997; Patton and Bhushan, 1996, 1997b; Luk and Bhushan, 2001].

The effect of operating environment (temperature and relative humidity) on the performance and failure mechanism of head-tape interface in a linear tape drive has not been studied much. Several studies aimed at investigation of material transfer from the media to the head were performed at ambient [Kattner and Bhushan, 2000a, 2000b] and extreme [Hempstock et al., 2000] environmental conditions. The latter was based on evaluation of both virgin and worn heads and tapes and measurement of the number of dropouts per minute during the test. Kattner and Bhushan [2000a, 2000b] studied mechanisms responsible for the head-tape interface failure by evaluating the changes at the head-tape interface as well as continuous monitoring of coefficient of friction, head output, and the number of dropouts per minute during the test. The approach of Kattner and Bhushan [2000a, 2000b] was employed in the present study.

The objective of this study was to investigate the effect of operating environment (temperature and humidity) on the failure mechanism of the head-tape interface in a linear tape drive with a magnetoresistive head and a belt driven cartridge. Long-term durability tests for the full length of the tape in the cartridge were conducted at the corners of the operating envelope as specified by the manufacture as well as at ambient temperature and humidity. Wear mechanisms responsible for the observed tribological and magnetic behavior are discussed.

3.2 Experimental details

3.2.1 Experimental apparatus and procedure

All tests were conducted using the experimental set-up shown in Fig. 3.1 [Kattner and Bhushan, 2000a, 2000b]. A Seagate Travan Hornet 20 ATAPI (TR-5) tape drive was used for this study, which was operated using software provided by the manufacturer. It was modified in order to make friction measurements. Belt driven cartridges with MP tape 8 mm wide (Imation Travan NS 20 GB) and thin-film read-while-write MR heads were used in the study. A data cartridge tape is a self-contained reel-to-reel tape deck without a motor or read-write head and is belt driven via a capstan [Bhushan, 2000]. A schematic of the tape path of a belt-driven cartridge is shown in Fig. 3.1. The capstan turns the drive roller, which in turn moves the elastomeric drive belt. The drive belt transfers the movement to the tape motion. For economy and reliability, designs embodying a self-tensioning drive belt without any movable tensioning rollers are used. In such designs, the belt tension is maintained by the elastic properties of the textured drive belt (typically made of polyurethane). The textured surface (matte finish) on the drive belt allows air to escape, which minimizes belt slippage even at high speeds and thus improves the grip for better tape tension. The drive belt simultaneously controls the rotation of both the winding and unwinding tape reels, without the need for any complicated servo mechanisms. The tape cartridge is capable of operating bidirectionally in either streaming (or continuous) mode or a start-stop mode. The nominal tension and speed are 0.8 N (80 g) and 2.4 m/s (94 ips), respectively.

A wavelength of 0.64 μm (80 kfc) was recorded on the tape during the forward pass. Then, the drive was programmed to read the recorded signal during forward and

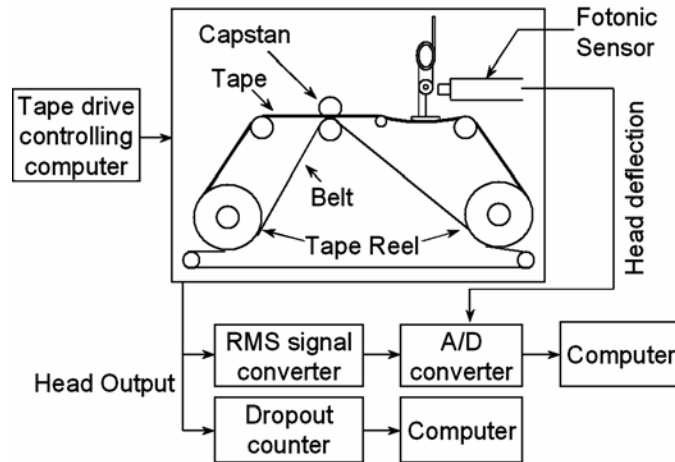


Figure 3.1: Schematic of the experimental apparatus.

reverse passes at 2.4 m/s for the full tape length in the cartridge (440 m for a round trip, which constituted one cycle and consisted of one forward and one reverse pass). The drive was stopped for 5 s after each forward and reverse pass was completed for it to settle and make the friction force measurement possible in the forward pass. This pattern was continued for 10000 cycles (according to the manufacturer the maximum life of the cartridge is 5000 cycles) or until failure occurred. The criteria for failure were the loss of the mobility of the tape cartridge during the test and/or head output change by ± 3 dB. Throughout the entire test the MR read element was active. During playback, the drive was operated with the automatic gain control turned off. (Automatic gain control is used during the normal operation of the drive to maintain signal amplitude during playback.)

During each test, head output, friction force, and the number of dropouts per minute were measured.

The reproduced signal from the head (Head output in Fig. 3.1) was amplified by the drive electronics and was transmitted to an RMS (RMS-to-DC) converter (AD637, Analog Devices, Norwood, MA) and a Doradus 20 dropout tester (System 20 VTT multi-level dropout tester, Doradus Corp, Minneapolis, MN). The Fotonic sensor output (Head deflection in Fig. 3.1) and the RMS head output were captured by a data acquisition board (DAS-16G, Omega Engineering Inc., Stamford, CT) with a sampling rate of 4 Hz. The data acquisition was controlled by Snap-Master V3.2 data acquisition software (HEM Data Corp., Southfield, MI). The data were stored on the computer for later processing. A BASIC program on another computer controlled the Doradus 20 dropout tester through an RS-232 port and averaged the dropout data over 25 cycles. Snap-Master data acquisition software was used to calculate coefficient of friction and head output. Coefficients of both static and kinetic friction were calculated. The values of coefficient of kinetic friction and head output were averaged over each forward pass and these values were plotted on all the graphs. Head output data is presented in a voltage decibel format, and the reference 0 dB voltage is the initial RMS playback voltage averaged over the first 10 cycles at a given temperature and humidity.

Coefficient of friction was measured as follows. The friction force between the tape and the head is transmitted to the post that holds the head. This post was fixed to the tape drive frame and was able to bend back and forth similar to a cantilevered beam. The friction force of the head-tape interface was measured by measuring the deflection of the post and converting it to force units. The deflection was measured using a proximity MTI

2000 Fotonic sensor (MTI Instruments Inc., Latham, NY) with a probe type 2020R having the sensitivity of 16 nm/mV. Calibration of friction force was performed by using a force gauge with a range of 0-15 g to apply the force to the head. Loads in the range of 0-5 g were applied and the displacement was measured by the Fotonic sensor. The linear relationship between the applied force and the Fotonic sensor output was measured to be 17.5 mV/g.

The coefficient of friction was calculated by assuming that only tape tension created the normal force on the head and that the tension was the same on both sides of the head. Since the only other force acting on the head, the friction force, was small, these assumptions were justified. Additionally, the tension was assumed to be constant through the length of the tape in the cartridge. The nominal tape tension T was taken 0.8 N (80 g). The wrap angle θ measured from a photograph of the tape in contact with the head was $13 \pm 1^\circ$. By drawing a free-body diagram of the head the coefficient of friction, μ , can then be determined as [Kattner and Bhushan, 2000a]

$$\mu = \frac{\text{Friction force}}{2T \sin\left(\frac{\theta}{2}\right)}. \quad (3.1)$$

The Doradus 20 dropout tester can measure twenty classes of dropouts defined by ranges of dropout depth and duration simultaneously. Dropout depth and duration are selectable in the ranges of 1 to 22 dB in 0.5 dB increments and 0.5 to 300 μs in 0.5 μs increments, respectively. In this study, the various ranges of dropout depth and duration were defined: 4-6 dB, 6-9 dB, 9-12 dB, and >12 dB; 0.5-3 μs , 3-6 μs , 6-9 μs , 9-12 μs ,

and $>12 \mu\text{s}$. Number of dropouts per minutes were measured during forward and reverse passes and were averaged over 25 cycles.

Figure 3.2 shows the number of dropouts per minute as a function of number of cycles for the test performed at 22°C and 45% RH. The class with depth and duration of $> 12 \text{ dB}$ and $6\text{-}9 \mu\text{s}$, respectively, represented the trend observed for almost every other class and was selected here. Another reason for choosing this class for further consideration is as follows. According to the Wallace equation [Wallace, 1951]

$$\text{Separation loss (dB)} = 54.6 \frac{d}{\lambda}, \quad (3.2)$$

where d is change in magnetic spacing between the head and the tape separation and λ is the wavelength of the recorded signal. For $\lambda = 0.64 \mu\text{m}$ the depth of greater than 12 dB corresponds to the change in head-tape spacing d greater than 140 nm, which can be caused by large debris particles such as head cleaning agent (HCA) and particle agglomerates. Assuming that the particles are sliding at the head-tape interface at the velocity of the tape motion over the head, which is 2.4 m/s, it will take such a particle approximately $6\text{-}7 \mu\text{s}$ to slide over the write and read modules of the head. Due to these reasons, we are presenting only data for this class ($> 12 \text{ dB}$ and $6\text{-}9 \mu\text{s}$) on all graphs. It is important to note that the magnetic spacing can be different from the physical spacing.

3.2.2 Operating envelope

The tape drive operating envelope is $5\text{-}45^\circ \text{C}$ and 20-80% RH with a maximum wet bulb temperature of 26°C . Figure 3.3 shows locations of various experimental conditions with respect to the data processing envelope in the temperature - specific humidity (SH) plane. Specific humidity is mass of water vapor in a unit mass of moist air,

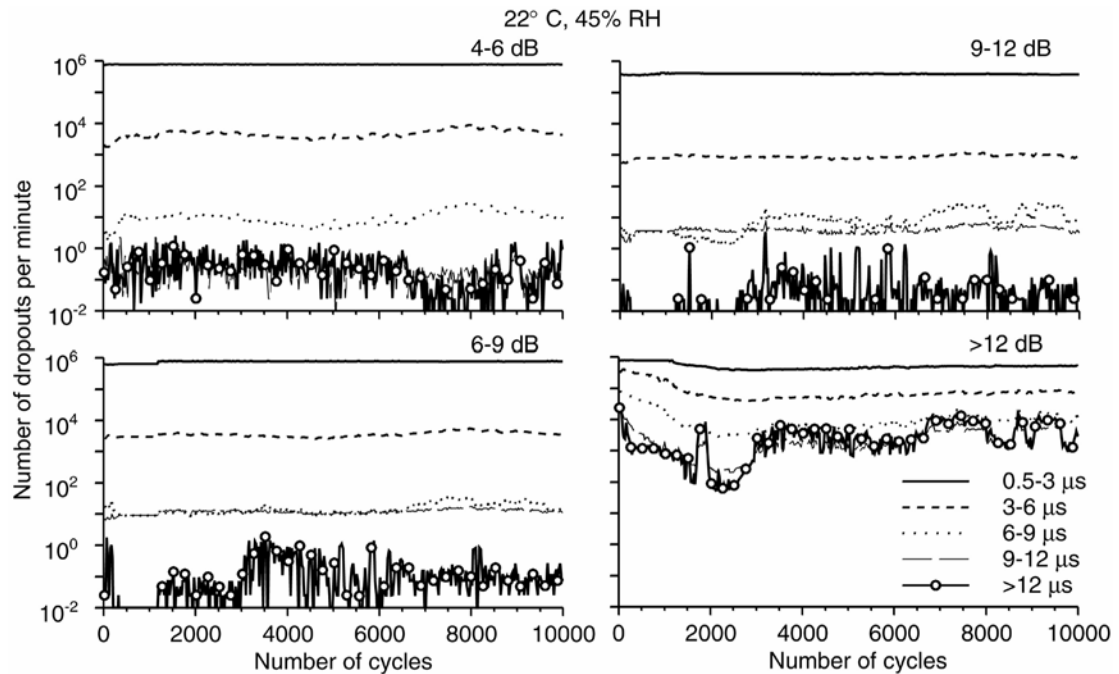


Figure 3.2: Number of dropouts per minute as a function of number of cycles for the test performed at 22°C and 45 % RH. The frequency of the symbols on all graphs for the class with the duration of greater than 12 μs is less than the actual number of the data points.

usually expressed as grams of vapor per kilogram of air. Both temperature and SH affect adsorption of water vapor from atmosphere onto surfaces, which affect interface tribology. Adsorption generally increases with increasing SH at a given temperature and it decreases as the temperature is increased at a given SH. Reference lines of constant relative humidity are also shown in Fig. 3.3. Relative humidity is ratio of the actual vapor

pressure of water in the air to that in air saturated with water vapor. As observed from Fig. 3.3, the amount of water at a given relative humidity is a function of temperature. In order to get the measure of the amount of water, we need to look at SH.

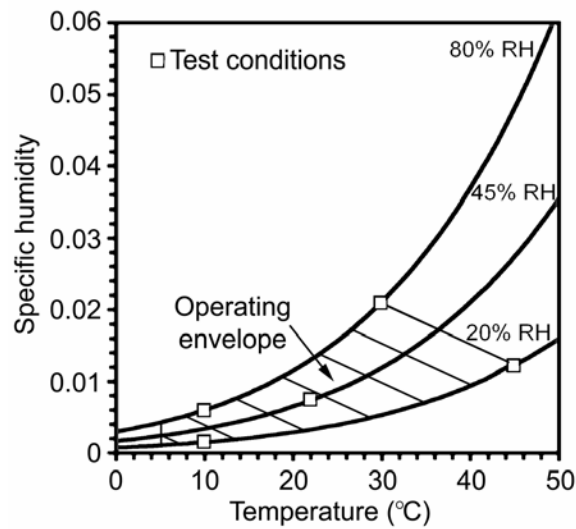


Figure 3.3: Environmental operating conditions used in the study.

All tests were performed at equilibrium conditions inside of an environmental chamber that was designed to control temperature and relative humidity (RH) in the range of 10-85° C and 20-80% RH with a precision of to $\pm 1^\circ$ C and $\pm 5\%$ RH,

respectively. The tape drive, with the tape cartridge loaded, was placed in the chamber at 22° C and 45% RH for 24 hours so that the components to reach the equilibrium, after which the signal with a wavelength of 0.64 μm (sine wave at a frequency of 3.7 MHz, 80 kfc) was recorded on to the tape during the forward pass. The tape was rewound and the desired temperature and humidity were set. The drive, with the tape, loaded was left in the chamber for another 24 hours, which allowed components to come to equilibrium at the testing conditions. (This step was omitted when the testing conditions were set at 22° C and 45% RH). The test was performed for 10000 cycles or until failure occurred.

3.2.3 Analysis of heads and tapes

The read head recession was measured using a stand-alone atomic force microscope (SAAF, Digital Instruments, Santa Barbara, CA) and the procedure developed by Scott and Bhushan [1999]. SAAF scans were taken of the thin-film region of the tape heads to measure the read head recession of the unworn heads and the worn heads at the end of testing. A special test was performed at 22° C and 45% RH, when the drive was stopped periodically to monitor changes in the read head recession during the course of the test. Great care must be taken in obtaining raw data from SAAF. The fact that the tape head sample had a rather small radius and that the scan size was so large (80 μm \times 80 μm), it made obtaining good raw data critical. In order to measure the recession, a tape head was placed face up on an X-Y stage. A stand-alone atomic force microscope was placed on a flat platform suspended just above the tape head specimen. Using the X-Y stage, the head was positioned just beneath the SAAF tip. A scan rate of 1 Hz was used and 512 data points were collected along each of the 512 scan lines. After engagement, while in the midst of scanning, the raw data were

examined in the fast and slow scan directions. If a significant slope existed in one or both directions, it was removed by adjusting the engagement screws of the SAAF_M. After this was accomplished, an image was captured to a file.

Two operations were performed on raw data. First, a zero-order flatten was applied. The flatten operation was used to eliminate image bow in the slow scan direction (caused by physical bow in the SAAF_M instrument itself), slope in the slow scan direction, and bands in the image (caused by differences in the scan height, due to debris, etc., from one scan line to the next). The flatten operation took each scan line and subtracted the average value of the height along each scan line from each point in that scan line. This brought each scan line to the same height, without affecting the measurement. Next, a second-order plane fit was applied in the fast scan direction. The plane fit operation was used to eliminate native head curvature in the fast scan direction. The plane fit operation calculated a best-fit second order curved surface for the image and subtracted it from the image. This surface had zero slope in the slow scan direction. After post-processing, the read head recession of the average two-dimensional profile was taken for the pole/shield-shield (read head) region. Depending upon the quality of the raw data, the flatten operation may not be required at all.

All optical images of the tape head thin-film region were obtained with an optical microscope (OPTIPHOT-2, Nikon Corporation, Tokyo, Japan) in the brightfield mode with a white light source. The gray-scale images were captured with a CCD camera with the resolution of 0.88 μm .

The unworn and the head worn for 10000 cycles at ambient temperature and humidity were analyzed using Auger electron spectroscopy (AES, Physical Electronics

680 scanning Auger nanoprobe) to detect elemental composition changes over the thin-film region. AES spectra were obtained at an accelerating voltage of 2 kV and a probe current of 1 nA. A scan area of $80 \times 100 \mu\text{m}$ was rastered over the thin-film region under and away from the cartridge belt while the analyzer averaged over the area.

Tape roughness statistics of the unworn and worn MP tape was measured using a large sample atomic force microscope (Dimension 3000, Digital Instruments, Santa Barbara, CA) [Bhushan, 1999]. Images of the MP tape with a scan size of $80 \times 80 \mu\text{m}$ were taken in contact mode using standard Si_3N_4 tips with a nominal spring constant of 0.6 N/m and nominal tip radius of curvature of 30-50 nm at a normal load in the range of 20-50 nN. Roughness data presented in the study are based on five sets of measurements.

3.2.4 Head and tape specimens

A thin-film read-while-write MR head was used. Figure 3.4 shows a schematic and an optical micrograph of the thin-film region of the unworn head used in the study. The head has one faceplate. The faceplate holds the chiplet, which contains the poles of the inductive write head and shielded MR read head. The position of the tape and cartridge belt with respect to the chiplet during the tests are shown on Fig. 3.4 (a). The chiplet is composed of an Al_2O_3 -TiC substrate. The undercoat and overcoat of the thin-film region are made of sputtered Al_2O_3 coating. One pole that is used exclusively for writing, one pole that is used for writing and serves, as a MR shield, and the MR shield are all made of CZT (cobalt-zirconium-tantalum). The MR element is made of permalloy (Ni-Fe).

Belt driven cartridges with MP tape 8 mm wide was used in the study. Table 3.1 summarizes roughness statistics of the virgin MP tape measured using an atomic force

microscope ($10 \times 10 \mu\text{m}$). Mean and σ values of roughness data are based on five sets of measurements. Figure 3.5 shows representative AFM images of the tape away from and under the belt.

		Away from the belt	Under the belt
σ (nm)		9.8 ± 0.9	7.6 ± 0.8
P-V (nm)		96 ± 14	99 ± 20
S_k		-0.21 ± 0.39	-0.36 ± 0.37
K		3.40 ± 0.39	5.57 ± 2.91
β^* (μm)	x ^{a)}	2.4 ± 0.6	2.3 ± 0.8
	y	2.1 ± 0.2	1.6 ± 0.5

^{a)} Tape motion direction

Notations. σ is standard deviation of surface heights, P-V is the distance between the highest asperity and the lowest valley, S_k is skewness, K is kurtosis, β^* is correlation length (the length over which the autocorrelation drops to 0.1 of its original value)

Table 3.1: Roughness statistics of virgin MP tape measured using an AFM ($10 \times 10 \mu\text{m}$). Roughness data are based on five sets of measurements.

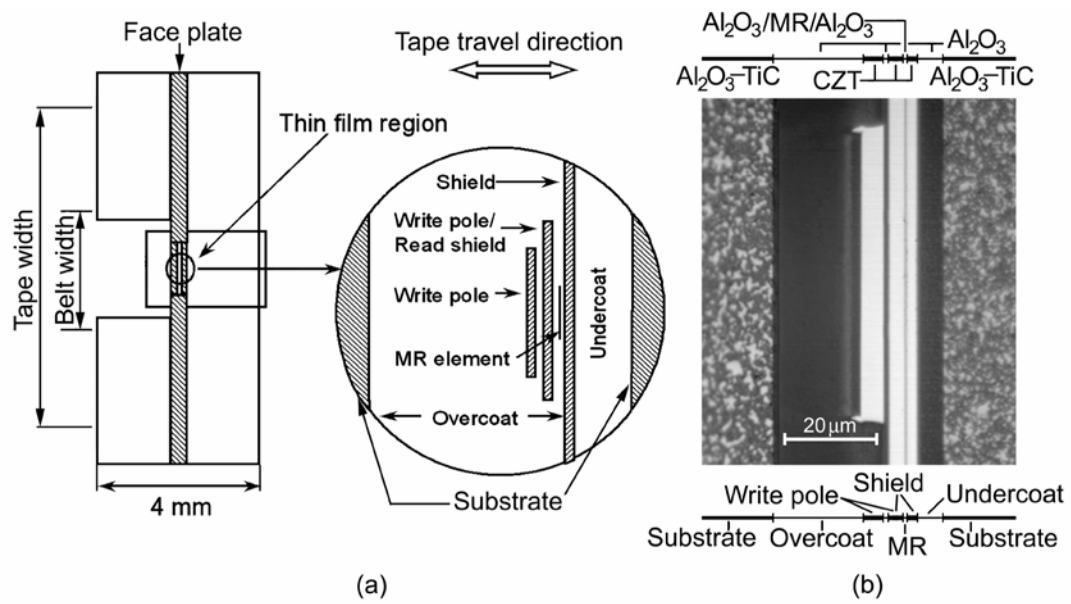


Figure 3.4: (a) Schematic and (b) optical micrograph of the thin-film region of the unworn MR head.

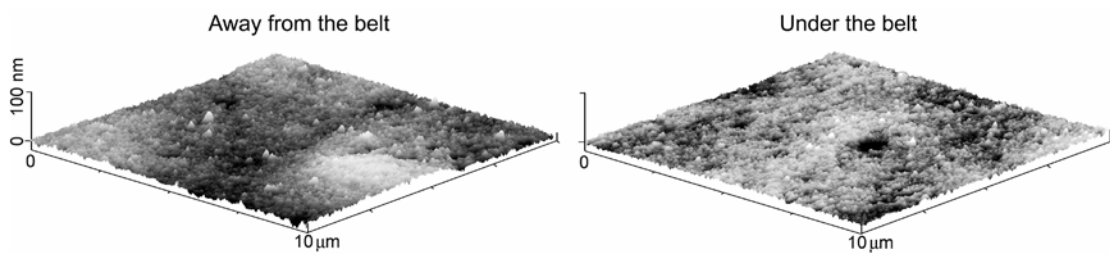


Figure 3.5: AFM images of the unworn tape.

3.3 Experimental results and discussion

3.3.1 Tests at ambient conditions

3.3.1.1 Tests run continuously at ambient conditions

The tests were performed at 22° C and 45% RH. The first test was run continuously for 10000 cycles. The tape drive with the tape cartridge loaded was placed inside of the environmental chamber 24 hours prior to the test. This test was run to form a baseline for successive testing (Fig. 3.6 (a)). In order to assure reproducibility of the results the test was repeated (Fig. 3.6 (b)). The trends observed for head output during both test tests were the same. It should be noted that trends in the variation of head output observed in the present study are different from those reported by Kattner and Bhushan [2000b]. It appeared that in the previous study [Kattner and Bhushan, 2000b] the drive was operated with automatic gain control turned on. The automatic gain control adjusts the gain of the amplifier of the drive electronics in order to maintain the amplitude of the reproduced signal, which masks the variations of the head output due to the changes at the head-tape interface. The problem was eliminated in the present study and the required set of commands was used, which set the gain of the amplifier at a fixed value.

Figure 3.6 (a) shows variation of head output, coefficient of friction, and the number of dropouts per minute with the number of cycles for the test performed at 22° C and 45% RH. Figure 3.6 (c) shows data on an expanded scale for the first 2500 cycles. Note that, head output increased from 0 dB at the beginning of the test to 0.5 dB at 150 cycles. Burnishing of the highest tape asperities, resulting in a decrease in head-tape separation, caused the increase. With the number of cycles increasing head output gradually decreased to -1.7 dB at 1800 cycles and remained at this level up to 6000

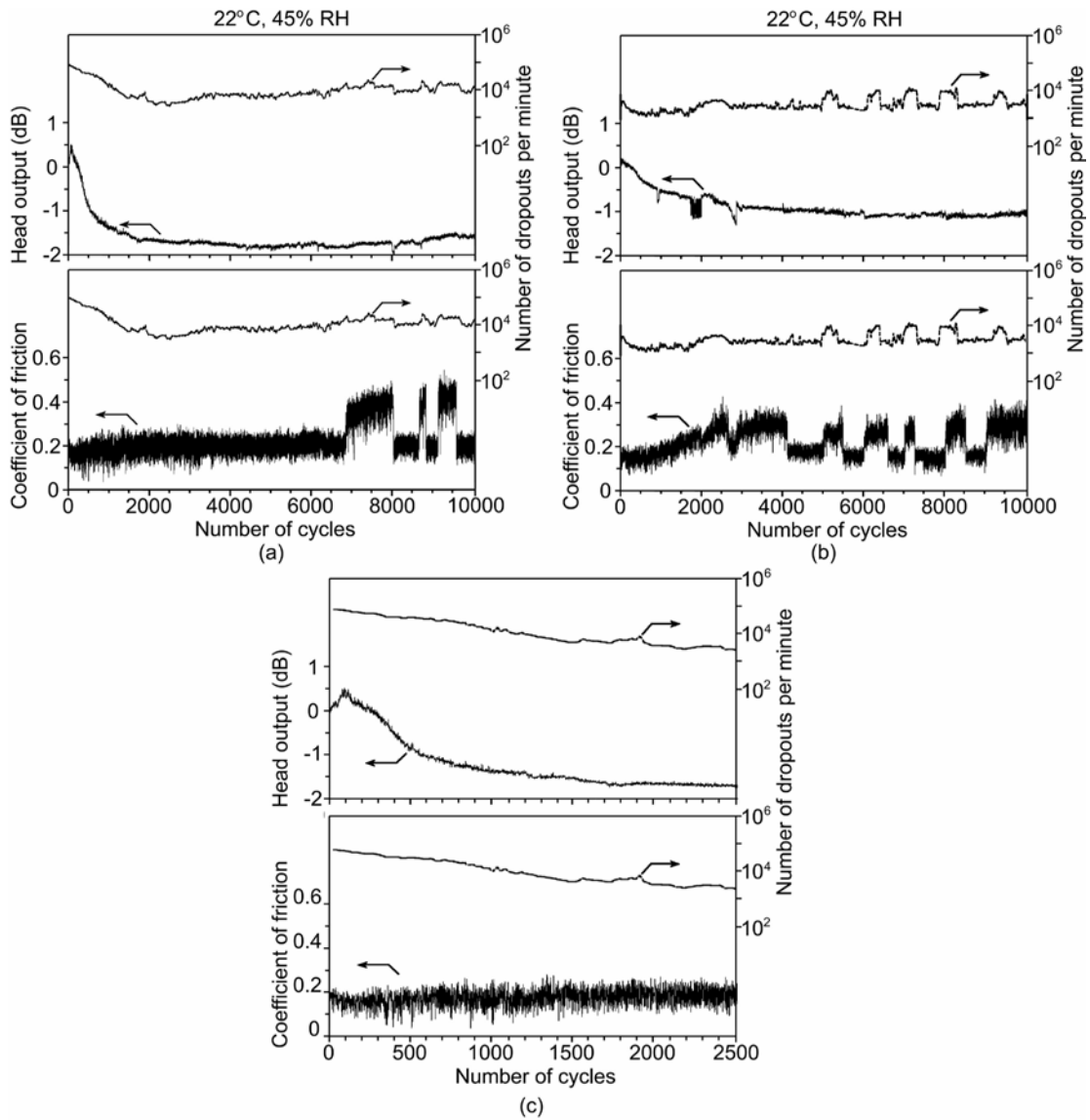


Figure 3.6: (a) Head output, coefficient of friction, and number of dropouts per minute (> 12 dB, $6-9 \mu\text{s}$) as a function of number of cycles for the test performed at 22°C and 45% RH. (b) Head output, coefficient of friction, and number of dropouts per minute as a function of number of cycles for another test performed at 22°C and 45% RH showing reproducibility of the results. (c) Data at an expanded scale for the first 2500 cycles from (a).

cycles, after which a slow increase to -1.5 dB at the end of the test was observed. The latter drop in head output will be discussed later. Coefficient of friction (Fig. 3.6 (a)) dropped from 0.18 at the beginning of the test to 0.15 during the first 200 cycles, after which it slowly increased to 0.17 at 1800 cycles and remained constant up to 6800 cycles, when it increased to 0.35-0.4 over 50 cycles and remained at this value for 1000 cycles. An abrupt decrease in coefficient of friction to 0.18 occurred at 7800 cycles. At 8600 and 9100 cycles, two sharp increases in coefficient of friction up to 0.3-0.4 were observed, each followed by an abrupt decrease to 0.18 at 8750 and 9800 cycles, respectively. The number of dropouts per minute was the highest (8×10^4 count/min) at the beginning of the test. It decreased during the first 1800 cycles and reached its minimum (3×10^3 count/min) for the test at 2400 cycles. Then, it leveled off at 5×10^3 count/min and remained constant up to 6400 cycles. At this point, the number of dropouts per minute increased to 2×10^4 count/min. This rate was observed up to 8000 cycles when a decrease in the number of dropouts to 8×10^3 count/min occurred. The number of dropouts increased to 2×10^4 count/min twice after that (at 8600 and 9000 cycles) and remained at a higher level for 200 and 600 cycles, respectively.

It is observed from Fig. 3.6 (a), that head output, coefficient of friction and the number of dropouts per minute correlate to each other. The decrease in head output in the range from 150 to 1800 cycles is accompanied by a decrease in the dropout rate. Head output, coefficient of friction and the number of dropouts per minute remain constant in the range from 1800 to 6800 cycles. At 6800, 8600 and 9100 cycles the increase is observed in both coefficient of friction and the number of dropouts per minute. That is followed by a simultaneous decrease at 7800, 8750 and 9800 cycles, respectively.

Anderson and Bhushan [1996] established that some dropouts correlate to changes in coefficient of friction. In a rotary tape drive a dropout was accompanied by an increase in coefficient of friction. Tape debris, loose or adherent, was found to be responsible for the correlation. However, at the beginning of the test the trends were opposite: increase in coefficient of friction was accompanied by a decrease in the number of dropouts per minute.

Figure 3.11 (to be presented later) shows optical images of different regions of the tape head worn at 22° C and 45% RH. The optical image of the unworn head is given for reference. The central row on Fig. 3.11 shows the head region near the belt edge. A distinct border is observed between the two areas on the faceplate at the head region near the belt edge (Fig. 3.11, central row). Black flaky debris was found only at the faceplate edges over the head region under the belt (Fig. 3.11, bottom row). The tape became smoother during the test (Table 3.2). High isolated asperities, in the size of head cleaning agent particles, were present over the tape region under the belt (Fig. 3.12, to be presented later).

To measure the recession of the thin-film region, AFM images of the heads were taken. Fig. 3.7 (a) shows AFM images and the averaged cross-sections of the thin-film region of the unworn head and at the end of the test. The read head recession increased from 14 nm for the unworn head to 40 nm after 10000 cycles. To detect elemental composition of the transfer material on the worn head, Auger analysis of virgin head and the head worn for 10000 cycles at 22° C and 45% RH was performed. Both heads were placed into the Auger analyzer 48 hours prior to taking of the spectra. Significant charging of the surface occurred during scanning the thin-film region under the cartridge

T (°C)	% RH	Under the belt	σ (nm)	P-V (nm)	S_k	K	β^* (μm)	
							y	x ^{a)}
Unworn		Yes	12±0.4	129±16-7	0.17±0.0	3.31±0.23	4.8	4.3
		No	12±0.5	135±10	-0.18±0.11	3.26±0.15	7.5	7.8
22	45	Yes	9.0±0.4	97±12	0.12±0.15	4.15±0.51	5.1	>40
		No	8.1±0.2	76±6.3	-0.13±0.14	3.12±0.15	5.4	5.0
10	20	Yes	9.0±0.6	200±36	0.20±0.12	5.42±2.15	4.6	5.5
		No	9.4±0.4	125±24	-0.22±0.08	3.44±0.26	4.8	>40
30	80	Yes	9.6±1.2	132±11	0.27±0.19	5.94±0.86	4.4	6.4
		No	8.3±0.6	79±7.8	-0.13±0.11	3.15±0.19	6.0	>40
10	80	Yes	9.7±0.6	117±24	0.12±0.13	3.82±0.23	5.4	>40
		No	9.1±0.5	95±16	-0.13±0.09	3.23±0.19	5.2	>40
45	20	Yes	8.4±0.3	89±9.7	-0.01±0.12	3.08±0.10	5.2	>40
		No	8.5±0.4	87±12	-0.13±0.14	3.20±0.17	5.7	>40

a) Tape motion direction

Notations. σ is standard deviation of surface heights, P-V is the distance between the highest asperity and the lowest valley, S_k is skewness, K is kurtosis, β^* is correlation length (the length over which the autocorrelation drops to 0.1 of its original value)

Table 3.2: Roughness statistics of virgin and worn MP tape measured using an AFM (80×80 μm). Roughness data are based on five sets of measurements.

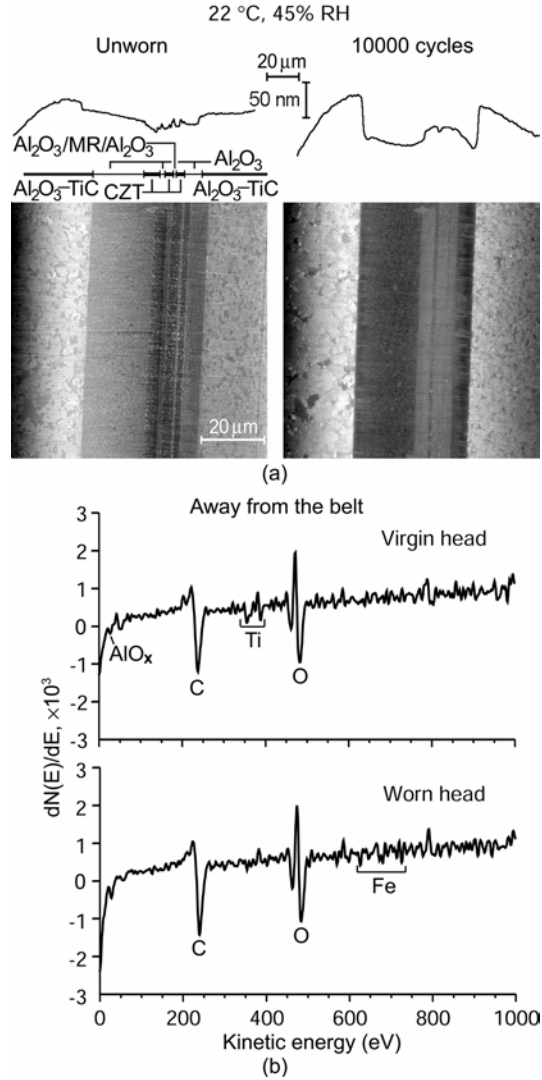


Figure 3.7: (a) AFM analysis (averaged cross sections and the gray scale AFM images) of the thin-film region of the MR head before and after the test performed at 22 °C and 45 % RH. Vertical scale from black to white is 200 nm. Brighter areas correspond to higher points. (b) AES analysis of virgin head and the head worn for 10000 cycles at 22° C and 45% RH.

belt with the electron beam even at low (2 kV) accelerating voltage and low (1 nA) beam current, which resulted in spectra shifts and prevented us from identifying elemental composition. Figure 3.7 (b) shows AES spectra obtained over the head region away from the belt for virgin head and the head worn for 10000 cycles at 22° C and 45% RH. Both alumina and titanium can be distinguished for the virgin head. The corresponding peaks cannot be identified for the head worn at ambient conditions, which, we believe, is due to the stain present at the surface. A weak triple peak, corresponding to elemental iron, appeared, which resulted from transfer of oxidized magnetic particles from the media. Based on AES results, we believe that stain is composed mainly of inorganic material.

3.3.1.2 Test with intermittent stops at ambient conditions

Another test was performed at 22° C and 45% RH in which the drive was stopped periodically, the head was removed from the drive and the recession of the read head was measured with the SAAFMM. After each SAAFMM measurement, the drive, with tape cartridge loaded, was placed in the environmental chamber at 22° C and 45% RH for 24 hours so that the components can reach the equilibrium; after this the test was continued.

Figure 3.8 (a) shows read head recession versus number of cycles and corresponding separation loss as calculated from Eq. 3.2. It should be noted, that the measured recession includes wear of the thin-film region as well as the thickness of stain present on the surface of both the read head and the substrate. Accumulation of stain on the read head due to the heating by the MR element resulted in the initial decrease of the measured recession [Kattner and Bhushan, 2000b]. With the number of cycles increasing wear of the thin-film region occurred. The read head recession reached its saturation [Scott and Bhushan, 2000, 2001]. It is also observed from optical (Fig. 3.8 (b)) and AFM

Figure 3.8: (a) Read head recession as a function of number of cycles of the head used in the test with intermittent stopping performed at 22 °C and 45 % RH; (b) optical micrographs of the thin-film region; and (c) the averaged cross sections and the gray scale AFM images of the thin-film region. Vertical scale from black to white is 200 nm. Brighter areas correspond to higher points.

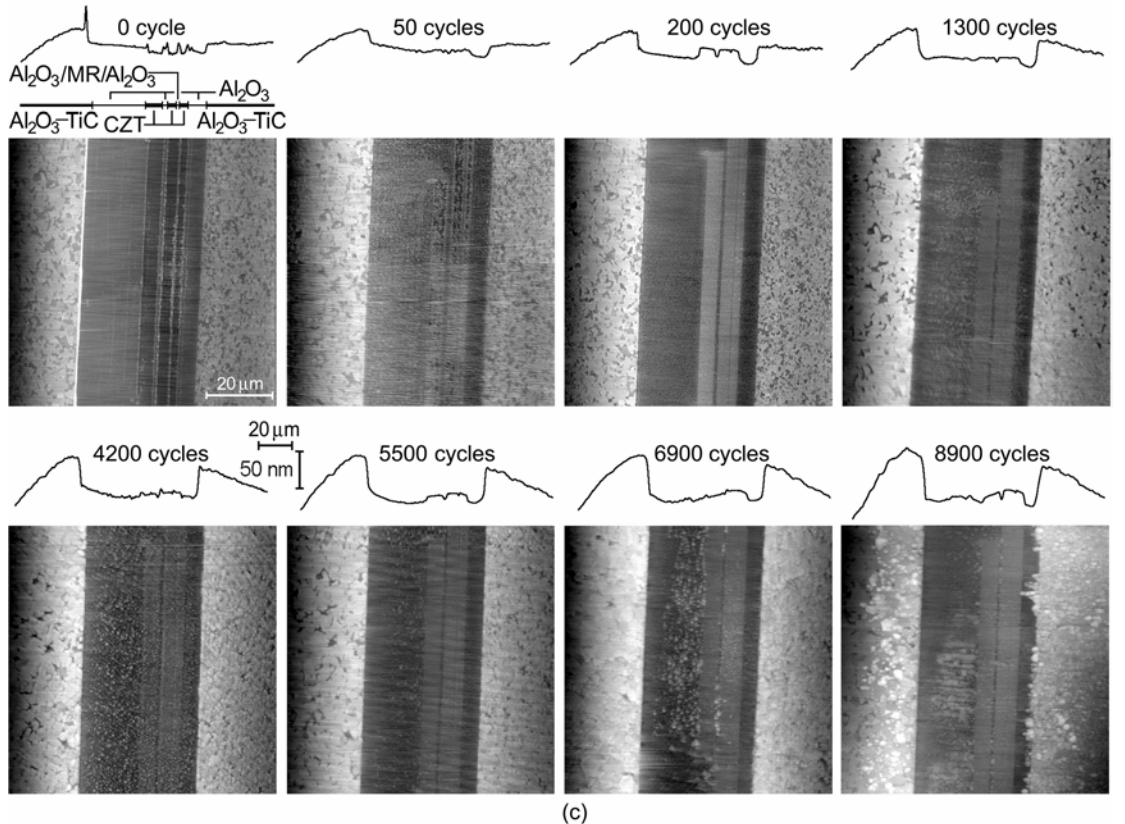
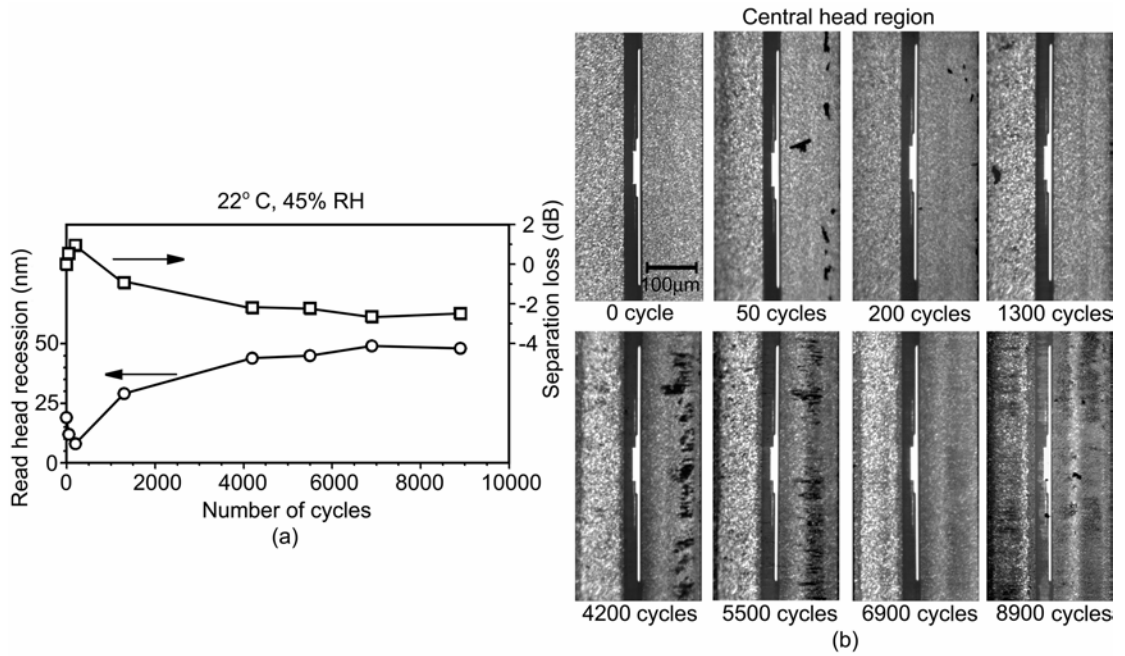


(Fig. 3.8 (c)) images of the thin-film region that debris accumulation started at some time between 1300 and 4200 cycles and continued to as the number of cycles increased.

There is a clear evidence of growth in read head recession and stain buildup, which results in an increase in the head-tape separation responsible for reduction of head output.

3.3.2 Tests performed at extreme operating conditions

The tape drive and the tape operating envelope (Fig. 3.3) is 5-45° C and 20-80% RH with a maximum wet bulb temperature of 26° C, as specified by the manufacturer. The tests were performed at the corners of the operating envelope at 10° C and 20% RH, 10° C and 80% RH, 30° C and 80% RH, and 45° C and 20% RH. The environmental chamber used in the study imposed a limitation on achievable low temperature. The requirement of the maximum wet bulb temperature of 26° C limits the maximum temperature to 30° C at 80% RH.

Figure 3.9 shows variation of head output, coefficient of friction and number of dropouts per minute (>12 dB, 6-9 μ s) with the number of cycles for the tests performed at 10° C and 20% RH, 10° C and 80% RH, 30° C and 80% RH, and 45° C and 20% RH. Figure 3.10 shows AFM images and the averaged cross-sections of the thin-film region of the unworn heads and the worn heads at the end of testing. Figure 3.11 shows optical images of different regions of worn tape heads. The optical image of the unworn head is given for reference. Table 3.2 presents roughness statistics of the unworn and worn MP tape measured using the large sample AFM (80 \times 80 μ m). Figure 3.12 shows selected AFM images of the unworn and worn MP tape regions under and away from the cartridge

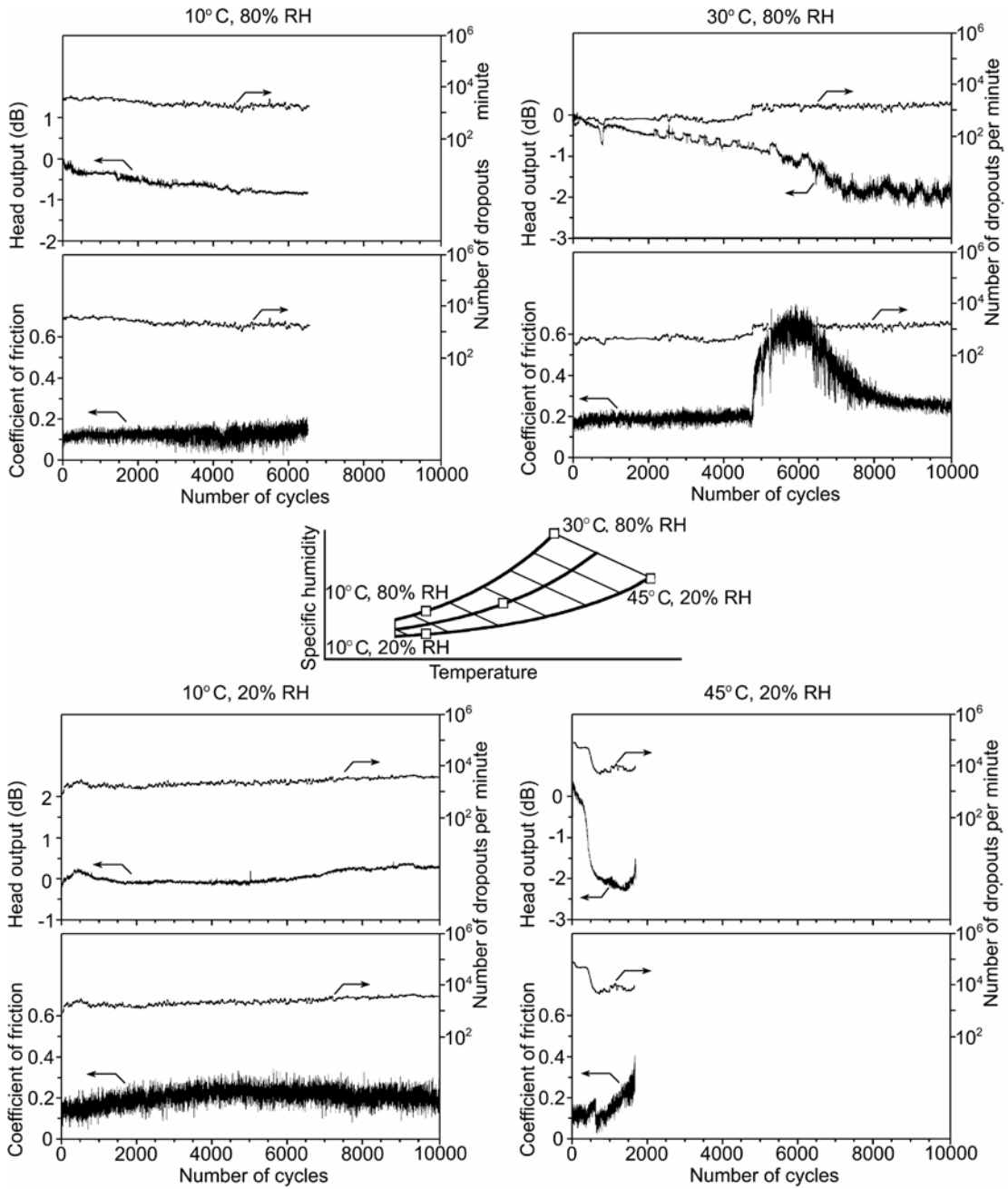


Figure 3.9: Head output, coefficient of friction, and number of dropouts per minute (> 12 dB, 6-9 μ s) as a function of number of cycles for the tests performed at extreme operating conditions.

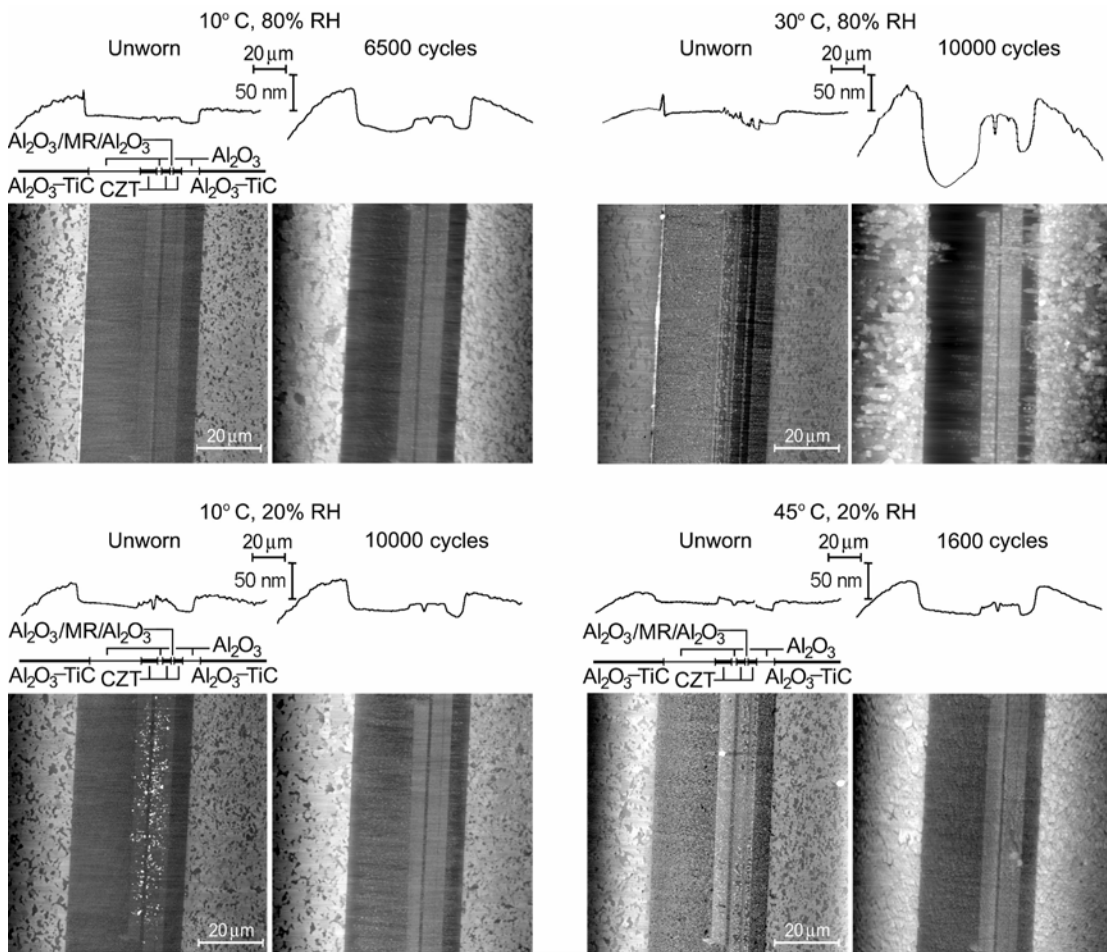


Figure 3.10: AFM analysis (averaged cross sections and gray scale AFM images) of the thin-film region of the MR head before and after the tests performed at extreme operating conditions. Vertical scale from black to white is 200 nm. Brighter areas correspond to higher points.

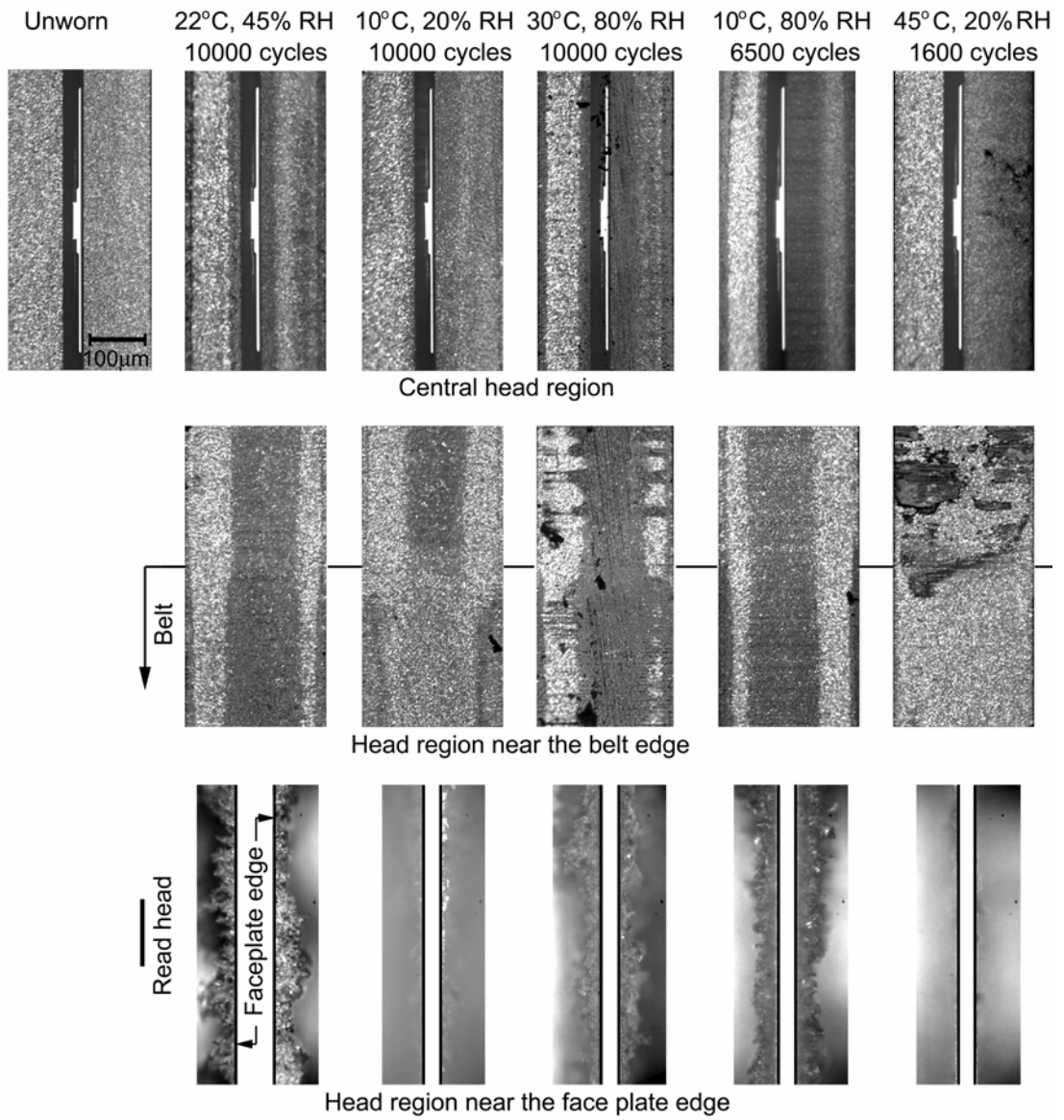


Figure 3.11: Optical images of different regions of worn tape heads.

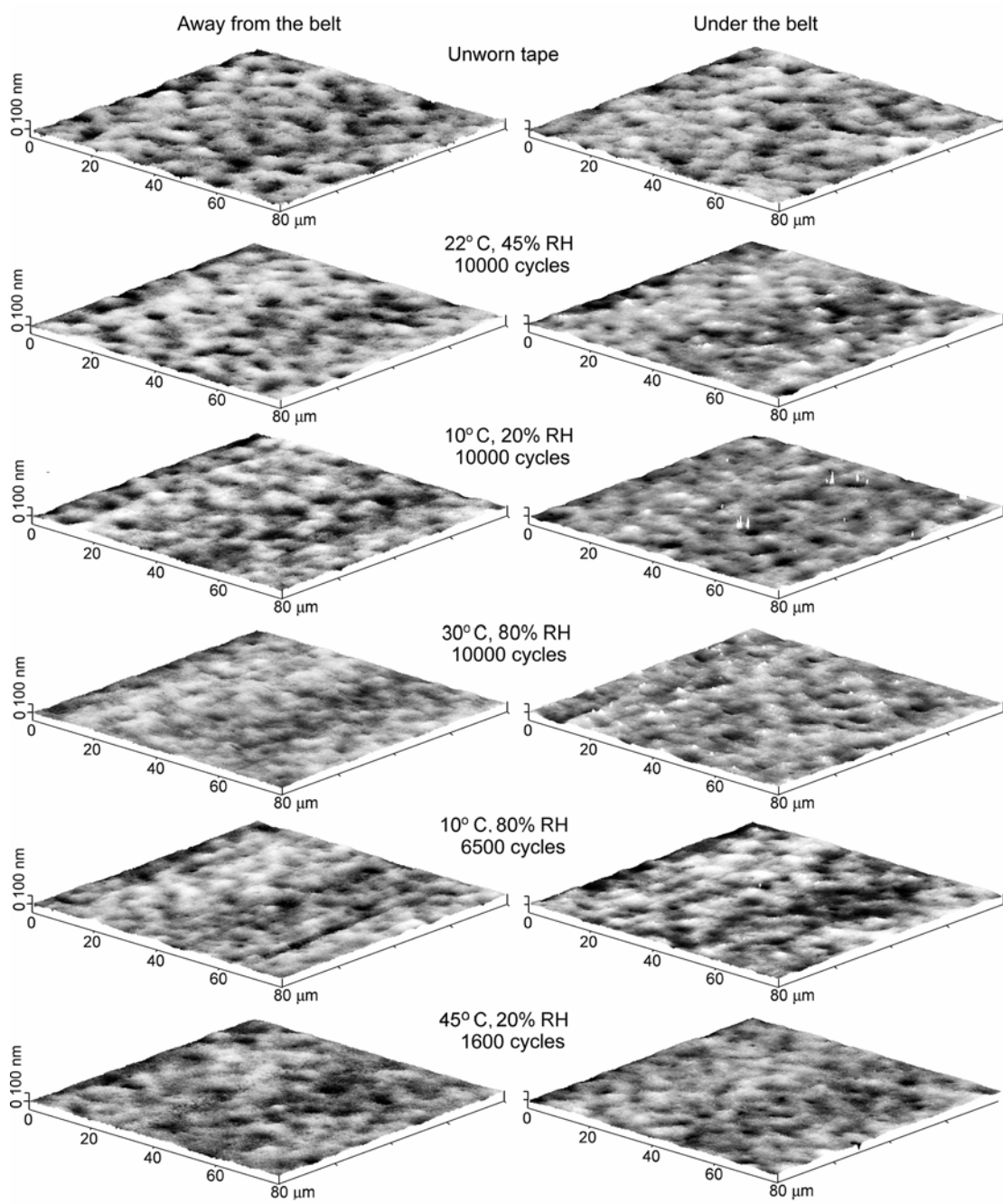


Figure 3.12: AFM images of the unworn and worn MP tape.

belt. Table 3.3 summarizes change in read head recession, corresponding separation loss as calculated from Eq. 3.2, and change in head output from the beginning to the end of the tests.

T (°C)	% RH	Test duration (cycles)	Read head recession (nm)			Separation loss (dB) ^{a)}	Measured change in head output (dB)
			Unworn head	End of test	Change		
22	45	10 000	14	40	26	-2.2	-1.6
10	20	10 000	11	24	13	-1.1	0.3
10	80	6 500	20	33	13	-1.1	-0.8
45	20	1 600	6	38	32	-2.7	-2.5
30	80	10 000	31	35	4	-0.3	-1.9

^{a)} The separation loss value was calculated using Wallace equation for $\lambda=0.64 \mu\text{m}$

Table 3.3: Summary of the measured read head recession, and calculated and measured separation loss.

3.3.2.1 Test at 10° C and 20% RH

Figure 3.9 (bottom left) shows variation of head output, coefficient of friction and the number of dropouts per minute (>12 dB, 6-9 μs) with the number of cycles for the

tests performed at 10° C and 20% RH for 10000 cycles. Head output dropped from 0 dB to -0.2 during the first 20 cycles. This was followed by an increase up to 0.2 dB at 500 cycles. At this point head output started decreasing and leveled off at 0 dB at 1600 cycles and remained at that level up to 5600 cycles. A further increase in the number of cycles resulted in the increase of head output up to 0.25 dB at the end of the test. Coefficient of friction gradually increased from 0.17 at the beginning of the test to a maximum of 0.22 at about 5000 cycles. After that, it remained almost constant through the remainder of the test. The number of dropouts per minute (>12 dB, 6-9 μs) was minimal during the first 25 cycles (900 count/min). A broad local maximum is observed at 500 cycles. The number of dropouts per minute increased from 1600 count/min at 1000 cycles to 4000 count/min at 10000 cycles.

Figure 3.10 (bottom left) shows AFM images and the averaged cross-sections of the thin-film region of the unworn head and the worn head at the end of the test performed at 10° C and 20% RH. The read head recession increased from 11 nm for the unworn head to 24 nm for the worn head after 10000 cycles. Figure 3.11 shows optical images of different regions of the tape head worn at 10° C and 20% RH. A small amount of shiny debris was found only at the faceplate edges over the head region under the belt (Fig. 3.11, bottom row). The tape did not become smoother during the test as compared to the unworn tape (Table 3.2). High values of σ and P-V parameters for the tape region under the belt are due to the presence of debris on the surface. Scratches are observed on the tape surface over the region away from the belt.

3.3.2.2 Test at 10° C and 80% RH

Figure 3.9 (top left) shows variation of head output, coefficient of friction and the number of dropouts per minute (>12 dB, 6-9 μ s) with the number of cycles for the tests performed at 10° C and 80% RH. The test failed after 6500 cycles. The drive motor was not able to move the tape in the cartridge at the very beginning of the forward pass after the drive was stopped for 5 s. Following this failure, the cartridge was removed from the drive, disassembled and carefully examined. No obvious signs of failure such as tape rupture, tape stiction to the guides, belt rupture and/or misalignment were found. An attempt was made to initiate the tape motion manually and the attempt was successful. The tape in the tape cartridge preserved its mobility. Then, data from the test were processed and coefficient of static friction at the beginning of each forward pass was calculated. It was observed, that coefficient of static friction was as high as 0.7 to 0.9 during the last 1000 cycles of the test. Based on these findings, we concluded that the test failed due to high stiction at the head-tape interface.

Head output (Fig. 3.9, top left) gradually decreased from its initial value of 0 dB at the beginning of the test to -0.8 dB at failure. Coefficient of friction did not change significantly throughout the test. However, its scatter increased at about 3000 cycles and a tendency to growth was observed starting at 4500 cycles. The number of dropouts per minute remained in the range of $(2-4) \times 10^3$ count/min.

Figure 3.10 (top left) shows AFM images and the averaged cross-sections of the thin-film region of the unworn head and at the end of the test performed at 10° C and 80% RH. The read head recession increased from 20 nm for the unworn head to 33 nm for the worn head after 6500 cycles. The gap between the write pole/read shield and read

shield of the read head cannot be distinguished. Figure 3.11 shows optical images of different regions of the tape head worn at 10° C and 80% RH. The central row on Fig. 3.11 shows the head region near the belt edge. A distinct border is observed between the two areas at the faceplate edges at the head region near the belt edge (Fig. 3.11, central row). Black flaky debris was found only at the faceplate edges over the head region under the belt (Fig. 3.11, bottom row). The tape became smoother during the test (Table 3.2). Scratches are observed on the tape surface over the region away from the belt.

3.3.2.3 Test at 30° C and 80% RH

Figure 3.9 (top right) shows variation of head output, coefficient of friction and the number of dropouts per minute (>12 dB, 6-9 μ s) with the number of cycles for the tests performed at 30° C and 80% RH for 10000 cycles. Head output fluctuated around 0 dB for the first 200 cycles. It decreased slowly to -0.3 dB at 700 cycles whereupon it dropped to -0.7 dB for a period of 100 cycles and increased again to -0.3 dB over a period of 60 cycles. That was followed by a gradual decrease to -0.45 dB at 2200 cycles at which a series of sudden increases of 50-150 cycles in duration and 0.1-0.2 dB in magnitude occurred. This behavior was observed up to 5000 cycles. At above 5000 cycles the scatter increased markedly. The overall trend was decreasing. At 6000 cycles the rate of the head output decrease, increased and at 7200 cycles a new level of -1.8 dB was reached. With a further increase in the number of cycles, head output experienced quasi-periodic changes on the range of -2.1 to -1.5 dB until the test was stopped. Coefficient of friction increases from 0.17 to 0.19 during the first 400 cycles. For the next 4300 cycles its value was in the range of 0.18-0.20. At 4700 cycles an increase in coefficient of friction began, its value increased to 0.6 at 6000 cycles. For the next 2700

cycles coefficient of friction decreased and reached a lower value of 0.25 at 8700 cycles; it remained at this level to the end of the test. The number of dropouts per minute increased from 400-500 during the first 4500 cycles to 1400 at 4700 cycles and remained constant until the end of the test. As observed from Fig. 3.8, the increase in coefficient of friction at 4700 cycles was followed by an increase in the dropout rate and a decrease in head output.

A distinct correlation was observed between head output and another class of dropouts of lower magnitude and shorter duration. Figure 3.13 shows variation of head output and the number of dropouts per minute (6-9 dB, 6-9 μ s). A higher number of dropouts per minute correspond to a lower head output.

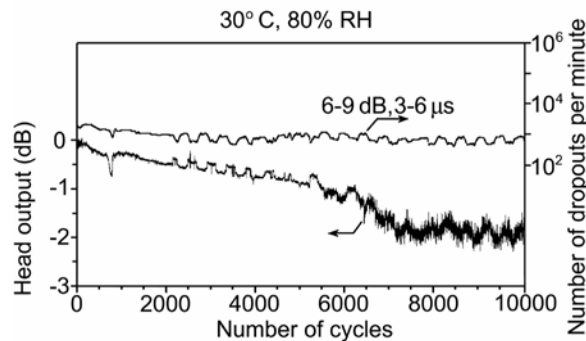


Figure 3.13: Head output and the number of dropouts per minute (6-9 dB, 3-6 μ s) as a function of number of cycles for the test performed at 30 °C and 80 % RH.

Figure 3.10 (top right) shows AFM images and the averaged cross-sections of the thin-film region of the unworn head and the worn head at the end of the test performed at 30° C and 80% RH. The read head recession increased from 31 nm for the unworn head to 35 nm after 10000 cycles. It was observed that both substrates were covered with debris and the recession of the alumina overcoat and undercoat were high. Figure 3.11 shows optical images of different regions of the tape head worn at 30° C and 80% RH. The central row on Fig. 3.11 shows the head region near the belt edge. No distinct border was observed between the two areas on the faceplate at the head region near the belt edge (Fig. 3.11, central row). Black flaky debris was found only at the faceplate edges over the head region under the belt (Fig. 3.11, bottom row). The tape became smoother during the test (Table 3.2) only over the region away from the belt. High isolated asperities were present over the tape region under the belt (Fig. 3.12).

3.3.2.4 Test at 45° C and 20% RH

Figure 3.9 (bottom right) shows variation of head output, coefficient of friction and the number of dropouts per minute (>12 dB, 6-9 μ s) with the number of cycles for the tests performed at 45° C and 20% RH. The test failed after only 1600 cycles. The drive motor was not able to move the tape in the cartridge at the very beginning of the forward pass after the drive was stopped for 5 s. The cartridge was removed from the drive, disassembled and carefully examined. It was found that the backside of the tape got stuck to one of the guides. As a result, the tape in the tape cartridge was not able to move. Then, data from the test were processed and the coefficient of static friction at the beginning of each forward pass was calculated. It was found, that coefficient of static

friction did not exceed 0.6 throughout the test. Based on these findings, we concluded that the test failed due to high stiction at tape backcoat-cartridge guide interface.

Head output increased from 0 dB to 0.25 dB (Fig. 3.9, bottom right) during the first 20 cycles. It decreased at a moderate rate to -0.3 dB at 300 cycles, at which point a decrease to -2 dB occurred over the next 300 cycles. At 600 cycles the decrease slowed down, and head output reached its minimum value of -2.4 dB at 1400 cycles. With a further increase in the number of cycles, head output increased and the rate at which it grew, steepened just before the drive failed. Coefficient of friction increased from 0.13 to 0.16 during the first 600 cycles, then abruptly dropped to 0.08-0.1 over 10 cycles and finally increased to 0.35 at failure. Number of dropouts per minute followed the trend for the head output. It was maximum during the first 25 cycles (8×10^4) and had increased by an order of magnitude when it reached 800 cycles.

Figure 3.10 (bottom right) shows AFM images and the averaged cross-sections of the thin-film region of the unworn head and the worn head at the end of the test performed at 45° C and 20% RH. The read head recession increased from 6 nm for the unworn head to 38 nm after 1600 cycles. It was observed that both the substrate and the thin-film region are covered with flaky stain and/or debris. Figure 3.11 shows optical images of different regions of the tape head worn at 45° C and 20% RH. The central row in Fig. 3.11 shows the head region near the belt edge. A distinct border is observed between the two areas on the faceplate at the head region near the belt edge (Fig. 3.11, central row). Large debris were present on the faceplate over the head region away from the belt. No visible debris was detected at the faceplate edges. The tape became smoother during the test over its full width (Table 3.2).

3.4 Discussion of environmental effects

Figure 3.14 presents summary of variation of head output, coefficient of friction and the number of dropouts per minute with the number of cycles for the tests performed at different environmental conditions. Figure 3.15 shows a summary of durability data, the range of variation for head output and coefficient of friction, and the change in the read head recession. As observed from Fig. 3.15, variation in head output and coefficient of friction was large during all tests. As observed from Fig. 3.14, an increase in both temperature and relative humidity deteriorated drive performance, with the worst performance at the highest temperature.

It has been reported that tribological and magnetic performance of head-tape interface in a linear tape drive with a belt driven cartridge at ambient conditions is governed by stain formation and removal [Kattner and Bhushan, 2000a, 2000b]. Once stain builds up to a certain thickness it gets removed. It has been found, that variations in stain thickness and read head recession are responsible for the variations of head output. Stain buildup and growth in the read head recession decrease head output. Stain removal leads to an increase in coefficient of friction and results in an increase in the number of dropouts per minute. However, stain acts as a protective layer and a lubricant, thus decreasing head wear. It is also known from literature [Bhushan and Hahn, 1995; Scott and Bhushan, 2000], that stain readily forms at relative humidity less than 40-45% and consists of mainly inorganic material. In order to estimate the amount of deposits formed at the surface of the heads used in the present study, AFM analysis was performed on the heads. Prior to measurements, the heads were cleaned with a dry cotton swab. Figure 3.16 shows AFM images of the air-bearing surface of the worn heads. The image of the

unworn heads is given for reference. As observed from Fig. 3.16, transfer of material occurred on the air bearing surface of all heads. This transfer could not be removed by a

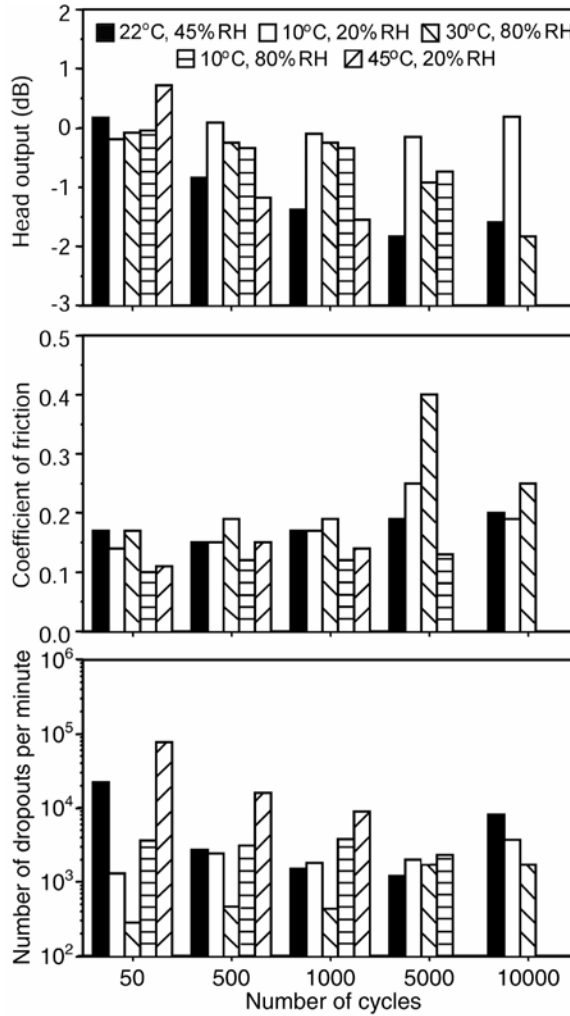


Figure 3.14: Head output, coefficient of friction and the number of dropouts per minute (> 12 dB, 6-9 μ s) as a function of number of cycles for all tests.

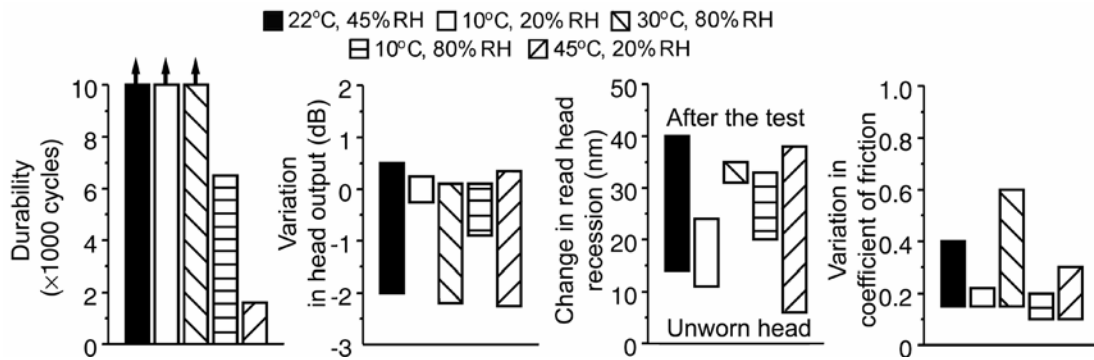


Figure 3.15: Durability of the tests, the range of variation for head output and coefficient of friction, and the change in the read head recession during the tests performed at different environmental conditions.

cotton swab and is adherent debris or stain. At low relative humidity and low temperature and at ambient conditions stain is thicker. Certain amount of stain buildup at low relative humidity and low temperature is responsible for good durability and stable head output. At all other conditions, interface wear is high which leads to read head recession. It is known from literature [Bhushan, 1996] that during prolonged exposure (few weeks) of magnetic tape to hot and/or humid environment hydrolysis of the binder occurs. High humidity results in formation of meniscus bridges and hydrolysis of the binder system. High temperature results in softening and hydrolysis of the binder system.

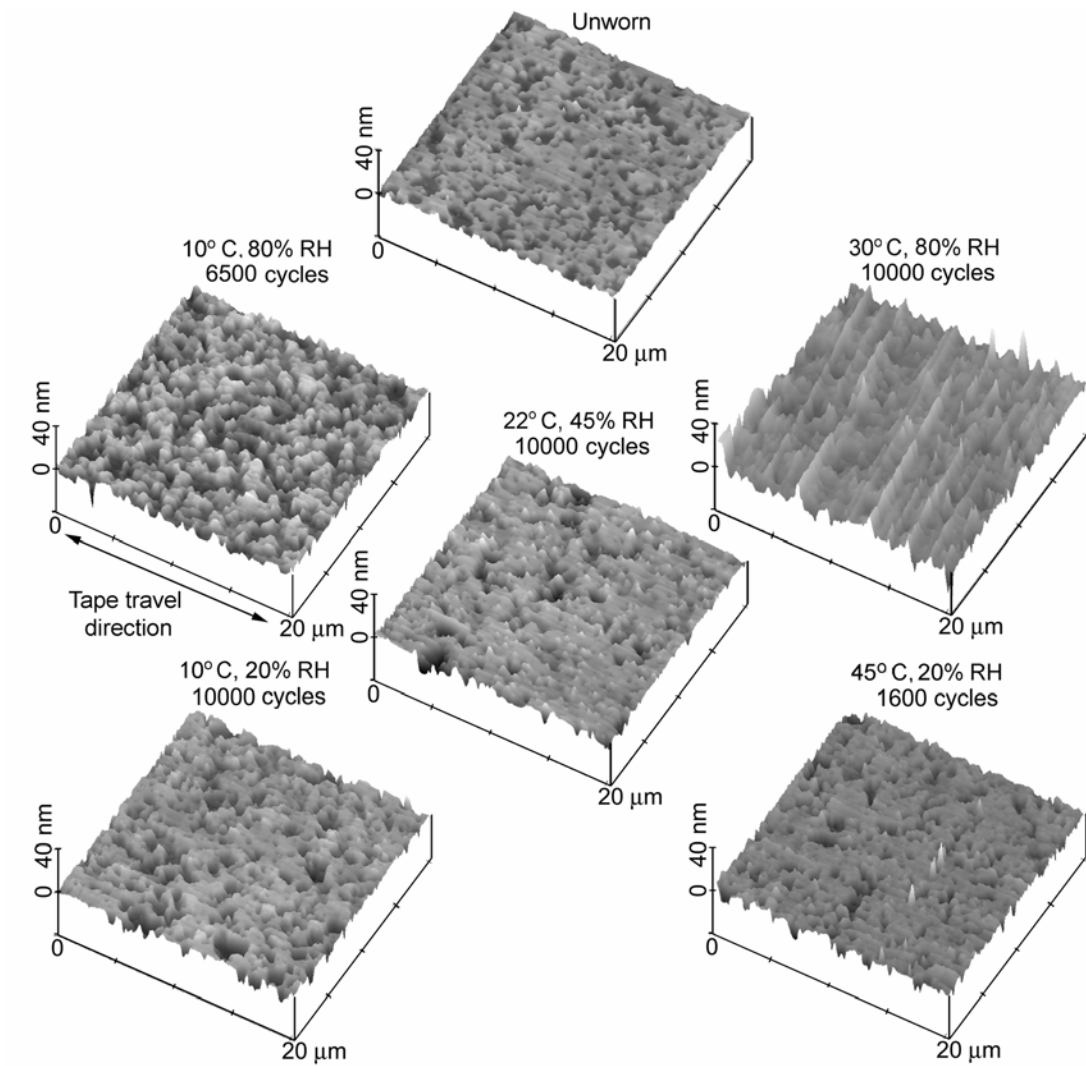


Figure 3.16: AFM images of the head air-bearing surface at the end of the tests performed at different environmental conditions after cleaning with a dry cotton swab.

3.5 Summary

Based on the tests performed in a linear tape drive with a belt driven cartridge at ambient environmental conditions and at the corners of the operating envelope as specified by the manufacturer, following conclusions are drawn.

Magnetic and tribological performance of the head-tape interface is the best at low temperature and low relative humidity. Increase in both temperature and humidity results in performance degradation with the worst performance at the highest temperature.

High humidity results in formation of meniscus bridges and hydrolytic binder degradation after sliding for several days, which is responsible for high friction and wear.

High temperature results in binder softening and hydrolytic degradation at high humidity, which is responsible for high friction and wear.

CHAPTER 4

EFFECT OF PARTICULATE CONTAMINATION ON POLE TIP RECESSION IN A LINEAR TAPE DRIVE

4.1 Introduction

Particulate contamination is an important issue in the performance and durability of magnetic storage media, as the flying height at the head-tape interface decreases for high recording density [Bhushan, 1996]. Particles that may interact with the head-tape interface can have two different sources: contaminant particles from the operating environment and wear particles that are generated at the interface itself. Particles from both sources can act as abrasives, which cause three-body abrasive wear of magnetic tape and tape heads and deteriorate magnetic performance during normal operation of a tape drive.

Magnetic heads used in tape and disk drives are made of multiphase materials. In inductive heads, relatively hard (typically ceramic) phases are used as substrates because they are highly wear resistant, while relatively soft magnetic metal pole phases and insulating thin films are used [Bhushan, 1996]. Differential wear, which is caused by differences in wear rates among the different phases, causes the softer poles to recede from the air bearing surface or substrate; this phenomenon is called pole tip recession

(PTR). A schematic of a thin-film inductive tape head showing the definition of PTR is presented in Fig. 4.1. All of the shaded and hatched regions in the figure depict materials that are deposited as thin films. The thin-film region (the region where the writing to the media actually takes place) consists of an undercoat, north and south magnetic poles, a gap (between the poles), and an overcoat. The function of the undercoat is to “planarize” the relatively rough substrate wafer before the poles are deposited. The rest of the structure is deposited on top of the undercoat. Since the substrate may be electrically conductive, the undercoat also insulates the copper coils from the substrate. After the poles are deposited the film is not planar, so a relatively thick overcoat must be deposited to create a planar surface so that the substrate closure can be glued on.

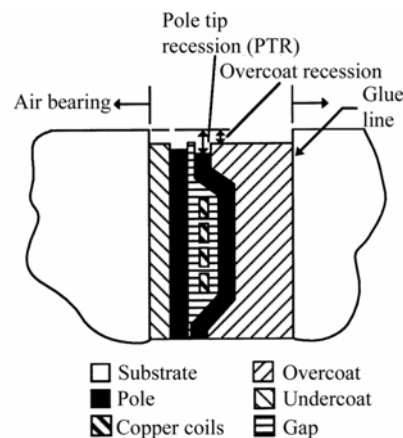


Figure 4.1: Cross-section schematic of a thin-film inductive tape head showing the definitions of PTR and overcoat recession.

The increased spacing caused by PTR results in lower write density, so the recession must be minimized. Scott and Bhushan [2000] review the recent research on PTR in tape heads. Tsuchiya and Bhushan [1995] proposed a wear mode for PTR. They proposed that wear particles are initially produced from the soft thin-film region of the head. Debris particles, of course, may also originate from the tape. Head cleaning agents (HCAs), which are alumina particles used in formulation of metal particle (MP) tape, are certainly hard enough to cause wear of the thin-film region. These particles are trapped at the interface and result in growth in PTR by three-body abrasion. They suggested that three-body abrasion must be the wear mode for PTR because tape asperities are not able to reach the recessed thin-film surface of the head to a significant extent; tape asperities are not large enough to reach the recessed material and tape cannot bend into the recess. They experimentally verified the proposed mechanism using an optical interferometry technique to measure differences in real area of contact of tape in contact with a top surface and of tape in contact with a fabricated recess. The real area of contact was much lower over the recess, implying that wear of the recessed region cannot occur by direct contact with the tape. Three-body abrasive wear modes for PTR were also proposed for tape heads and disks by Harrison et al. [1998] and Xu and Bhushan [1998], respectively. Scott et al. [2001] present evidence that reducing the number of three-body particles at the interface reduces PTR.

Scott and Bhushan [2002] performed an extensive experimental and theoretical study of micro/nano-scale differential wear of multiphase materials resulting in PTR in magnetic-tape heads. An analytical model that accounts for the observed wear was presented. The authors show both experimentally and analytically that each of the

following leads to higher differential wear: increasing the size of the three-body particles, increasing tape tension, and increasing the thin-film wear coefficient with respect to that of the substrate. An increase in the thin-film wear coefficient can be caused by a decrease in the thin-film hardness, an increase in the thin-film thickness or an increase in the number of particles at the interface. These results support the notion that three-body abrasion is the cause of differential wear (PTR) in tape heads. To study particles present at the head-tape interface during normal drive operation, the number and type of the particles that were found on heads slid against MP tape, heads exposed to the drive environment but not slid against the tape, and “clean” heads which were neither slid against the tape nor exposed to the drive environment, were extracted with solvents for analysis [Scott and Bhushan, 2002]. Bhushan et al. [1999] give a detailed schematic and procedure for the solvent extraction used. It was reported [Scott and Bhushan, 2002] that a substantial majority of the solvent-extracted particles found on heads slid against MP tape were generated by head-tape contact and that most wear particles originated from the tape. Some particles originating from the environment were also found. Almost all of the particles extracted after the drive tests were below 100 μm in length and the largest number of particles was 10-20 μm in length.

The results of experimental and theoretical studies show that three-body abrasion is the primary wear mode of the thin-film region in tape heads, resulting in differential wear (PTR). Only one source of the three-body particles, those originating at the head-tape interface, has been taken into account. We believe, that particulate contaminants, present in the drive operating environment, can be trapped at the head-tape interface and affect PTR [Scott and Bhushan, 2000, 2002; Tsuchiya and Bhushan, 1995]. The present

study is aimed at evaluation of the effect of particulate contamination on PTR of a thin-film head slid against MP tape in a linear tape drive. An experimental setup has been developed to inject loose particles into the head - tape interface at controlled levels during differential wear tests. Atomic force microscopy (AFM) is used to measure PTR at various points during the wear tests. The effect of particle concentration, size, and hardness on PTR is studied. AFM and scanning electron microscopy (SEM) analyses are employed to reveal changes at the tape head surface at the end of testing. The experimental results are supported by the simulation of PTR based on the analytical model developed by Scott and Bhushan [2002]. A possible mechanism responsible for the change in PTR with particle concentration and size is discussed.

4.2 Experimental

4.2.1 Test apparatus and procedures

All differential wear tests were conducted using a commercial Honeywell 96 linear tape drive at 22 °C and $45 \pm 5\%$ RH; a schematic for the drive is shown in Fig. 4.2. A vacuum pump and column are used to control tape tension. A head is mounted on a linear stage that penetrates into the tape path and controls head wrap angle. Loose particles were injected into the drive environment (a volume of approximately $42,000 \text{ cm}^3$), as shown in Fig. 4.2. The clean air filtered using a PTFE membrane filter (0.2 μm pore size, Gelman Sciences, Ann Arbor, MI) was continuously supplied to the fluid dispenser, the aerosol generation chamber, and the vacuum generator. Nitrogen was supplied to the fluid dispenser to inject iron metal particles (MP). The micron specification on the filters is meant for liquid filtration. For air, these filters are capable of eliminating particles smaller than the specified size. A suspension of alumina or metal

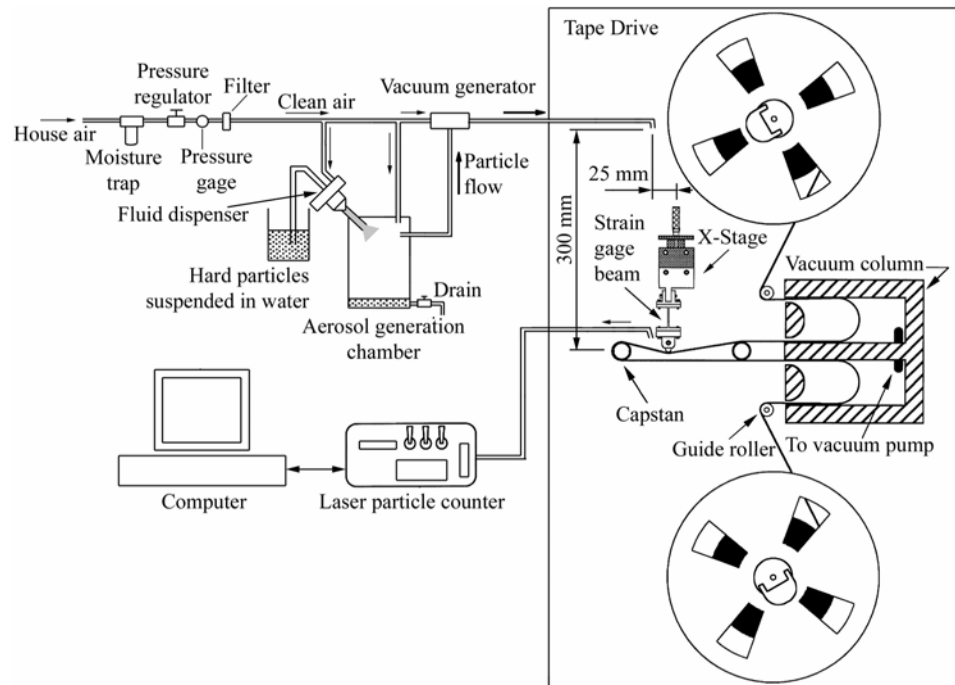


Figure 4.2: Schematic of the experimental setup.

particles in demineralized distilled water was subjected to ultrasonic agitation during the test to maintain a near constant concentration. The suspension was sprayed inside the aerosol generation chamber in the form of a pressurized spray using the fluid dispenser (METLAP 2000, Buehler Ltd., Lake Bluff, IL). The droplets containing the alumina or MP particles were suctioned out of the aerosol generation chamber with the help of the vacuum generator (PIAB Vacuum Products, model L20) and were introduced into the drive. During this process the liquid content of the droplets evaporated, leaving the solid

powder particles in a dispersed form inside the drive. The particles were injected downward inside the drive at a vertical distance of 300 mm and horizontal distance of 25 mm from the head-tape interface at a flow rate of 0.036 m³/s. The particle count in the vicinity (5 mm to the side of the head and 5 mm above the head-tape contact) of the head-tape interface was monitored with the help of a laser particle counter (PMS Inc., Boulder, Colorado, model ULPC-1001-CPC-2CH) with a sampling flow rate of 4.7×10⁻⁶ m³/s. Sampling was done continuously with a sampling interval of 5 min. Particle count was obtained in two different size bins of 0.1–0.3 μm and >0.3 μm. Measured particle size distribution was found to be consistent with the particle size distribution (S-shaped cumulative distribution) provided by the particle manufacturer. Tygon tubing of 6.35 and 9.5 mm ID were used together with standard tubing connectors in the flow network.

A number of drive tests was conducted. For each test, a head was placed in the mount and penetrated into the tape path, fully wrapping the tape over the head. First, a test in a class 10,000 laboratory environment with no particles injected was performed to create a baseline for future testing with contaminant particles injected. Class 10,000 is a typical operating environment for tape drives in information storage centers. Four drive tests with contaminant particles of various concentration, size, and hardness were conducted. The list of the contaminant particles and particle concentration used in the study is presented in Table 4.1. Both alumina and MP particles (cobalt-doped iron particles 0.08 μm in length of acicular shape with an aspect ratio of 6:1, passivated with a thin oxide layer) are used in the formulation of magnetic tapes. Alumina particles serve as head cleaning agents and serve as load bearing particles in magnetic tapes, thus

improving tape wear properties. MP particles dispersed in polymer matrix constitutes the magnetic layer to which information is recorded.

Particle type	Shape	Hardness (GPa) ^{a)}	Nominal size (μm)	Concentration (cm^{-3})
Al_2O_3	Spherical	22	90% <0.5	20
			90% <0.5	200
			90% <0.05	200
MP (iron)	Acicular	≤ 2.5	90% <0.08 b	200

^{a)} Xie and Bhushan, 1996.

^{b)} length. Particles have acicular shape with an aspect ratio of 6:1.

Table 4.1: Particles used in the study.

All drive tests were performed at tape tension of 2.2 N and speed of 1.5 m/s. For each test a single 600 m length of tape was run back and forth over the head and was stopped periodically to measure PTR using an AFM (StandAlone AFM, Digital Instruments, CA). The AFM was used in contact mode to take $80 \mu\text{m} \times 80 \mu\text{m}$ scans, in order to measure recession at four pole pairs across the head which are 1.2 mm apart. The

same four pole pairs were measured each time the test was stopped. For all measurements, the natural curvature of the head is removed during software post-processing of raw AFM data and recession is found with respect to the substrate surface on the left side, just adjacent to the thin-film region, as shown in Fig. 4.1. The measurements made at the four sites are averaged and the average is reported as the PTR and is plotted on all graphs. The 2-dimensional AFM scans across the thin-film region were averaged over the shorter pole length using a software option for AFM data post-processing. Scott and Bhushan [1999] give a detailed discussion on PTR measurement and software post-processing of raw AFM data.

4.2.2 Test specimen

Commercial tape heads were used in this study. Each head consists of three modules: one write module with 18 write pole pairs and two read modules, glued to each side of the write module. The entire head is 7 mm wide and 21 mm long, and has a 10 mm radius. The heads use slots in the direction transverse to the tape travel to bleed out air between the head and tape. Typical head-tape spacing for these heads is 40 nm [Scott et al., 2001]. Fig. 4.3 shows an optical micrograph and an AFM image of a pole pair. The pole material is rf-sputtered CZT and the supporting thin films are rf-sputtered Al_2O_3 . $\text{Al}_2\text{O}_3 - \text{TiC}$ is used as the substrate material. A double-layer MP tape (width = 12.7 mm, total/substrate thickness = 9/6.2 μm , magnetic/non-magnetic layer thickness = 0.3/2.0 μm , backcoat thickness = 0.5 μm) is used in all tests.

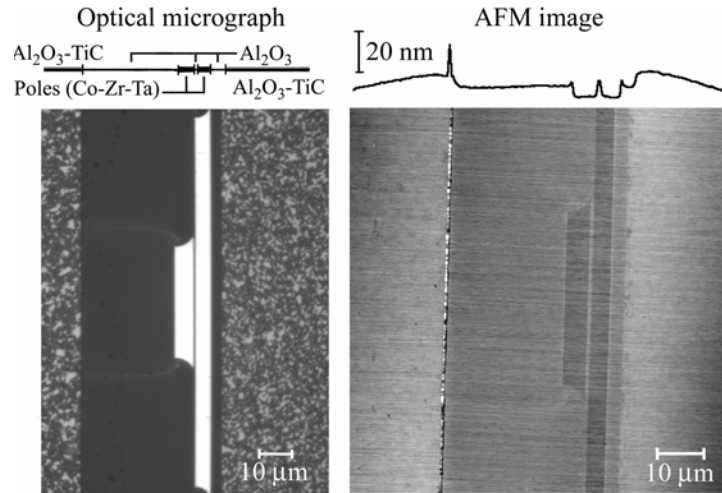


Figure 4.3: Optical micrograph and AFM image of the thin-film structure of the heads used in the study. The transition from black to white in the AFM image covers height range of 100 nm. Brighter areas correspond to higher points.

4.2.3 Analysis of the worn heads

The thin-film region of the tape heads run in the wear tests with different contaminant particles present in the drive environment were analyzed using SEM and AFM (Dimension 3100, Digital Instruments, Santa Barbara, CA). SEM images were taken at an acceleration voltage of 2 kV. Secondary electrons were collected for imaging. AFM images ($20 \mu\text{m} \times 20 \mu\text{m}$) were taken in contact mode with a Si_3N_4 tip that has a nominal tip radius of 30-50 nm. The data were taken at the end of testing, after the tape was run against the head for 500 km. The same pole pairs, for which PTR was measured during wear tests, were analyzed.

4.3 Results and discussion

4.3.1 Airborne particulate contaminants

The setup used in this study was located in the class 10,000 clean room. To measure airborne particulate contaminants in the room, we monitored particle count in the room for 70 hours with the laser particle counter. The particle count was sampled for 1 hour intervals. Data were obtained in two different size bins: 0.1-0.3 μm and $> 0.3 \mu\text{m}$. The measured count is shown in Fig. 4.4 (a). As observed from Fig 4.4 (a), the particle count for both bins exhibits periodic variation with a period of approximately 24 hours, which most probably results from the operation of the environmental unit and its ability to clean the air in the room. The concentration of 0.1-0.3 μm size particles varies from 1 to 20 cm^{-3} , while that of greater than 0.3 μm remains less than 1 cm^{-3} . For reference, class 10,000 refers to an environment with particle concentration less than 3.53 cm^{-3} (10,000 ft^{-3}) particles with size not exceeding 0.5 μm .

In order to eliminate these airborne particulate contaminants (background particles) from the drive operating environment it was sealed and flushed with clean air filtered with a 0.2 μm pore size PTFE membrane filter. The particle count was measured close to the head mount as shown in Fig. 4.2. During this measurement the drive was not running and the vacuum pump was turned on to provide tension to the tape wound on the reels. For the first period shown in Fig 4.4 (b), the particle count was measured with no clean air supplied to the drive environment. The concentration of 0.1-0.3 μm size particles remained at about 5 cm^{-3} . Clean air was supplied into the drive environment at a flow rate of 0.036 m^3/s . Initially, no change was observed in the particle count for both size bins (Fig. 4.4 (b)). With an increasing time, the particle count for the 0.1-0.3 μm bin

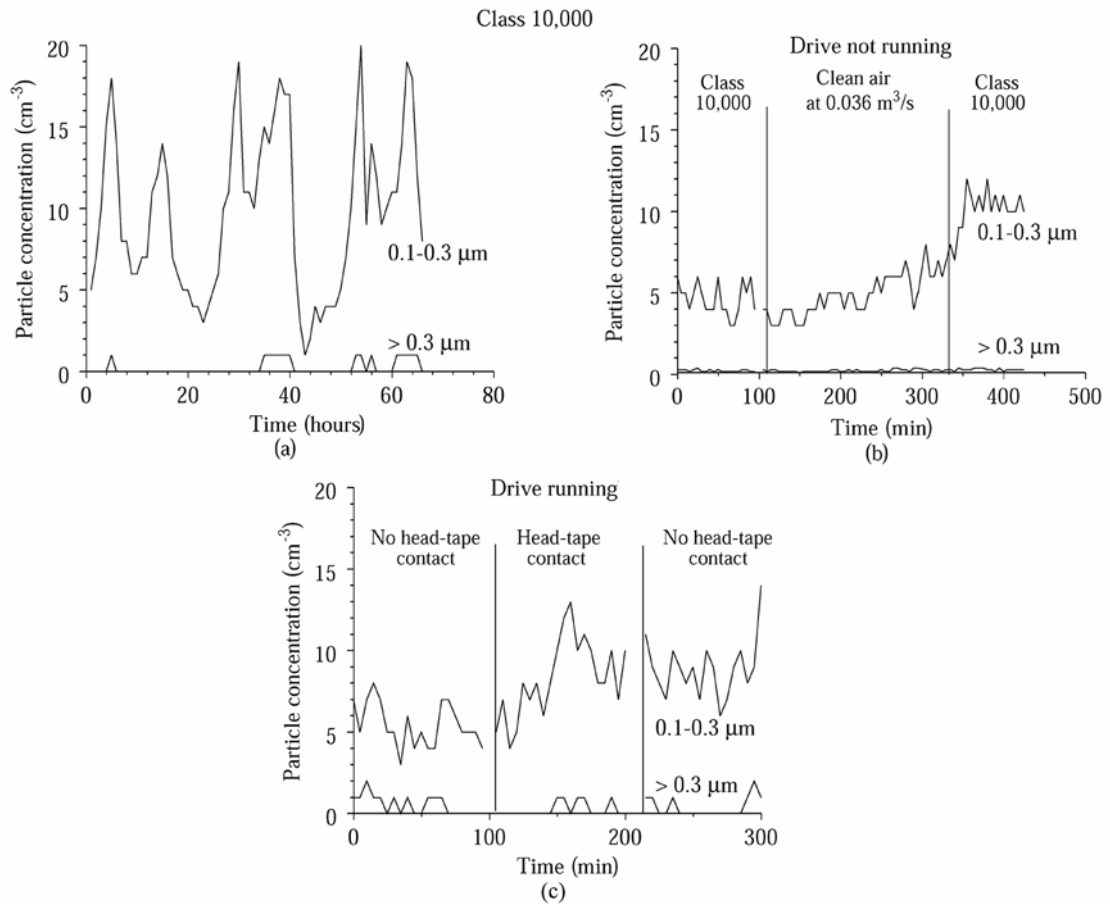


Figure 4.4: Number of airborne particle versus time: (a) in laboratory environment; (b) in laboratory environment and during flushing by clean air; (c) for a period before head-tape contact, followed by two hour long period of head-tape contacts, and followed by a period of no head-tape contact.

showed a slight increase. As observed from Fig. 4.4 (b), after the supply of clean air to the drive was cut off, the particle count for the 0.1-0.3 μm size particles leveled off and took the value higher as compared to the beginning of the test. No variations in the particle count for the particle greater than 0.3 μm was observed during the test. It should be noted that the particle count during this experiment follows the variation in the background particles count (Fig. 4.4 (a)), which means that the clean air flows used are not enough to eliminate the background. The fact that the drive is not well sealed and that the air pump generates an extra flow into the drive accounts for the failure to eliminate the background.

So far we have considered airborne contaminant particles present in the drive operating environment. During the wear tests, loose particles are generated at the head-tape interface. In order to check whether some of the debris particles became airborne, a test was performed. The drive was running during this test. The number of airborne particles per cubic centimeter was measured in the vicinity of the tape head. Data were taken for a period before head-tape contact, followed by two hour long period of head-tape contact, and followed lastly by a period of no head-tape contact (Fig. 4.4 (c)). The variability of the data does not allow us to separate the airborne particle, if any present, from the background.

During these experiments it was established that the background count of the airborne particulate contaminants of the size greater than 0.1 μm was in the range of 5-20 cm^{-3} . Flushing the drive with clean air or head-tape contact does not alter the background. Therefore, the average background count of 10 cm^{-3} was taken into account when setting the concentration of the particles injected during the wear experiments. We also believe

that these particles do not alter the results as most of these particles are "soft" dust particles from the environment.

4.3.2 Effect of particulate contamination on PTR

Fig. 4.5 (a) shows PTR vs. sliding distance for the wear tests performed in the operating environment contaminated with particles of different concentration, size, and material nature. The 2-dimensional AFM scans across the thin-film region are presented for the test performed in class 10,000 laboratory environment to show the history of the PTR growth with sliding. During the test performed in the class 10,000 laboratory environment, PTR grows quickly during the first 20 km of sliding. With increasing sliding distance, the rate of PTR growth decreases and the increase in the recession during the last 400 km of sliding is only 6 nm. PTR has reached close to saturation. The presence of contaminant particles in the drive environment alters the described behavior. It should be noted, that the initial PTR in the heads used in this study was in the range from 8 to 15 nm caused by the lapping in the manufacturing process. It was shown both experimentally [Tsuchiya and Bhushan, 1995] and theoretically [Scott and Bhushan, 2002] that the recession at saturation for the heads with different initial PTR approaches the same value. The results obtained in the present study are different. This means that the difference in PTR observed, and shown in Fig. 4.5 (a), for the wear tests with different particles injected into the drive environment is caused by the particles entrapped at the head-tape interface from the environment. It is also observed from Fig. 4.5 (a) and 4.5 (b), that particle concentration, size and hardness affect PTR. These effects are summarized in the following three subsections. For each comparison, only the parameter being studied is varied.

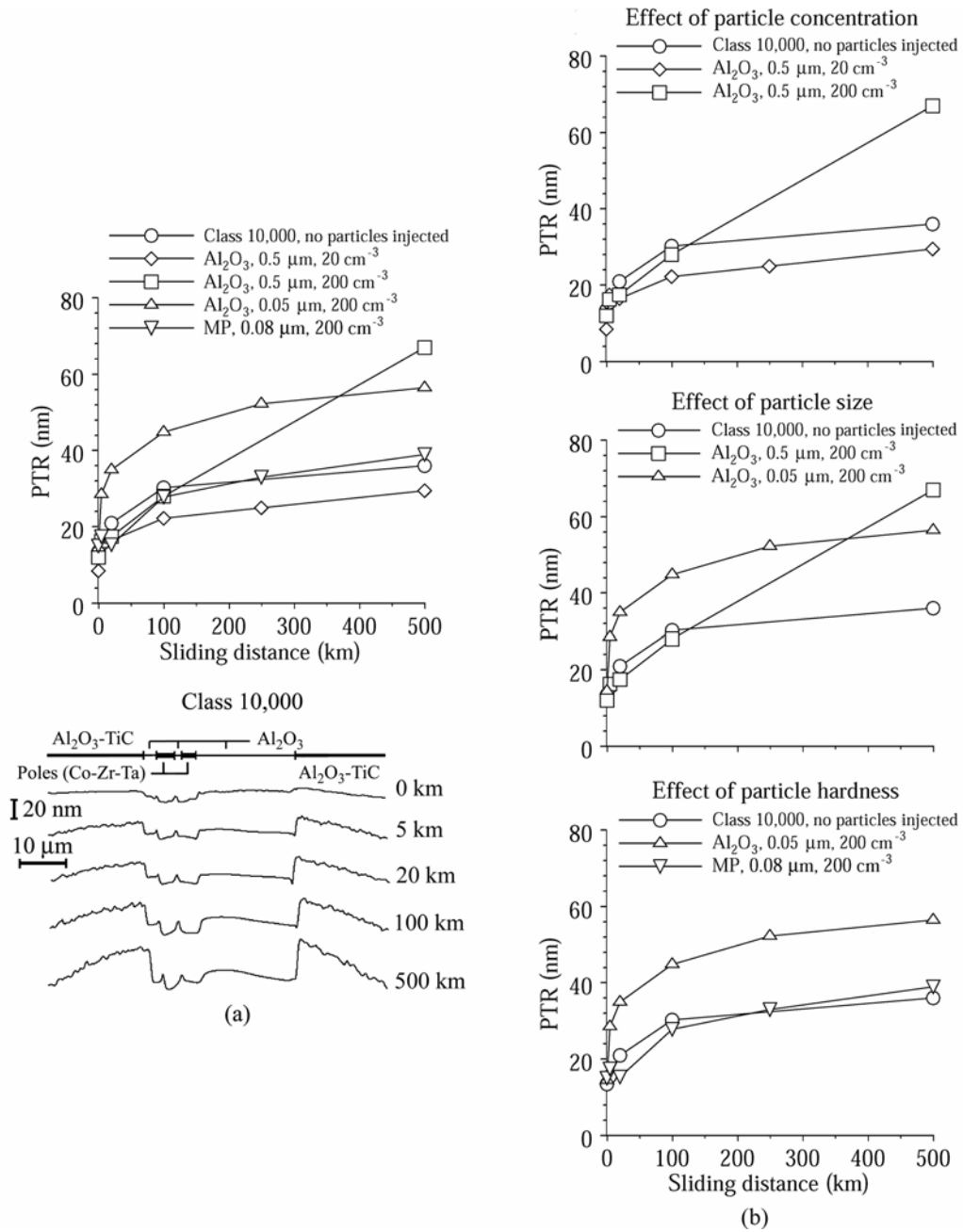


Figure 4.5: PTR vs. sliding distance. (a) Summary of the wear tests performed and 2-dimensional AFM scans across the thin-film region for the test performed in class 10,000 laboratory environment; (b) effect of contaminant particle concentration, size, and hardness on PTR.

4.3.2.1 Effect of particle concentration

The effect of concentration of particulate contaminants on PTR was studied by injecting alumina particles (nominal size of 0.5 μm) into the drive environment during the wear test at two levels: 20 cm^{-3} and 200 cm^{-3} (Fig. 5 (b, top)). Data for the wear test performed in class 10,000 environment with no particles injected serve as a baseline. It is observed from Fig. 4.5 (b) that an increase in the contamination level of the drive environment by a small amount (20 cm^{-3}) of large particles decreases PTR at saturation and saturation in PTR occurs sooner as compared to the test run in the class 10,000 environment. At high level of contamination (200 cm^{-3}), the rate of PTR growth remains constant and no saturation in recession occurs for the sliding distance run. PTR at the end of testing at a high level of contamination was measured to be 57 nm as compared to 36 nm for the baseline test.

The thin-film region of the tape heads run in the wear tests with different contaminant particles present in the drive environment was analyzed using SEM (Fig. 4.6) and AFM (Fig. 4.7). The data were taken after testing was completed. The images of the unworn head are presented for reference. The same pole pair is presented on both figures for each head. As observed from Fig. 4.6, the only head that shows contrast in SEM images within a single material is the head worn in the class 10,000 environment; several dark spots are present on the alumina overcoat (Fig. 4.6 (a)) and scratches in the direction of tape motion are seen for the CZT pole pair (Fig. 4.6 (b)). Both surface topography and chemical composition of the surface layers contribute to the contrast formation in the SEM image. In order to correctly interpret the result additional information is required. AFM images (as measured in the present study) provide only

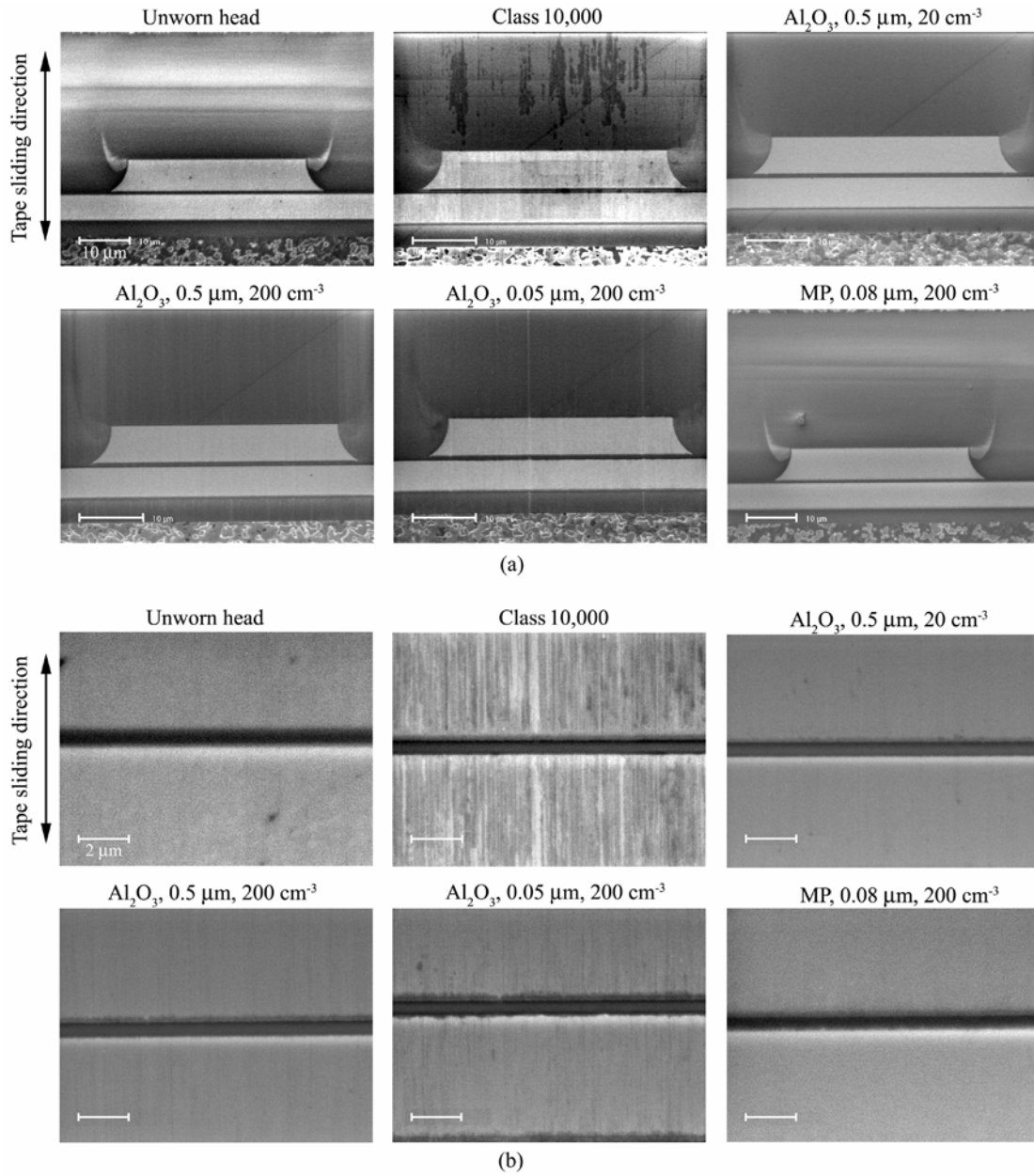


Figure 4.6: Secondary electron SEM images of the tape heads run in the wear tests with different contaminant particles: (a) thin-film region; (b) pole pair at high magnification.

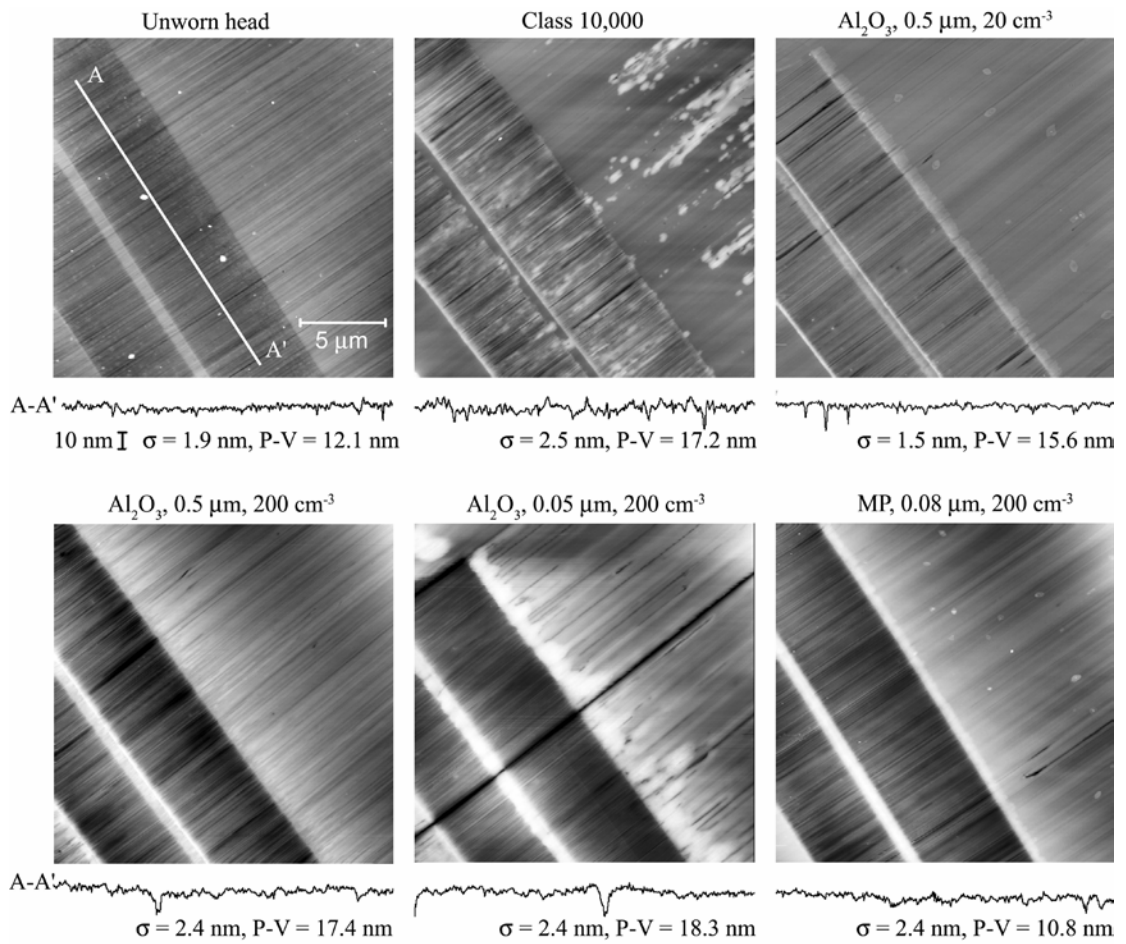


Figure 4.7: AFM images of the tape heads run in the wear tests with different contaminant particles and 2-dimensional AFM scans along the pole. The transition from black to white in the gray scale image covers height range of 100 nm. Brighter areas correspond to higher points.

surface height information. It should be noted that dark areas (variation in surface topography and/or chemical composition) over the overcoat on the SEM image of the head worn in the class 10,000 environment (Fig. 4.6 (a), Class 10,000) correspond to bright areas (higher points) in the same region in the AFM image (Fig. 4.7, Class 10,000). Based on this comparison of SEM and AFM data, we believe that some adherent debris resides on the surface of the thin-film region of the head worn for the class 10,000 environment. All other worn heads appear to be free of adherent debris. We believe that contaminant particles trapped at the head-tape interface provide cleaning action. Scratches in the direction of tape motion are observed over the thin-film region of the worn heads (Fig. 4.7), which implies that wear occurred by plastic deformation.

We also believe that the largest particles in the distribution lift the tape. If the total number of the particles at the interface is low (low concentration of the contaminants in the environment) the number of small particles that can abrade the thin film is small. This leads to a decrease in thin film wear and results in decreased recession. The increase in particle concentration increases thin-film wear. As the size of the particles is large as compared to the recession, no saturation occurs.

4.3.2.2 Effect of particle size

Fig. 4.5 (b, center) shows the effect of particle size on PTR. Wear tests were performed with alumina particles of 0.05 μm and 0.5 μm size injected into the drive environment at a concentration 200 cm^{-3} . The highest rate of PTR growth was observed for the test with small particles present in the drive environment (Fig. 4.5 (b, center)) during the first 20 km of sliding. With increasing sliding distance the rate of PTR growth decreased during the tests performed in the class 10,000 environment and with small

particles injected. The saturated recession was higher in the head run in the environment contaminated with small particles as compared to the baseline. The rate of PTR growth remained constant during the test with large particles present in the environment and no saturation in PTR was achieved for the sliding distance run. We believe that the presence of the small particles does not alter the head-tape separation and most of the particles abrade the surface. High concentration of the particles leads to high thin-film wear at the beginning of sliding. As recession grows with sliding, the number of particles abrading the surface decreases, when the particles are small, resulting in recession saturation. The size of the 0.5 μm alumina particles is large as compared to the recession, the number of particles abrading the surface does not change with an increasing sliding distance and no saturation occurs.

The depth of scratches over the thin-film region of the worn heads (Fig. 4.7) can be used as a measure of the wear severity. The depth can be estimated from the roughness parameters of the 2-dimensional profiles along the poles as shown in Fig. 4.7. The highest values of the P-V parameter for the 2-dimensional profiles were measured for the heads worn in the environment contaminated with alumina particles of nominal size = 0.5 μm and 0.05 μm and concentration = 200 cm^{-3} . This is in an agreement with the high PTR values measured for the same heads in wear tests at the end of testing.

4.3.2.3 Effect of particle hardness

The effect of contaminant particle hardness on PTR was studied by injecting alumina (nominal size 0.05 μm) and MP (length 0.08 μm , aspect ratio 6:1) particles into the drive operating environment during a wear test (Fig. 4.5 (b, bottom)). As observed from Table 4.1, the hardness of alumina particles is almost nine times that of MP. As

shown on the bottom plot of Fig. 4.5 (b), the presence of “soft” (MP) contaminant particles in the environment does not affect PTR growth as compared to the baseline test. The hardness of MP (Table 4.1) is lower than that of the materials constituting thin-film region (H_f in Table 4.2, to be presented later) and these particles cause no or little damage to the head surface. “Hard” (alumina) contaminant particles increase the rate of PTR growth at the beginning of sliding drastically. With increasing sliding distance, PTR levels off. The saturated recession was high in the test run in the environment contaminated with “hard” particles.

4.3.3 Comparison with analytical model

Based on the results of the wear tests performed at different levels of contaminations with contaminant particles of different concentration, size, and material nature and the analysis of the worn head surfaces, some conclusions can be summarized as follows. Airborne particulate contaminants can be entrapped at the head-tape interface and may affect PTR in a linear tape drive. PTR increases with an increase in one of the following: particle concentration, size, and hardness. These results also support the notion [Bhushan, 1996; Xu and Bhushan, 1998] that wear of the thin-film region occurred by plastic deformation and the wear mode for the head thin-film materials is three-body abrasive wear. In this section we will compare the experimental observations with the predictions of an analytical model for such wear behavior at the micro/nanoscale.

Scott and Bhushan [2002] have developed an analytical model for the micro/nanoscale differential wear of the multiphase materials responsible for PTR in thin-film magnetic heads. This can be used as a predictive tool for PTR change versus sliding distance. The wear mode for the head thin-film materials is assumed to be three-

body abrasive wear. The wear mode for the substrate material is assumed to be a combination of adhesive and two- and three-body abrasive wear [Bhushan, 1996]. Wear is also assumed to occur by plastic deformation. Plastic wear, whether adhesive or abrasive, is described by the empirical relation [Bhushan, 1999]

$$V = \frac{kWL}{H}, \quad (4.1)$$

where V is the wear volume, k the dimensionless wear coefficient, W the normal force, L the sliding distance, and H is the hardness of the worn surface. Additional assumptions and simplifications used in the model are summarized here: (1) wear for the individual head material is uniform, (2) air-film pressure is disregarded in the calculation of nominal contact pressure, (3) particle deformation is disregarded, (4) air-film thickness is independent of wear particle thickness and recession depth, (5) for a wear event, the contact between particle and tape, and between the particle and the head's thin film material is plastic, (6) the contact pressure on the substrate is equal to that on the thin film when the recession depth is zero, (7) the number of particles in contact with the film does not change with sliding distance and is equal to the maximum number required to support the contact pressure at a recession depth of zero, (8) direct contact between the tape and thin film is disregarded and (9) development of stain on the head is ignored. The required inputs for the model are H_{sub} , H_f , H_t , which are hardness of substrate, thin-film and tape, respectively; R_{fi} and R_{ti} , radius of contact between particle and thin film and between the particle and tape; h , thickness of air film between head and tape; T , tape tension; k_{sub} and k_f , dimensionless wear coefficient for substrate and thin film, w_{tape} , width of tape; R_{head} , radius of head contour; w_f , width of thin film; and t_i , thickness of particle.

By using the model, the change in the thin-film recession for the head slid against the tape can be calculated. We performed the calculation of PTR vs. sliding distance for the head used in the study ($\text{Al}_2\text{O}_3 - \text{TiC}$ substrate/ $5 \mu\text{m}$ CZT pole) using the parameters listed in Table 4.2. The effect of particle size (thickness) and thin-film wear coefficient on recession was studied. For each comparison, only the parameter being studied is varied. We did not perform simulations for the $0.5 \mu\text{m}$ nominal particle size, as we believe these particles lift the tape and alter the air-film thickness which contradicts one of assumptions postulated in the derivation of the model. The results are presented in Fig. 4.8. An increase in particle size leads to increase in recession (Fig. 4.8), which agrees well with experimental data (Fig. 4.5 (b, center)) at the end of sliding. However, the rate

Head	H_{sub} (GPa) ^{a)}	H_f (GPa) ^{a)}	H_t (GPa) ^{b)}	R_{fi} (nm) ^{c)}	R_{ti} (nm) ^{c)}	h (nm) ^{d)}	T (N)	k_{sub}	k_f
Al_2O_3 - TiC/ $5 \mu\text{m}$ CZT	30.2	8	0.3	100	100	40	2.2	0	3.5×10^{-8}

^{a)} Li and Bhushan, 2001.

^{b)} Li and Bhushan, 1997.

^{c)} Approximate radius of HCA [Scott and Bhushan, 2000].

^{d)} Scott et al., 2001

Table 4.2: Model parameters for derivation of curves in Fig. 4.8.

of PTR growth in the early period of sliding is clearly lower for the modeled curve for small particle size. This difference most probably results from decrease in wear coefficient k_f with sliding distance and recession growth. Due to the size distribution of the particles and with the recession growing, fewer particles of the same nominal size can interact with the thin film to cause wear. A decrease in the thin film wear coefficient k_f decreases the recession (Fig. 4.8). The lower value of k_f can result from the decrease in the number of abrasive particles at the head-tape interface, which is supported by the data presented in Fig. 4.5 (b, top). The decrease in the concentration of the contaminant particles lowers PTR.

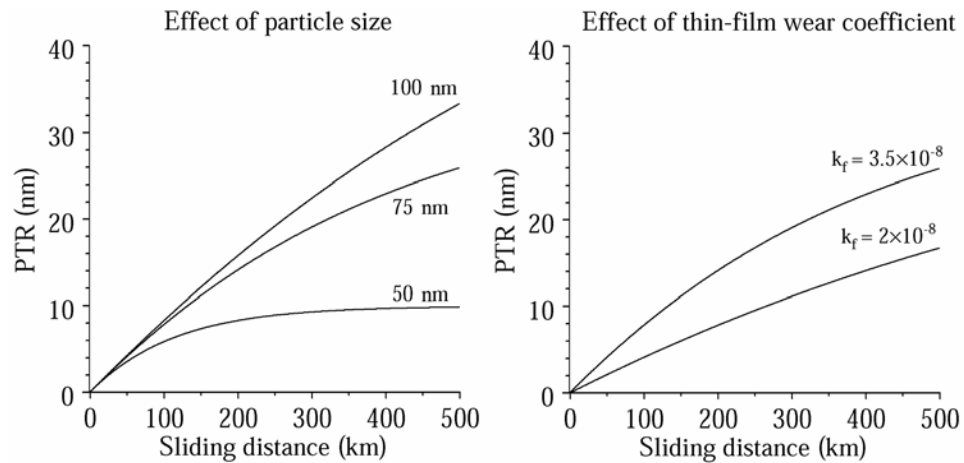


Figure 4.8: Results generated by the model showing the effect of particle size and thin-film wear coefficient. Model parameters are listed in Table 4.2.

4.3.4 Mechanism of PTR with contaminant particles from the environment

Based on the experimental observations and analytical modeling the effect of particulate contamination on PTR in linear tape heads can be summarized in the drawing shown in Fig. 4.9. It shows head-tape interface with large and small particles entrapped. We believe that the largest particles (there is a size distribution for each nominal particle size) of those with the large nominal size actually lift the tape during a test. If the number of the particles at the interface is low (low concentration of the contaminants in the environment) the number of particles that can abrade the thin film is small due to particle size distribution. Note that small particles do not interact with either tape or head. This leads to a decrease in the thin film wear coefficient and results in decreased recession (Fig. 4.5 (b, top), Al_2O_3 , $0.5 \mu\text{m}$, 20 cm^{-3}). The increase in particle concentration increases thin-film wear coefficient. Since the size of the particles is large as compared to

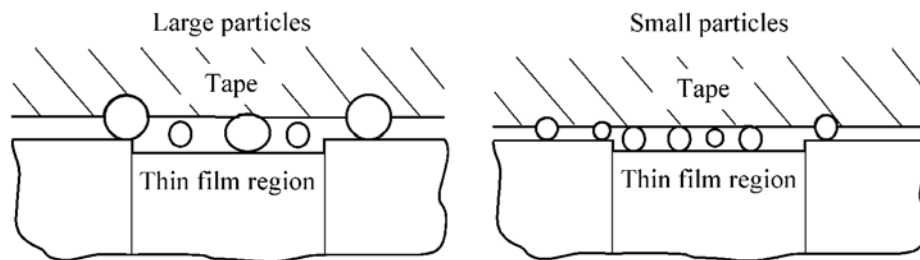


Figure 4.9: Schematic showing head-tape interface with large and small particles entrapped. Large particles lift the tape.

the recession, no saturation occurs (Fig. 4.5 (b, top), Al_2O_3 , $0.5 \mu\text{m}$, 200cm^{-3}). As depicted in Fig. 4.9, the presence of the small particles does not alter the head-tape separation and most of the particles abrade the surface. A high concentration of particles leads to high thin-film wear coefficient at the beginning of sliding. As recession grows with sliding, the number of particles abrading the surface decreases and recession saturates (Fig. 4.5 (b, center), Al_2O_3 , $0.05 \mu\text{m}$, 200cm^{-3}). The hardness of MP (Table 4.1) is lower than that of the materials constituting the thin-film region (Table 4.2), and the wear rate due to three-body abrasion is low. These particles do not contribute to the head wear.

4.4 Summary

The controlled injection of three-body particles into the head-tape interface has shown the importance of three-body abrasion in PTR growth.

Airborne contaminant particles present in the tape drive operating environment can be entrapped at the head-tape interface and may affect PTR.

PTR increases with increases in one of the following: particle concentration, size, and hardness. The experimental results agree well with the predictions of the analytical model for the micro/nano-scale differential wear.

The presence of a small amount of large particles at the head-tape interface can decrease PTR. High concentration of the large particles leads to continuous PTR growth.

Small particles drastically accelerate PTR growth at the beginning of sliding and increase the recession at saturation.

The results of this study support the notion that three-body abrasion is the cause of PTR in tape heads.

CHAPTER 5

MEASUREMENT AND ORIGIN OF TAPE EDGE DAMAGE

IN A LINEAR TAPE DRIVE

5.1 Introduction

To increase storage capacity, future high performance linear tape systems will require the use of thinner magnetic tapes, lower track width, higher tape speeds, and lower head-tape spacing. Better tape guiding and tape dimensional stability is needed for better tracking performance as track widths are reduced [Bhushan, 2000]. Lateral (cross-track) motion of the tape can cause the desired data track to move away from the magnetic head and cause a so-called track misregistration (TMR) error. Consequently, tape lateral motion needs to be minimized. Higher track density necessitates the use of narrower data tracks that will be placed closer to the tape edge; tape edge damage becomes a concern. Tape guiding and consequent tape edge damage are dependent on various parameters, such as quality of virgin tape edge, drive operating parameters (e. g., tape tension and tape speed), type of the guides (e. g., stationary, rotary, and active), mechanical properties of the tape, and tape geometry (e. g., cupping and curvature). During drive operation, damage to the tape edge may result in tape dimensional changes,

leading to problems in tracking, generation of loose tape debris, which may show up at the head-tape interface and cause signal loss.

Topoleski and Bhushan [2000] were the first to evaluate the quality of factory-slit magnetic tape edges. They explored and explained the condition of a sample batch of factory slit tape edges. In general, it was found that edges of factory-slit particulate tapes had tears and missing chunks, and metal-evaporated tapes showed continuous jagged cracking. Bhushan and Mokashi [2001] found that progressive degradation of tape edges with increasing number of cycles is a primary contributor to continuous generation of loose debris and more debris collected on the head in the vicinity of the tape edges under normal drive operation. According to Hunter and Bhushan [2001], much more debris accumulates near the tape edge-head contact than at other contact locations. They reported an existence of a bias in debris distribution over the tape width toward one particular edge of the tape. Tape cupping and curvature, both naturally occurring, as well as virgin (factory-slit) tape edge quality were considered among other possible reasons for the bias existence. Scott and Bhushan [2003] reported that there is no difference in debris generation for tapes with different residual cupping.

It was established [Bhushan and Mokashi, 2001; Hunter and Bhushan, 2001; Topoleski and Bhushan, 2000] that factory slit tape edge is imperfect and degradation of tape edges during normal drive operation was a primarily source of loose debris generation. The existence of the bias in the debris distribution towards one of the two edges of the tape suggests that the quality of the two tape edges may be different. It should be noted that until now only the one edge from the magnetic coating side has been studied and the two tape edges have not been distinguished.

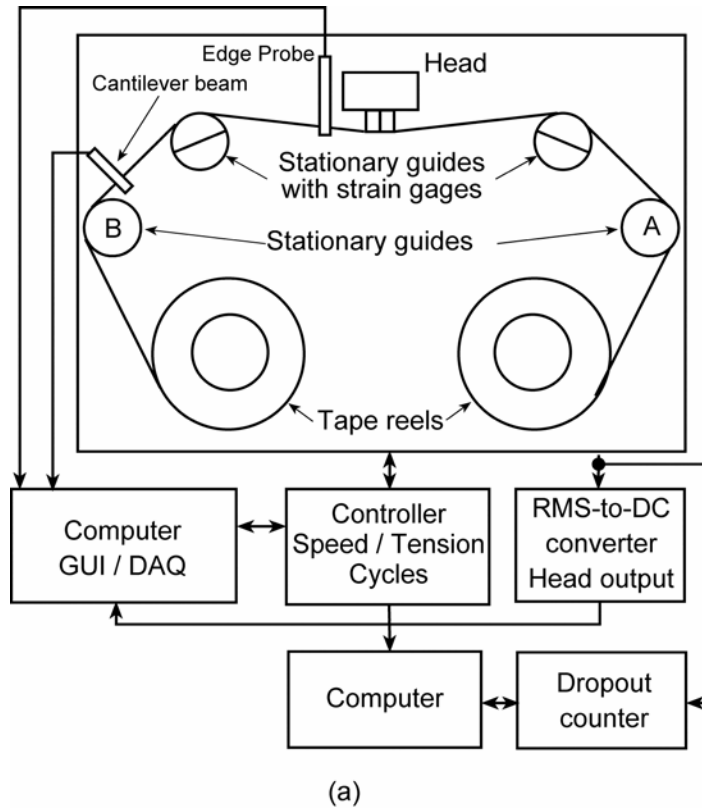
The objective of the present study is to develop a methodology to evaluate the quality of both tape edges and to study the origin of the tape edge damage. Wear tests up to 5000 cycles are conducted and head output, number of dropouts per minute, coefficient of friction and lateral tape motion are monitored. Based on the analysis of tape reels during the tests, possible mechanisms revealing the origin of the tape edge damage during slitting and under drive operation are proposed.

5.2 Experimental details

5.2.1 Description of tape transport and test procedure

Advanced Research Corporation (ARC) model 20 linear tape transport with a horizontal tape path was used, Fig. 5.1 (a). Drive tests were conducted in a class 10,000 laboratory environment (22 ± 1 °C; relative humidity 45 ± 5 percent). The tape reels are driven by Maxon D.C. motors outfitted with rotary encoders. They operate in forward (clockwise) and reverse (counter-clockwise) direction. The encoders are sampled every millisecond to calculate the motor angular speed during the cycle. All tape guides are stationary with the primary guide support posts equipped with strain gages. Tape tension is calculated by the measured deflection of the primary guides and the known wrap angles around the guides. During a tape pass, both reels must rotate in the same direction with the takeup reel speed slightly faster than that of the drive reel in order to maintain tension. The angular speeds are monitored by a tension feedback. Upon completion of the forward pass, the reels are decelerated to a stop, and then the motors reverse direction to begin the reverse pass. Tape is loaded onto a reel until the diameter of the roll is 60 mm. This is the tape length used to control tape speed in the transport. The pass length was set

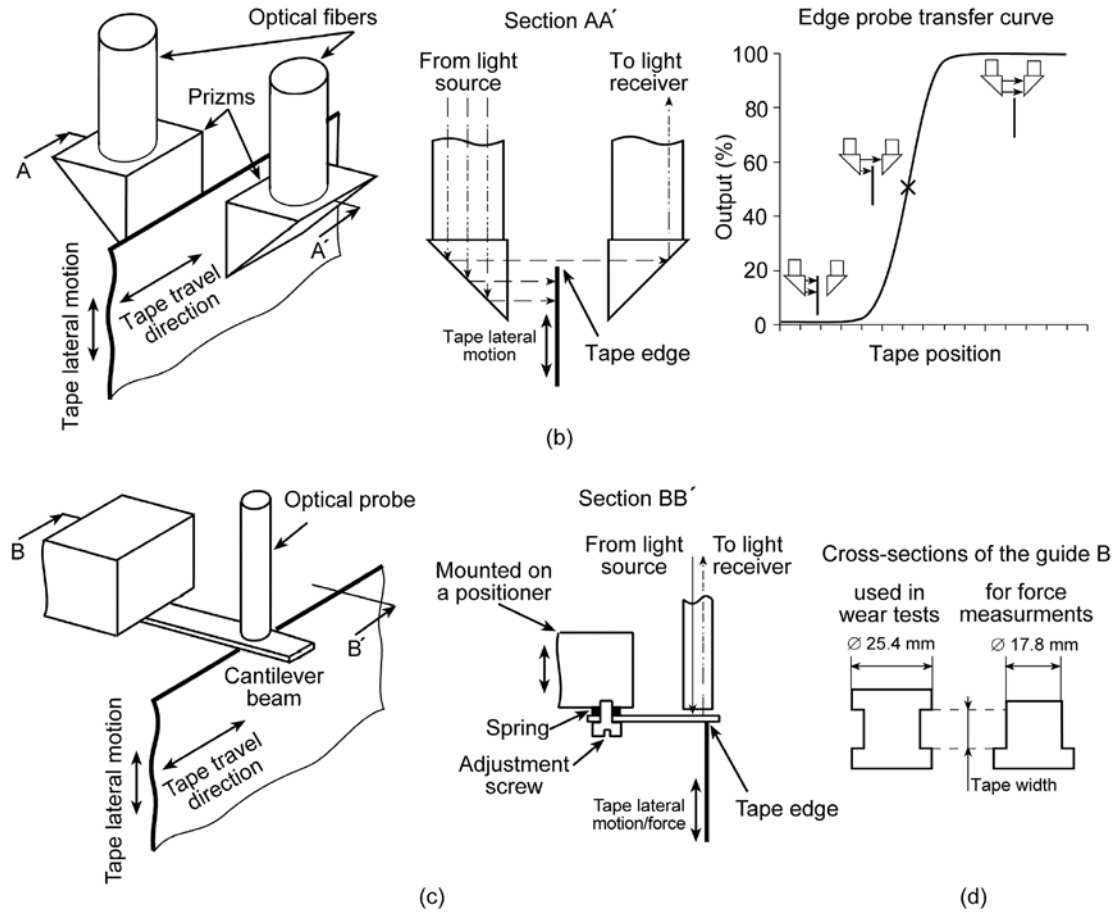
at 100 m for all the tests; with one forward and reverse pass equal to one 200 m cycle.
 The nominal tension and speed are 1 N and 4 m/s, respectively.



Continued

Figure 5.1: (a) Schematic of the tape transport, (b) Schematic showing details of the tape lateral motion measurement technique, (c) Schematic showing details of the lateral force measurement technique, and (d) Cross-sections of the guide used in wear tests and for force measurements.

Figure 5.1 continued



Tape lateral motion was measured by MTI 2000 Fotonic sensor equipped with Edge Probe (MTI Instruments Inc., Latham, NY, probe 2062E with sensitivity of 0.92 $\mu\text{in}/\text{mV}$ ($25 \mu\text{m}/\text{V}$) and noise level of 20 $\text{mV}_{\text{p-p}}$). The location of the edge probe with respect to the tape path in the transport is shown in Fig. 5.1 (a). Figure 5.1 (b) shows the

details of the tape lateral motion measurement technique. The edge probe is positioned over the tape edge. The light from the light source (Fig. 5.1 (a), Section AA') is reflected by a 90-degree prism to another 90-degree prism and finally reaches photodiode (light receiver). The Fotonic sensor converts the photodiode signal that is proportional to the light intensity into the output units (volts or microinches). If the light path is not obstructed by the tape edge the output of the Fotonic sensor is 100 percent (Fig. 5.1 (b), edge probe transfer curve). The output decreases as the tape moves upward into the gap between the prisms and vanishes to zero when no light reaches the photodiode. The transfer curve has a linear region in the center of which the reference point is selected corresponding to “zero” lateral displacement. Tape lateral motion is measured with respect to the zero point (cross on the transfer curve in Fig. 5.1 (b)).

Figure 5.1 (c) shows the details of the schematic of the lateral force measurement technique. Lateral force is the force exerted by the tape edge on the guide flange under drive operation. The force was measured by measuring the deflection of the cantilever beam (a hard drive slider suspension) and converting it into force units. The deflection was measured using proximity MTI 1000 Fotonic sensor (proximity probe MTI-3804 with sensitivity of $11.9 \mu\text{in/mV}$ ($302 \mu\text{m/V}$) and noise level of $25 \text{ mV}_{\text{p-p}}$). Calibration of lateral force was performed by using dead weights. Loads in the range of 0.1- 5 mN were applied to the beam at the point where it touched the tape edge and the displacement was measured by the Fotonic sensor. The linear relationship between the applied force and the Fotonic sensor output was measured to be 11.2 mN/V . The force was measured at the location shown in Fig. 5.1 (a) and a modified guide (guide B) with no upper flange was used.

At the beginning of each test a new piece of tape was loaded into the transport. A wavelength of 0.64 μm (sine wave at a frequency of 6.25 MHz) was recorded on the tape during the forward pass. Then, the drive was programmed to run the tape in the transport for 1000 and 5000 cycles. The reproduced signal from the head was amplified by the transport electronics and was transmitted to an RMS (RMS-to-DC) converter (AD637, Analog Devices, Norwood, MA; conversion time is 181 ms) and a Doradus 20 dropout tester (System 20 VTT multi-level dropout tester, Doradus Corp, Minneapolis, MN). The RMS head output, the tension signals obtained from the strain gages and the edge probe signal were captured by a data acquisition board (DAS-16G1, Omega Engineering Inc., Stamford, CT) with a sampling rate of 10 Hz. The data acquisition was controlled by Snap-Master V3.2 data acquisition software (HEM Data Corp., Southfield, MI). A BASIC program on another computer controlled the Doradus 20 dropout tester through an RS-232 port. The dropout count was triggered by a signal from the transport controller at the beginning of each forward and reverse pass. After the test was completed the worn part of the tape was removed from the transport and manually wound on a spare reel for further analysis.

The values of head output and coefficient of friction were averaged over each forward pass and these values were plotted on the graph. The tape lateral motion peak-to-peak amplitude was calculated as the difference between the highest and the lowest tape position with respect to the reference point during each forward and reverse pass. Head output data is presented in a voltage decibel format, and the reference 0 dB voltage is the initial RMS playback voltage averaged over the first 10 cycles. The tension signals obtained from the strain gages were used to calculate the coefficient of friction at the

head-tape interface by using belt equation [Bhushan and Mokashi, 2001]. The head wrap angle was 30 degrees.

Dropout is a short-term head signal loss. Debris particles passing through the tape-head interface can increase the head-tape spacing causing an instantaneous decrease in the signal amplitude and increase in friction force in a rotary head drive [Anderson and Bhushan, 1996]. Some dropouts do not correlate to friction force and are caused by tape defects [Anderson and Bhushan, 1996]. In the present study, the number of dropouts per minute was measured with the Doradus 20 dropout tester. The tester can measure twenty classes of dropouts defined by ranges of dropout depth and duration simultaneously. Dropout depth and duration are selectable in the ranges of 1 to 22 dB in 0.5 dB increments and 0.5 to 300 μs in 0.5 μs increments, respectively. In this study, the various ranges of dropout depth and duration were defined: 4-6 dB, 6-9 dB, 9-12 dB, and >12 dB; 0.5-1 μs , 1-5 μs , 5-10 μs , 10-25 μs , and >25 μs . The number of dropouts was counted during each forward and reverse pass and after the test was completed this was converted into the number of dropouts per minute which was plotted on the graph for the forward passes only.

5.2.2 Measurement techniques

The edges of the unworn (factory-slit) and worn for 1000 cycles and 5000 cycles tapes were analyzed using optical microscopy, AFM (Dimension 3100, Digital Instruments, Santa Barbara, CA) and SEM (Philips XL30 ESEM). Fig 5.2 (a) shows definition of the views examined in the study. The notations “upper edge” and “lower edge” are assigned arbitrarily and are used to distinguish between the two edges. Each edge was imaged from three angles - magnetic coating side, backcoat side and cross-

section view - as indicated for the upper edge in Fig. 5.2 (a), which resulted in a set of 6 images for each tape sample.

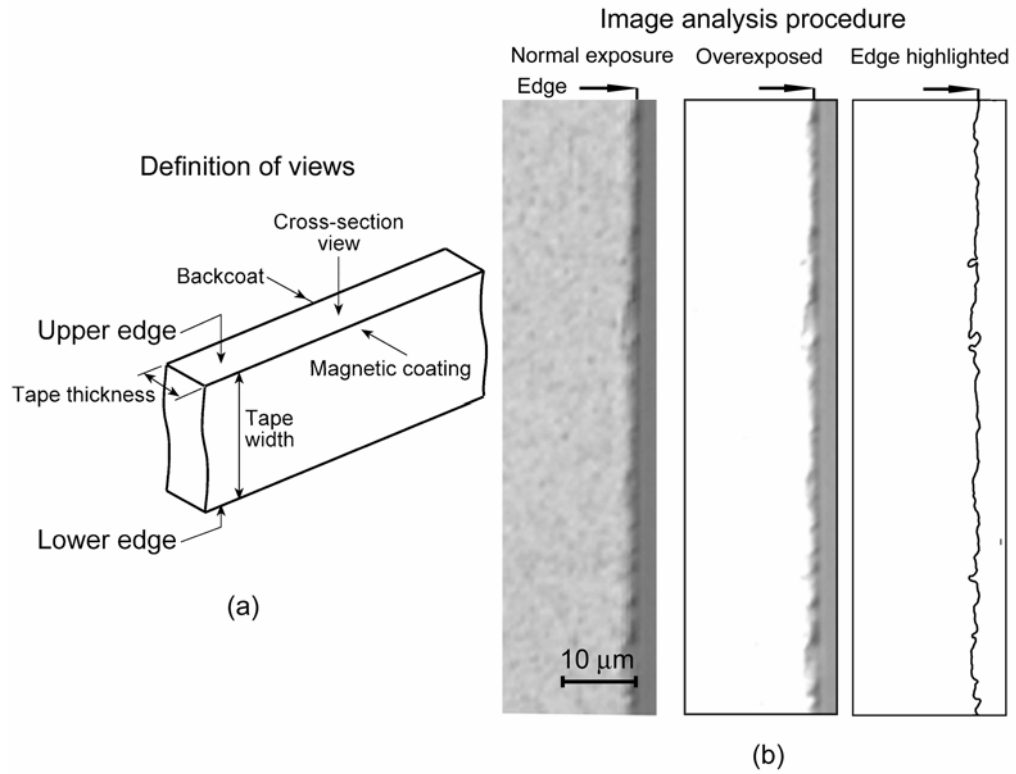


Figure 5.2: Definition of tape edge views used for imaging. (b) Sample optical micrographs illustrating edge quality measurement technique.

Optical images of the tape edges were obtained with an optical microscope (OPTIPHOT-2, Nikon Corporation, Tokyo, Japan) in the brightfield mode with a white light source. The gray-scale images (640×480 pixels) were captured with a CCD camera at a resolution of $0.175 \mu\text{m}$ per pixel. AFM images were taken in contact mode with a Si_3N_4 tip (square pyramid with a half-angle of 35 degrees) that has a nominal tip radius of 30-50 nm. SEM images were taken at an acceleration voltage of 5 kV. Secondary electrons were collected for imaging and none of the samples used for SEM analysis was coated.

For optical and AFM analysis of magnetic coating and backcoat, tape samples cut into 3 mm strips were mounded on a glass microscope slide by using double-sided adhesive tape. Tape edges were placed approximately 0.3 mm from the adhesive edge of the mounting. Flatness of the tape samples was a concern, and usually 80 to 90 percent of the mounted strips on a slide could be used for imaging. To measure tape cross-section with the AFM, a 5 cm long piece of tape was pinched between two glass microscope slides with the edge sticking out by about 0.3-0.5 mm over the slides and placed into the AFM. For SEM analysis, tape strips were mounted on sample holder using conducting adhesive.

Edge quality measurements were performed using methodology developed by Topoleski and Bhushan [2000]. The images of both magnetic coating and backcoat from both tape edges were analyzed. Tape edges were measured for their variability from a theoretically perfect straight line, which represents a perfect edge-slitting process during manufacturing. Figure 5.2 (b) shows image analysis procedure [Hunter and Bhushan, 2001; Topoleski and Bhushan, 2000]. The tape edge appears in the optical micrograph as a line of pixels of varying opacity. Adding power to the light source of the microscope

overexposes the image, leaving behind the tape edge. With the use of image analysis software, the edge is highlighted and the number of pixels constituting the edge is calculated. The total number of pixels for each edge becomes a measure of the deviation of the tape edge from a perfect straight line. Each number of pixels reported is based on ten measurements.

To assure the certainty and reproducibility of the edge quality measurements, we compared samples from two different reels as obtained from the manufacturer. Optical images of the magnetic coating at the upper edge were taken and visually inspected. No difference in the images was found for the two reels. After this inspection one reel was marked and the tape from this reel was used for the wear tests. Wear test for 1000 cycles was performed twice and optical imaging of upper and lower edges from the side of magnetic coating and backcoat was performed for both tape samples. Visual analysis of the optical micrographs revealed reproducibility of the changes occurring during sliding. Thus, three tape samples were selected (unworn, worn for 1000 cycles and 5000 cycles) for complete analysis and edge quality measurements, the results of which are reported in the study.

5.2.3 Head and tape specimens

Specimens of a commercial two module read/write head were used in the study. The schematic of the head along with the thin-film structure are shown in Fig. 5.3 (a). The two read/write modules are embedded in an aluminum housing. The thin-film region containing the magnetoresistive (MR) read and inductive write elements is located on the Al_2O_3 -TiC bumps. The length of the head is 16.5 mm and the width is 2.5 mm.

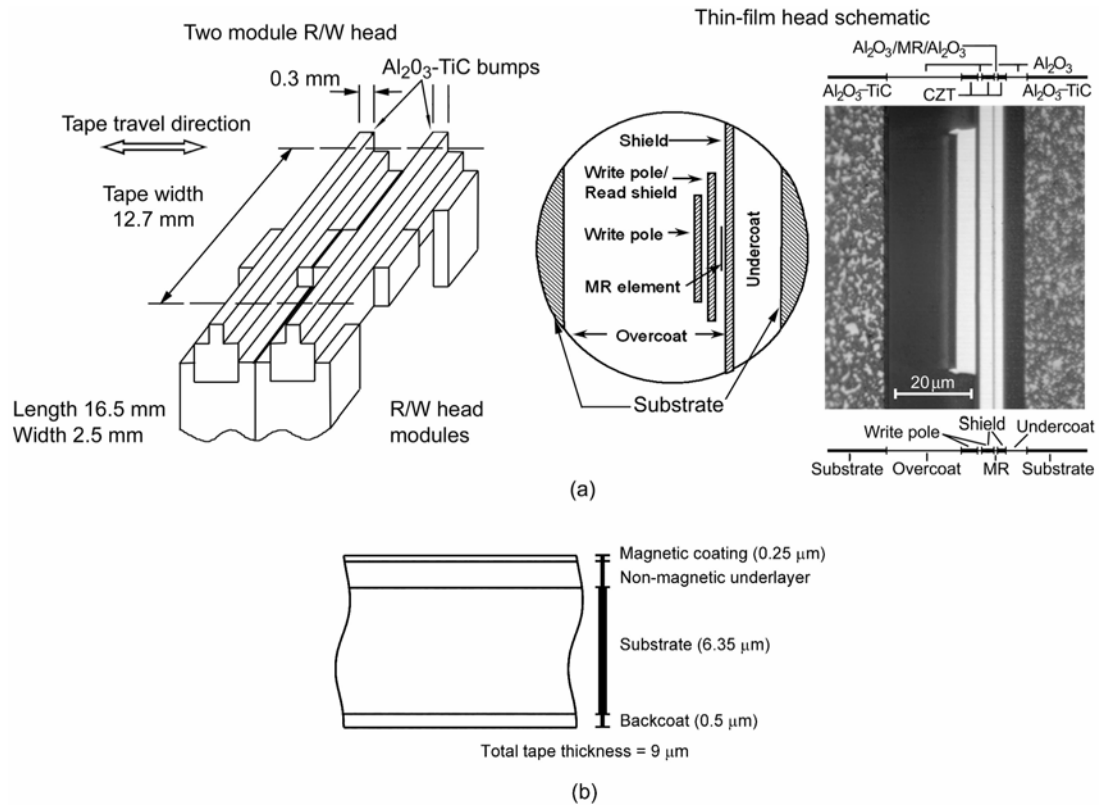


Figure 5.3: (a) General view and thin-film region of the tape head. (b) Schematic diagram of MP tape.

Commercial metal particle tape (12.7 mm) was used in the study. The tape is a dual-layer metal particle tape with a magnetic layer and backcoat thickness of 0.25 μm and 0.5 μm, respectively; a substrate thickness of about 6.35 μm and an overall thickness of 9 μm. Figure 5.3 (b) shows a schematic diagram of the tape.

5.3 Results and discussion

It has been established [Bhushan and Mokashi, 2001; Hunter and Bhushan, 2001; Topoleski and Bhushan, 2000] that tape edge damage occurs during factory slitting and normal drive operation. We performed long-term wear tests to study the effect of normal drive operation on edge quality, tape guiding and tape dimensional changes. The analysis of tape edge quality of factory-slit tape and tape used in tape drive was carried out. In order to understand sources of tape edge damage, we measured the lateral force exerted by the guide flange on the tape edge. Based on the analysis, origin of the tape edge damage is revealed and possible edge wear mechanisms are discussed. Finally, we propose a methodology for the tape edge degradation studies.

5.3.1 Wear tests

A number of wear tests were run continuously for 1000 cycles and 5000 cycles. Figure 5.4 shows representative data for the variation of head output, the number of dropouts per minute, coefficient of friction, and tape lateral motion peak-to-peak amplitude for the test run for 5000 cycles. It is observed from Fig. 5.4, that the head output steadily increases throughout the test. As the larger asperities on the tape surface wear down (tape burnishes), the spacing between the tape magnetic layer and the head decreases, which results in a stronger head output signal [Wallace, 1951; Bhushan, 1996, p. 11]. As the asperities wear, the rate of wear slows down and so decrease in the head-tape spacing, which is responsible for lower rate of signal growth [Patton and Bhushan, 1997a].

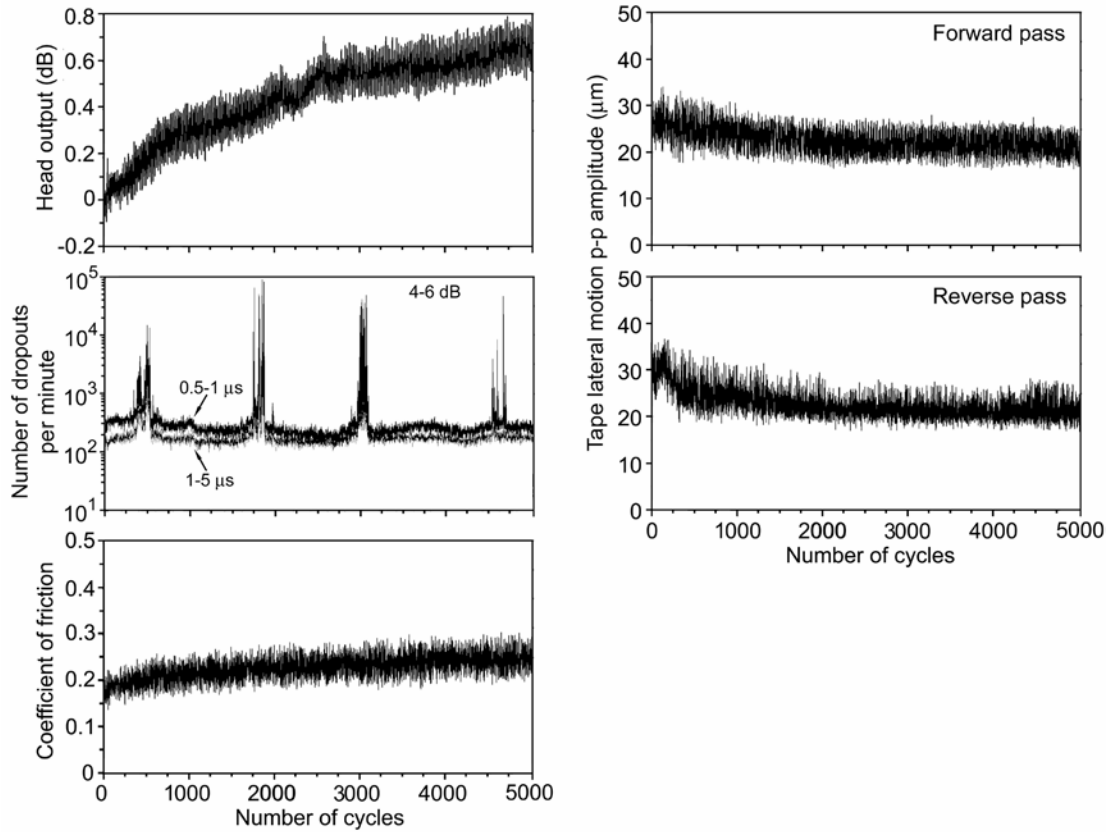


Figure 5.4: Variation of head output, number of dropouts per minute, coefficient of friction, and tape lateral motion peak-to-peak amplitude as a function of number of cycles.

The Doradus 20 dropout tester can measure twenty classes of dropouts (short-term head signal losses) defined by ranges of dropout depth and duration. In the present study the measurable dropout counts were obtained only in two classes with the depth of 4-6 dB and the duration of 0.5-1 μ s and 1-5 μ s. As observed from Fig. 5.4, the number of

dropouts per minute remains constant throughout the test except for short periods of time when a sporadic increase in the dropout rate occurs. Debris particles originating from the head and the tape and removal of stain, if any formed on the head surface, can be responsible for the observed behavior. Stain is a tenacious film formed on the head surface during normal drive operation. Stain readily forms at relative humidity less than 40-45% and consists of mainly inorganic material [Bhushan and Hahn, 1995; Scott and Bhushan, 2000]. Several authors reported that sporadic change in the dropout rate in the durability studies of the linear tape drives with belt-driven cartridges was observed [Kattner and Bushan, 2000a; Goldade and Bhushan, 2002]. Cycle of stain formation and removal has been found to be responsible for the observed variation in the number of dropouts per minute. Stain acts as a lubricant and when it gets removed both coefficient of friction and the number of dropouts per minute increases [Kattner and Bushan, 2000a; Goldade and Bhushan, 2002]. In the present study no such correlation is observed. In addition, head output steadily increases during the test, which suggests that no staining of the head occurs as stain would increase the head-tape spacing and decrease head output. Thus, debris particles from both tape and head can cause the increase in the number of dropout per minute. These particles can alter the friction force at the head-tape interface similar to that reported by Anderson and Bhushan [1996] for a rotary tape drive. However, in the present study coefficient of friction has been averaged over one pass which can mask short-term variations associated with the individual debris particles passing through the head-tape interface and causing dropouts.

Coefficient of friction increases from 0.17 at the beginning of sliding to 0.25 at 5000 cycles (Fig. 5.4). The rate of increase slows down with increasing sliding distance.

Burnishing of the tape asperities [Bhushan and Mokashi, 2001; Patton and Bhushan, 1997a] may result in an increase in the real area of contact responsible for an increase in friction [Bhushan, 1996, p. 239].

Figure 5.4 also shows variation of the lateral tape motion peak-to-peak amplitude with sliding. During the first few hundred cycles, the trends in the amplitude change differ for the forward and reverse passes. For the forward pass, the amplitude decreased from its maximum value of 27 μm peak-to-peak in the beginning of sliding and leveled off at 23 μm at 2000 cycles. For the reverse pass the amplitude increased from 30 μm during the first few cycles to 32 μm at 250 cycles. With further sliding it decreased and leveled off at 23 μm at 2000 cycles. For sliding in both directions the amplitude did not change significantly from 2000 cycles to the end of testing. At the beginning of sliding the tape lateral motion amplitude during the reverse pass is higher than that during the forward pass. These data show that at the beginning of sliding the tape lateral motion amplitude is affected by tape sliding direction, which is in agreement with the results reported in literature [Taylor et al., 2000], stating that the mechanical instabilities (tape vibrations) are responsible for the difference in tape lateral motion during forward and reverse passes.

In order to explain the trends in the peak-to-peak tape lateral motion amplitude as a function of number of cycles, the effect of tape use on dimensional changes (the change in the tape width) and tape geometry (the tape residual cupping) was measured for the unworn tape and tape worn for 5000 cycles. The tape width measurements were performed by using the technique developed by Ma et al. [2002]. Table 5.1 shows the results of the measurements performed at three locations for each tape. The

Location number	Unworn		5000 cycles	
	Tape width (mm)	Standard deviation (mm)	Tape width (mm)	Standard deviation (mm)
1	12.6494	0.0004	12.6480	0.0004
2	12.6490	0.0002	12.6480	0.0007
3	12.6491	0.0004	12.6484	0.0006

Table 5.1: Tape width measurement data for unworn and worn tapes. Each number represents an average of 300 measurements obtained over a 3 mm tape length. The width was measured at three different locations for both unworn tape and tape worn for 5000 cycles.

measurements were performed with a tension of 1 N (nominal tape tension in the transport) applied to the tape in a controlled environment (at 22 °C and 45 % RH) with a measurement accuracy of 2 μm and a precision of 0.1 μm . As observed from Table 5.1, the change in tape width was insignificant after the tape was run in the transport for 5000 cycles.

Magnetic tape is not a flat strip. A tendency of tape to curl about an axis perpendicular to the direction of travel along the tape width exists [Bhushan, 2000; Scott and Bhushan, 2003]. This tendency is called tape cupping. In negative cupping the edges of tape are farther from the head. Cupping measurements were performed using an optical microscope as described earlier. Figure 5.5 shows profiles along the width of the

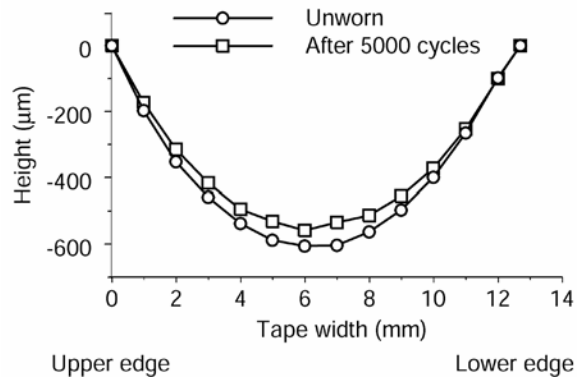


Figure 5.5: Cupping of the unworn tape and after use in tape drive. Magnetic coating is at the bottom (negative cupping).

tape for the unworn tape and tape worn for 5000 cycles. The decrease in residual cupping is less than 10 %.

Based on the tape width and tape cupping measurements, it appears that both changes are insignificant to be responsible for the decrease in the tape lateral motion amplitude with sliding. The tape edge quality is another factor affecting tape guiding, so it is evaluated next.

5.3.2 Analysis of tape edge degradation

The methodology described earlier was used to measure the quality of the tape edge of factory-slit and worn tapes. To date, edge quality was evaluated from the side of magnetic layer and only one of the two edges was considered. In the present study we

made an attempt to fully characterize both tape edges by imaging each one from three sides as shown in Fig. 5.2 (a).

Figure 5.6 shows typical optical images of magnetic coating and backcoat at tape edges. The quality of the magnetic coating at upper and lower edges of the unworn tape is different. Cracks and/or tears can be identified at the upper edge. The magnetic coating at the lower edge seems to have fewer cracks and tears. No significant difference can be found for the backcoat at both edges. The quality of the edges changed after tape was used in the transport for 1000 cycles. Most of the cracks disappeared from the magnetic coating at the upper edge. Few scratches close to the edges in the tape travel direction were observed. After 5000 cycles, chunks of magnetic coating got removed at the edges. The damage, which appeared at the backcoat as a result of tape sliding, can be easily identified by using an AFM, which provides information on surface heights. Figure 5.7 shows AFM images of the magnetic coating and the backcoat at the tape edges for the unworn tape and after use in tape drive. As observed from Fig. 5.7 (a), after sliding, a ridge was formed on the backcoat near the upper edge. The height of the ridge is about 1 μm and does not change much with sliding. However, ridge width increased with increasing sliding distance. It is also observed from Fig. 5.6 and Fig. 5.7 (a) (upper edge, 1000 cycles, and backcoat) that a part of the ridge is missing. This part was torn during sliding and contributed to the debris generated. By comparing optical micrographs and AFM maps of the backcoat at the lower edge, we identified the damage as isolated islands elevated over the backcoat surface, which resulted from smearing of the debris particles from the tape.

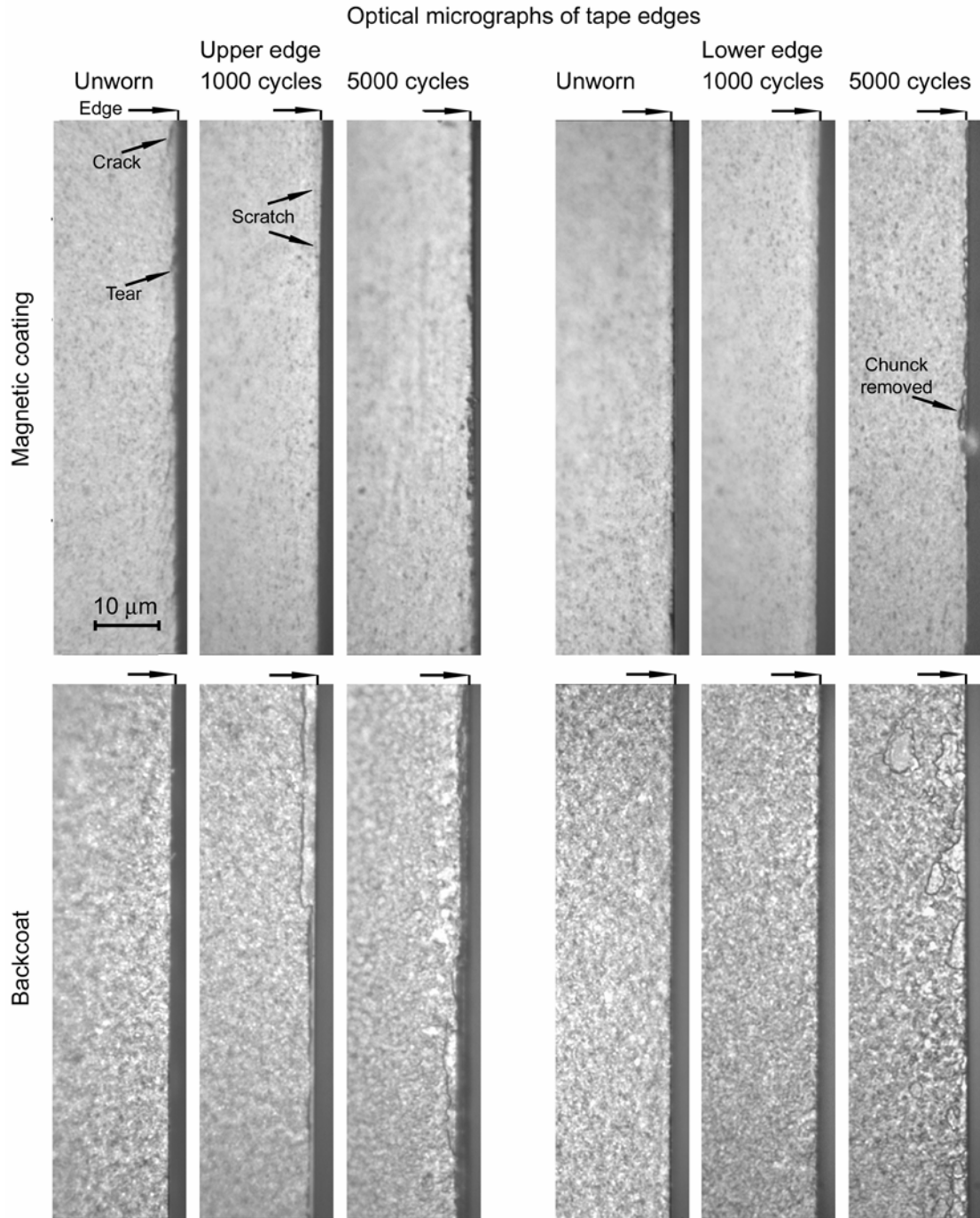
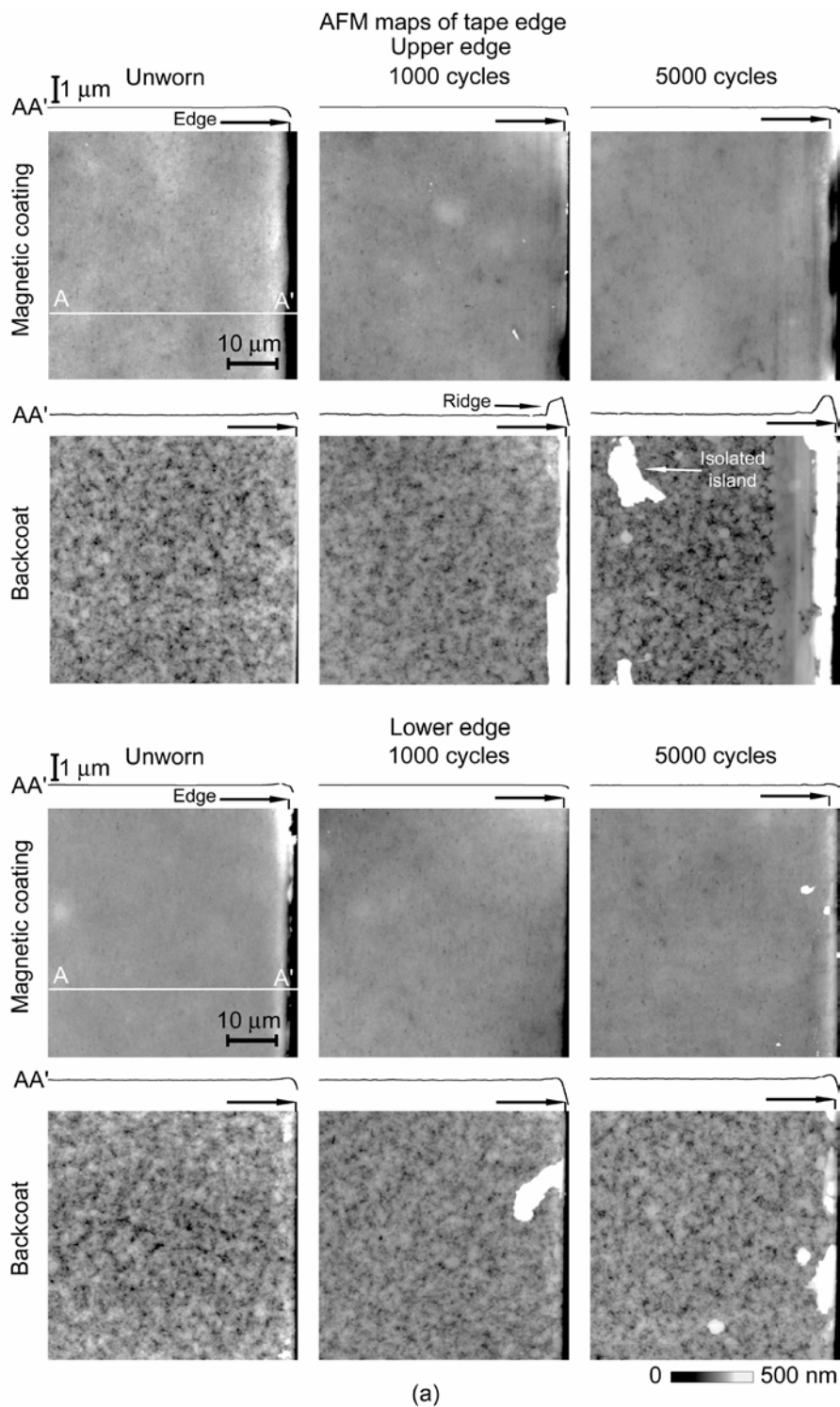


Figure 5.6: Optical analysis of degradation of tape edge under normal drive operation. Examples of cracks, tears and scratches are shown in the figure for clarity.

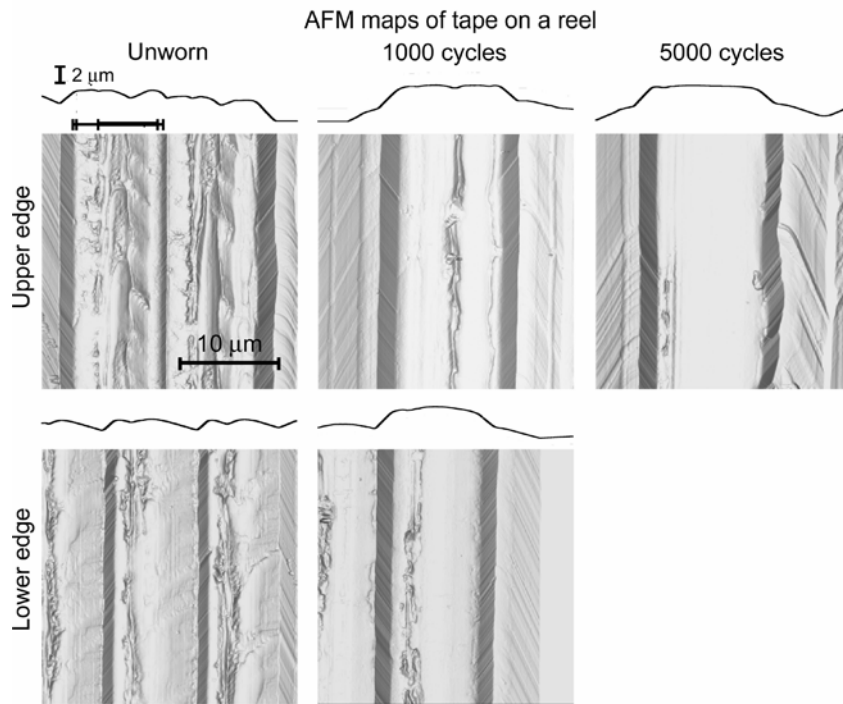
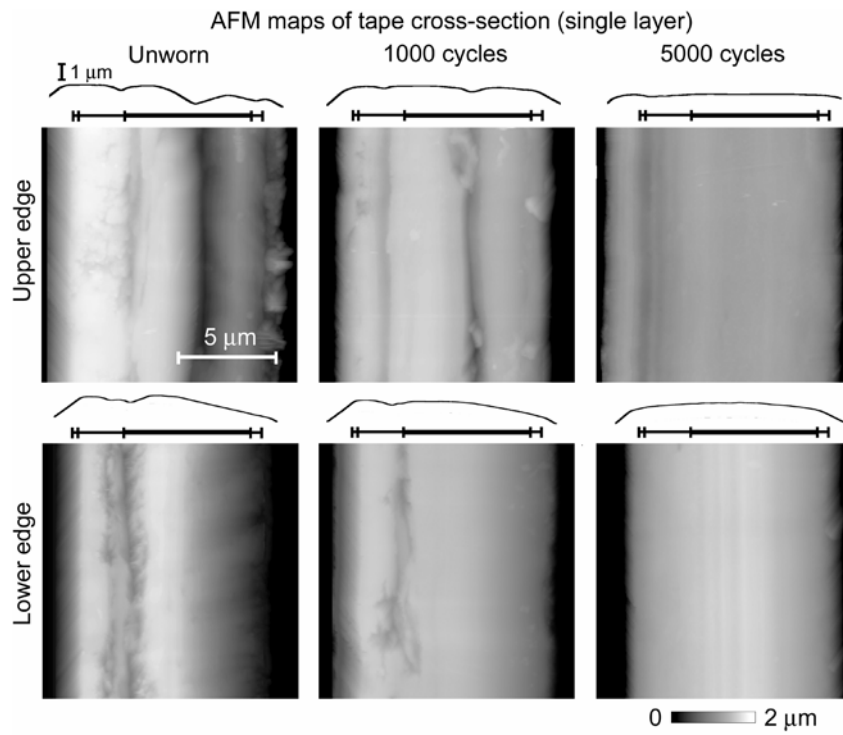
Figure 5.7: AFM analysis of degradation of the tape edge under normal drive operation. Surface profiles presented in (a) were measured along one scan line and in (b) were average over the entire scan. An example of the ridge and an isolated island are shown in the figure for clarity.



(a)

Continued

Figure 5.7 continued



(b)

The data presented so far characterize magnetic coating and backcoat at the tape edges. An AFM was also used to measure tape cross-section [Fig. 5.7 (b)]. Both tape single layer and tape stack wound on a reel were studied. In the AFM maps of a tape single layer brighter areas correspond to higher points. The AFM maps of tape stack on a reel were processed by using an option available in the AFM software, which eliminates abrupt changes in height (between adjacent tape layers) and allows highlighting small height features on the surface. Surface heights information should be read from the averaged profile presented for each image of the tape stack wound on a reel. As observed from Fig. 5.7 (b), the cross-section of both edges of the factory-slit (unworn) tape is not flat. After use in the tape drive the cross-section was smoothed and the tape thickness at the upper edge increased due to the formation of the ridge at the backcoat. It should be noted that the side of the pyramid of the AFM tip touches the surface if the surface slope is steep (high step, abrupt height change). In the present study this happens only when the tip slides off of the tape sample, which occurs at the corner formed by the cross-section and the magnetic coating and the cross-section and the backcoat over a distance of approximately 0.5 μm from the edge towards the center of the tape cross-section, which gives erroneous data on both sides over the tape width.

To overcome the limitations of optical microscopy (low depth of field), SEM of unworn tape and tape worn for 5000 cycles was performed. As observed from Fig. 5.8, SEM images provide higher resolution and better image quality, which is beneficial for quantification of the tape edge quality. Cracks developed during factory slitting can be clearly identified on magnetic coating at upper edge. SEM analysis confirms earlier results of optical microscopy and AFM as well as provides some additional information.

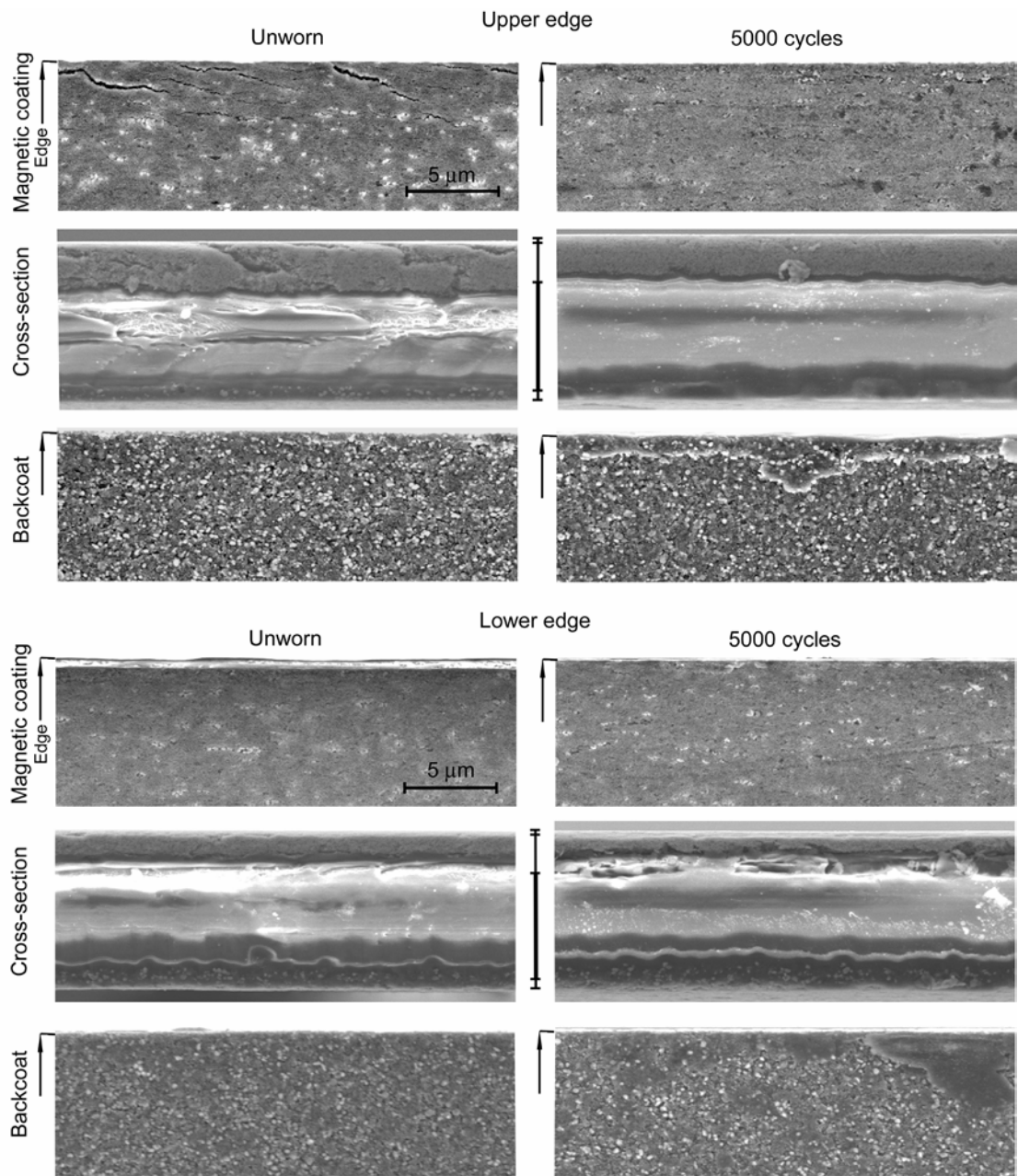


Figure 5.8: SEM analysis of degradation of tape edge under normal drive operation.

We see evidence of cracking of the magnetic coating, ridges and isolated islands in the backcoat. Additional information obtained here is tiny white spots observed in magnetic coating (Fig. 5.8, magnetic coating, all images), which are the particles of head cleaning agents (HCA), commonly made of hard ceramic materials with a size on the range of 150-300 nm [Bhushan, 2000]. The conductivity of these particles is low and they get charged when irradiated by the electron beam, which results in the appearance of a bright spot in an SEM image. It is observed from Fig. 5.8, that the number of HCA decreased for the upper edge of tape worn for 5000 cycles as compared to that of the unworn tape. The change in the number of HCA for the lower edge with sliding is insignificant which agrees well with the fact that the quality of the two edges of factory-slit tape is different. The lower edge experiences less damage (cracking and tearing) during manufacturing and thus has better wear resistance during normal drive operation.

Based on the qualitative characterization of the tape edge of factory-slit tape we conclude that two edges are imperfect and different. Tape edge damage occurs during factory slitting with cracking of the magnetic coating at one edge. After tape is used in a tape drive, chunks of magnetic coating are removed and ridge is formed over the backcoat at one edge, the cross-section of both tape edges gets smoothened. Smoother cross-section results in a better tape guiding and the decrease in the tape lateral motion amplitude, as observed in Fig. 5.4. The ridge can tear away and produce debris particles.

The quality of the magnetic coating and the backcoat at the tape edges was quantified next. Table 5.2 presents the number of pixels constituting edge damage as determined from optical micrographs of 112 μm along length (640 pixels) and 11.2 μm along width (64 pixels). The number of pixels is based on ten measurements. Based on

	Unworn	1000 cycles	5000 cycles
Upper edge			
Magnetic coating	680	690	870
Backcoat	660	7020	9620
Lower edge			
Magnetic coating	650	670	840
Backcoat	655	710	2650

Table 5.2 Number of pixels constituting edge damage. Optical micrographs of 112 μm along length (640 pixels) and 11.2 μm along width (64 pixels) were analyzed. Most of the damage occurs in the 0.5 μm (magnetic coating, lower edge) to 3-5 μm (backcoat, both edges) region from the edge. The number of pixels is based on ten measurements of each view.

the quantitative results, tape use in the drive caused most damage to the backcoat at the upper tape edge.

The damage to the tape edge results from its interaction with the guide flange. We measured the lateral force exerted by the flange on the tape edge during one cycle using the technique described earlier. The measurements were performed using a modified guide without upper flange. The location of the beam during the force measurements is shown in Fig. 5.1 (a). Figure 5.9 (a) shows variation of the lateral force during one cycle. A preload of 0.6 mN was required for the beam to stay in contact with the tape edge during forward and reverse passes. The magnitude of the lateral force is higher during a

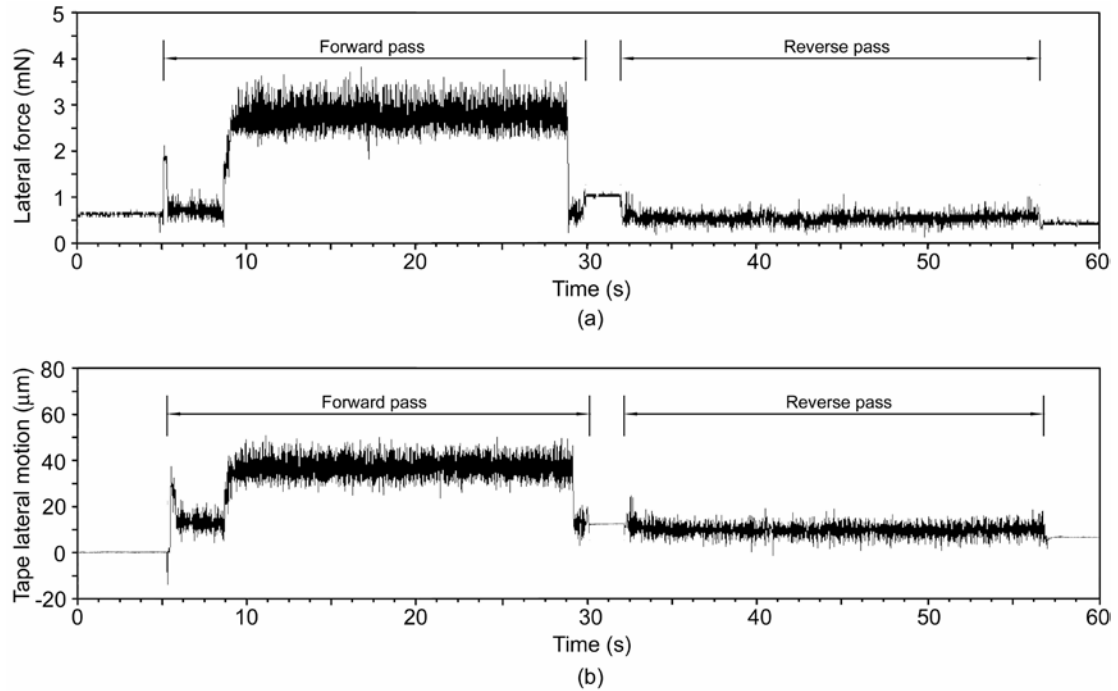


Figure 5.9: Variation of (a) lateral force and (b) tape lateral motion during one cycle. Both measurements were performed at location “Cantilever beam” shown in Fig. 5.1 (a) near the modified guide B.

part of the forward pass (Fig. 5.9 (a)). As observed from Fig. 5.9 (b), the tape rises in lateral direction during the forward pass. If a flanged guide is used, the tape edge rubs against the guide flange and the ridge is formed over the backcoat at the upper edge. During the reverse pass the tape slides along the guide without touching the flanges.

5.3.3 Origin of tape edge damage

It was established that the edges of factory-slit tapes are imperfect and the two edges of a tape strip are different. The magnetic tape that is commercially available comes from slitting of a much wider web of tape into thin strips. Shear-cut slitting is used to perform this operation [Bhushan, 1996, 2000; Rienau, 1979]. In this process, the web of tape is fed between pairs of circular rotating blades (Fig. 5.10, top). The spacing between the blade pair is set to give desired tape width. Fig. 5.10 (center) shows a pair of such blades and how a web is being slit. This technique is similar to the cutting action that is used with a pair of scissors.

As observed from Fig. 5.10 (center), the boundary conditions for the tape edge are different. The edge on the left-hand side is not supported from beneath (backcoat) by the blade, while the edge on the right is supported. Due to the action of the converging blades, bending of the tape occurs and tensile stresses are developed in magnetic coating on the left-hand side and in backcoat on the right-hand side (Fig. 5.10 (center)). It is known from the literature [Bobji and Bhushan, 2001] that if a tensile stress is applied to magnetic tape, cracks develop at the magnetic coating surface perpendicular to the loading direction. It is observed from Fig. 8 (upper edge, unworn tape, magnetic coating) that cracks developed are not strictly parallel with the slit edge. The crack propagation path is altered by the stress component acting in the direction of the web motion due to the tension applied to the web to pull it along the blades. Some cracks can be developed at the backcoat on the right-hand side, which is also bent by a lower blade.

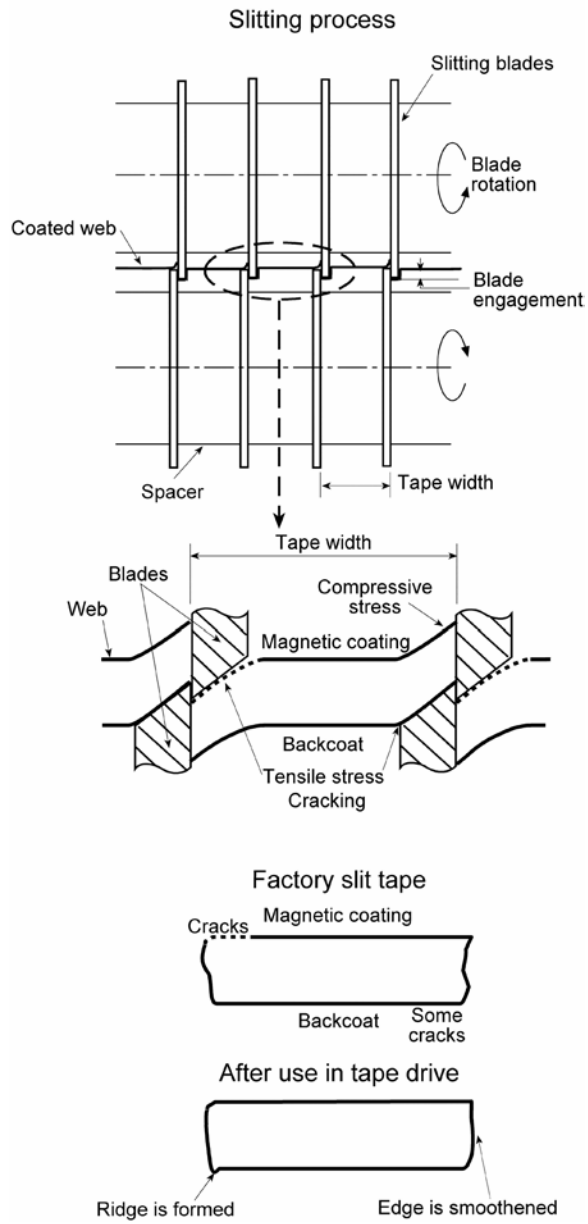


Figure 5.10: Schematic showing formation of tape edge during slitting and after drive use.

However, we did not find any cracks in this region. If any cracks are present, they cannot be distinguished on the rough backcoat.

The final cross-section of a factory-slitted tape can be presented as shown in Fig. 5.10 (bottom). The cross-section of both edges is rough. Cracks were developed at the magnetic coating at one edge (which can be identified as upper edge, according to the definition of views presented earlier). Under normal drive operation due to the tape edge - guide flange interaction, tape edge wears and the tape cross-section takes the shape as shown in Fig. 5.10 (bottom). The mechanism of the edge wear includes material removal as well as material folding resulting from plastic flow from the top of the cross-section to the sides (magnetic coating and backcoat). The cross-section of both tape edges gets smoothed. A ridge is formed over the backcoat at the upper edge. This ridge is not continuous over the tape length and can act as a source of loose debris.

5.4 Summary

A methodology has been developed for evaluation of magnetic tape edge quality. The proposed methodology allows quantitative evaluation of edge damage. Optical microscopy can be used as a fast technique to monitor changes occurring to the edge with sliding. SEM should be used to quantify edge quality. To obtain surface height information, AFM can be used.

Using the methodology developed, it has been established that factory-slitted edges are imperfect and that the two edges differ from each other. The difference in stress distribution for the two edges during tape slitting governs the formation of two different edges. Cracking of magnetic coating at one edge occurs during manufacturing.

The effect of normal drive operation on tape edge quality has been studied. Edge quality degrades after use in a tape drive. One of the edges is prone to produce more debris than the other.

A possible mechanism of the tape edge wear under normal drive operation has been proposed. Cross-section of both edges gets smoothed after use in tape drive. Chunks of magnetic coating are removed at the edges. Continuous sliding results in plastic flow of material from the top of the cross-section to tape sides. This material forms a ridge over backcoat at one edge. The ridge partially tears during sliding and debris particles are formed.

CHAPTER 6

TAPE EDGE STUDY IN A LINEAR TAPE DRIVE WITH SINGLE FLANGED GUIDES

6.1 Introduction

In a linear tape drive, magnetic recording and retrieval processes are accomplished by relative motion between a magnetic head and a magnetic tape. The tape moves through a series of handling devices (reels and guides) designed to control the transverse motion of the tape so that the read heads are able to retrieve data. All modern recorders utilize pre-recorded track following servo patterns on the tape which allows the magnetic heads to remain on track. Long wavelength variations in tape movement are easily followed by servo actuator. However, short wavelength lateral (cross-track) motion of the tape can cause the desired data tracks to move away from the magnetic head and cannot be “followed” by the servo actuator thereby causing a so-called track misregistration (TMR) error. This becomes of more concern for the developers of the future high performance linear tape systems, which will require the use of thinner magnetic tapes, lower track width, higher track densities, higher tape speeds, and lower head-tape spacing in order to increase storage capacity and data transfer rates. Therefore, better tape guiding and tape dimensional stability is needed for better tracking

performance as track widths are reduced and track densities are increased [Bhushan, 2000].

The performance of a tape guiding system is dependent on various parameters, such as type of the guides (e. g., stationary, rotary, and active), quality of virgin tape edge, drive operating parameters (e. g., tape tension and tape speed), mechanical properties of the tape, and tape geometry (e. g., cupping and curvature). It is a common practice to use flanges (edge guides) at both top and bottom of a guide or use a compliant member in one of the guides which pushes the tape against fixed flange [Bhushan, 2000]. Guides minimize lateral tape motion; however, during normal drive operation, the tape edge-guide flange interaction results in damage to the tape edges, leading to problems in tracking, generation of loose tape debris, which then show up at the head-tape interface and cause signal loss. The force exerted by a compliant member of a guide on thinner tapes can result in tape buckling. In a linear tape drive with stationary dual flanged guides, progressive degradation of tape edges with increasing number of cycles is known to be a primary contributor to continuous generation of loose debris and more debris is collected on the head in the vicinity of the tape edges under normal drive operation [Bhushan et al., 1994; Scott and Bhushan, 2000; Bhushan and Mokashi, 2001; Hunter and Bhushan, 2001; Goldade and Bhushan, 2003]. Hunter and Bhushan [2001] and Goldade and Bhushan [2003] reported the existence of a bias in debris distribution over the tape width toward one particular edge of the tape, which is related to the fact that the quality of the two factory-slit tape edges is different.

It is generally known that the quality of the factory slit edge affects guiding performance in a linear tape transport. A straight and smooth edge is desirable for proper

guiding. However, a perfectly smooth edge will result in high real area of contact between itself and edge guides which will increase friction and may cause edge melting at high tape speeds and material transfer onto the guides [Bhushan et al., 1994]. The latter will result in polymer-polymer contact with high friction leading to tape dimensional changes, debris generation and deterioration in the drive tracking and error performance. One should also realize that tape edges are a critical part of the system as well as the guide design. Proper selection of guide type, geometry and material is also crucial.

Based on the above findings it is desirable to have guiding system which minimizes interaction between its components and tape and especially with tape edges. Gavit [1998] and Stahl and Gavit [2001] describe a guiding system incorporating low-flow-rate porous ceramic air-bearing system which provides gentle tape guiding. Pressurized air bearings provide an air cushion to support tape and minimize tape-guide contact. A tapered bearing is used so that the tape is pushed downward against the bottom flange which eliminates the need of a top guide flange. Guides with only one flange minimize tape edge wear.

The objective of the present study is to evaluate guiding and tribological performance of single flanged guides with porous air bearings in a linear tape drive as well as to study the effect of drive operating parameters (speed and tension), tape edge quality and tape thickness on the variation of the lateral tape motion during normal drive operation.

6.2 Experimental details

6.2.1 Description of tape transport

A linear tape transport with a horizontal tape path was used, Fig. 6.1 (a). Drive tests were conducted in a class 10,000 laboratory environment (22 ± 1 °C; relative humidity 45 ± 5 percent). The tape is wrapped around a cylindrical surface formed by four guides (a 75degree segment of a cylinder each) with the magnetic head mounted in the center, to increase its buckling strength. Each guide (Fig. 6.1 (b)) is a porous air bearing consisting of housing, bearing member formed of a porous material, lower flange (datum), and outriggers [Gavit, 1998]. The housing and the bearing member form a plenum connected to an air pump such that air flow through the porous material creates an air cushion to support the tape. When the tape is stationary the flying height is the lowest at the tape edges and higher across the center of the tape [Stahl and Gavit, 2001]. When the tape runs in shoeshine motion at a speed of 4 m/s and tension in the range of 1.25-1.5 N, the flying height increases from 25 μm to 35 μm with the pump pressure increasing from 27.6 kPa to 68.9 kPa [Stahl and Gavit, 2001]. The surface of the bearing member is machined at a small taper angle α (on the range of 0.4 degree, Fig. 6.1 (b), Section AA'), so that the radius of curvature on top is slightly higher than the radius of curvature at the bottom thus providing non-uniform tape tension and tape velocity profile along the tape width. When the tape is in motion, linear velocity of the upper tape edge is higher than that of the lower edge at the flange, which results in appearance of a velocity component which tends to move the tape downwards against the flange, thus creating the lateral force between the guided tape edge and the flange (Fig. 6.1 (b)). The outriggers at each side of the guide provide cleaning action to the tape.

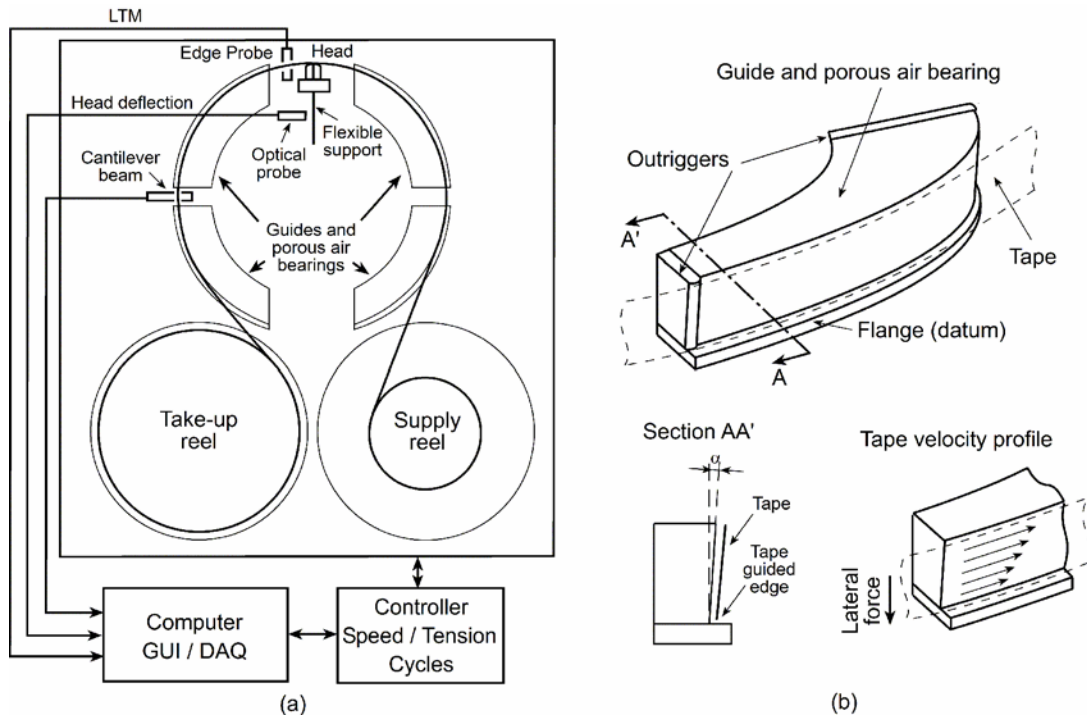


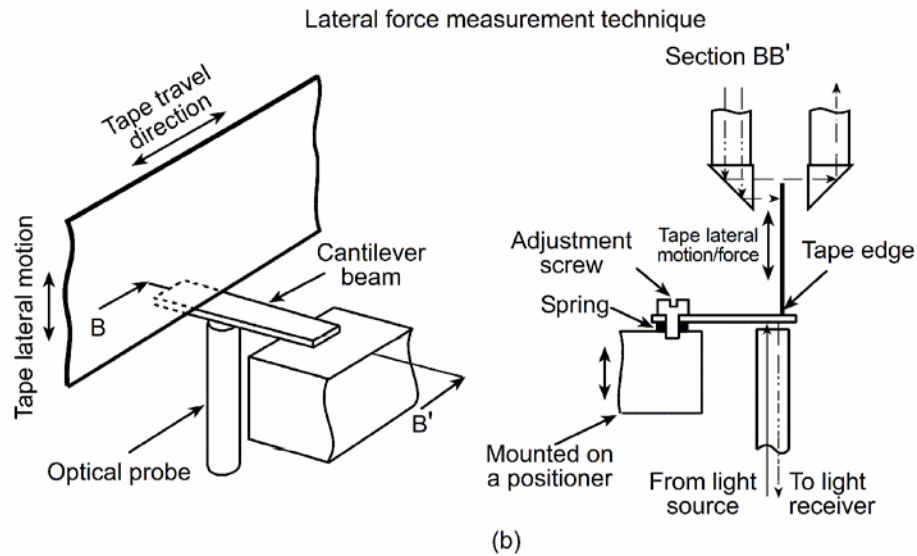
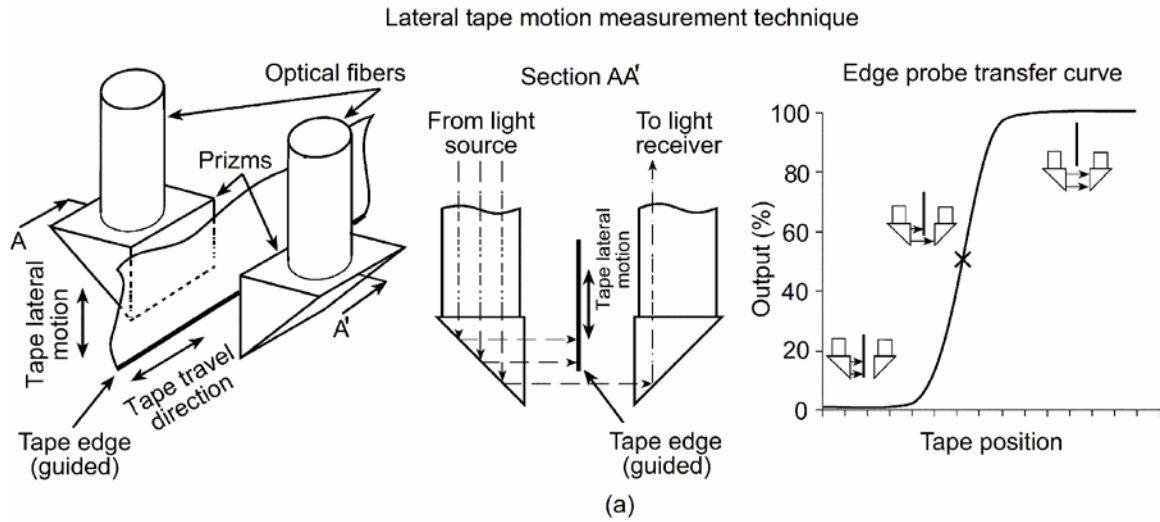
Figure 6.1: (a) Schematic of the tape transport. (b) Origin of downward force.

Tape tension on both sides of the head is monitored by measuring air pressure in the gap between the tape and the bearing member by means of pressure transducers that are mounted in the two guides on each side of the head. The drive controller board provides tension feedback and controls tape speed. The drive can be programmed to run for a specific number of cycles. The communication between the drive controller and a computer is through RS-232 interface and is controlled through a terminal emulator.

A desired tape length is loaded onto a reel and its diameter is used by the controller to calculate instantaneous tape position and speed in the transport. During a tape pass, the angular velocities of both reels are monitored by the controller board to maintain constant tape speed. The maximum length of 9 μm thick tape that can be loaded onto the reel is 600 m. The pass length is set at 100 m for all the tests, if not mentioned otherwise; with one forward and reverse pass equal to one 200 m cycle. The forward pass is defined as the tape travels from the supply to the take-up reel.

6.2.2 Measurement techniques

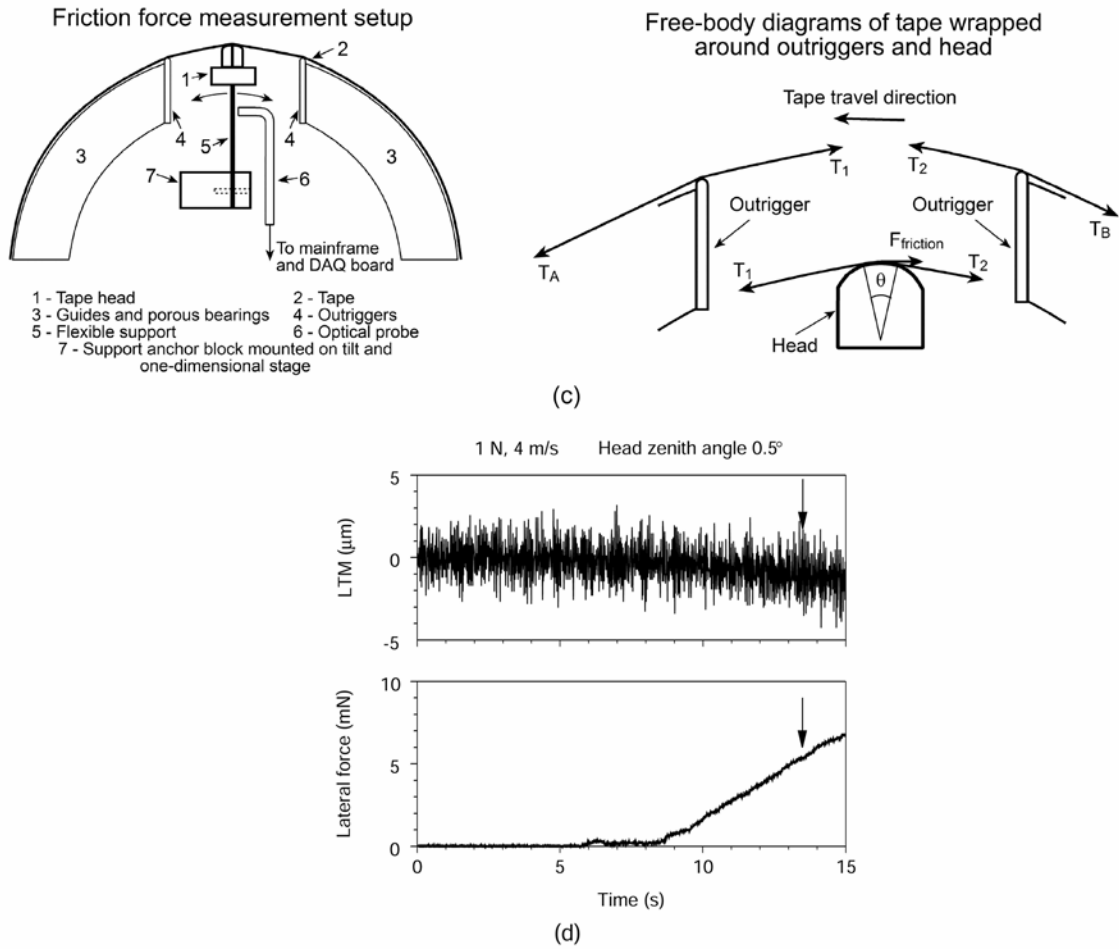
Lateral tape motion was measured by MTI 2000 Fotonic sensor (MTI Instruments Inc., Latham, NY) equipped with Edge Probe (model 2062E with sensitivity of 0.92 $\mu\text{in}/\text{mV}$ (25 $\mu\text{m}/\text{V}$) and noise level of 20 $\text{mV}_{\text{p-p}}$). The location of the edge probe with respect to the tape path in the transport is shown in Fig. 6.1 (a). Figure 6.2 (a) shows the schematic of the tape lateral motion measurement technique. The edge probe is positioned at the guided (lower) tape edge. The light from the light source (Fig. 6.2 (a), Section AA') is reflected by a 90-degree prism to another 90-degree prism and finally reaches photodiode (light receiver). The Fotonic sensor converts the photodiode signal that is proportional to the light intensity into the output units (volts or microinches). If the light path is not obstructed by the tape edge the output of the Fotonic sensor is 100 percent (Fig. 6.2 (a), edge probe transfer curve). The output decreases as the tape moves into the gap between the prisms and vanishes to zero when no light reaches the photodiode. The transfer curve has a linear region in the center of which the reference point is selected corresponding to “zero” lateral displacement. Lateral tape motion is measured with respect to the zero point (cross on the transfer curve in Fig. 6.2 (a)). Power



Continued

Figure 6.2: Schematics showing details of (a) lateral tape motion measurement technique, (b) lateral force measurement technique, and (c) friction force measurement and free-body diagrams of tape. (d) Lateral force measurement.

Figure 6.2 continued



spectral density of lateral tape motion was measured using an HP 35665 spectrum analyzer (Agilent Technologies, Palo Alto, CA). Frequency range from 5 Hz to 105 Hz was analyzed with frequency resolution of 0.25 Hz.

Figure 6.2 (b) shows the details of the schematic of the lateral force measurement technique. Lateral force is the force exerted by the lower tape edge on the flange under drive operation. The values of the lateral force were determined by measuring the deflection of the cantilever beam (a hard drive slider suspension) and converting it into force units. The deflection was measured using proximity MTI 1000 Fotonic sensor with MTI-3804 probe with sensitivity of $6.3 \mu\text{in/mV}$ ($160 \mu\text{m/V}$) and noise level of $25 \text{ mV}_{\text{p-p}}$. Calibration of lateral force was performed by using dead weights. Loads in the range of 0.1- 10 mN were applied to the beam at the point where it touched the tape edge and the displacement was measured by the Fotonic sensor. The linear relationship between the applied force and the Fotonic sensor output was measured to be 7.3 mN/V .

Coefficient of friction was measured as follows, Fig. 6.2 (c). The head was mounted on a flexible support fixed on tilt and one-dimensional stage (to adjust head zenith and wrap angle). When the tape is in motion, the friction force between the tape and the head causes the support to bend. The friction force at the head-tape interface was determined by measuring the deflection of the support and converting it to force units. The deflection was measured using proximity MTI 1000 Fotonic sensor with MTI-3804 probe. Calibration of lateral force was performed by using spring gage. Loads in the range of 50 - 250 mN were applied to the head mounted on the support and the displacement was measured by the Fotonic sensor. The linear relationship between the applied force and the Fotonic sensor output was measured to be 700 mN/V .

The coefficient of friction was calculated by assuming that only tape tension created the normal force on the head and that the tension was the same on both sides of the head. The nominal tape tension T was used. The head wrap angle θ was calculated

from the tape path geometry to be 21 degree. From the free-body diagram of the tape over the head, the coefficient of friction μ , can then be determined as

$$\mu = \frac{\text{Friction force}}{2T \sin\left(\frac{\theta}{2}\right)} \quad (6.1)$$

The edge probe output (LTM in Fig. 6.1 (a)) and the Fotonic sensor output (Head deflection in Fig. 6.1(a)) were captured by a data acquisition board (DAS-16G1, Omega Engineering Inc., Stamford, CT) with a sampling rate of 100 Hz, 150 Hz and 200 Hz at tape speed of 4 m/s, 6 m/s and 8 m/s, respectively. The data acquisition was controlled by Snap-Master V3.2 data acquisition software (HEM Data Corp., Southfield, MI). The lateral tape motion peak-to-peak amplitude was calculated as the difference between the highest and the lowest tape position with respect to the reference point during each pass. The values of coefficient of friction were calculated using Eq. (6.1).

For the lateral force measurements the cantilever beam was positioned near the guide so it just touched the lower tape edge and the edge probe was positioned at the upper tape edge just above the cantilever beam (Fig. 6.2 (b), Section BB'). As the tape moved in the drive, the base of the cantilever beam was manually raised so that the beam pushed the tape. The position of the upper edge was monitored with the edge probe. The edge probe output and the Fotonic sensor output were captured on the computer for future processing. After measurements were complete, the deflection of the cantilever beam was converted into the force units. Figure 6.2 (d) shows sample data used to determine the value of the lateral force. As observed from Fig. 6.2 (d), a certain force is required to change the position of the upper tape edge (to raise the tape as a whole from the flange).

Lateral force was determined as the force required to raise the tape by 1 μm from the flange (indicated by the arrow in Fig. 6.2 (d)).

6.2.3 Test procedure

Two types of test were performed in the study. Short term (20 cycles) tests were carried out to study the effect of tape path geometry, edge quality of the factory-slit tapes and drive operating conditions on guiding performance of the tape transport. Long term wear tests (5000 cycles) were conducted to study the effect of continuous sliding on tape guiding and tape edge degradation. For the short term tests, a new piece of tape (300 m) was loaded into the transport. The center portion (100 m) was used for testing. The effect of head wrap and the head zenith angles on tape guiding were studied at nominal tape tension and tape speed of 1 N and 4 m/s, respectively. Head zenith angle of zero degree corresponds to the taper angle of the porous air bearings and the head is parallel to the tape surface. At zenith angles larger than zero, the top of the head penetrates into the tape path deeper than the bottom of the head. To evaluate the effect of drive operating conditions (tape tension and speed) on tape guiding head wrap angle and zenith angle were set at 21 degree and 1 degree (0.0175 radians), respectively and lateral tape motion at the lower (guided) edge and friction force at the head-tape interface were measured. Guiding performance of the transport was evaluated with tapes from different cartridges and at different reel locations at nominal tape tension and tape speed of 1 N and 4 m/s, respectively, for which full length of the tape from the cartridge (600 m) was loaded into the transport. Head wrap angle and zenith angle were set at 21 degree and 1 degree (0.0175 radians), respectively. Lateral tape motion peak-to-peak amplitude was measured at several reel locations over 100 m long pass.

At the beginning of each long term wear test a new piece of tape (300 m) was loaded into the transport. The center portion (100 m) was used for testing. The head wrap and the head zenith angles were set at 21 degrees and 1 degree (0.0175 radians), respectively. The drive was programmed to run the tape in the transport for 5000 cycles at specified speed and tension. During each test, lateral tape motion at the lower (guided) edge and friction force at the head-tape interface were measured. After the test was completed the worn part of the tape was removed from the transport and manually wound on a spare reel for further analysis. All long term wear tests were performed twice to assure certainty and reproducibility of the results.

For the short term tests the lateral tape motion peak-to-peak amplitude and coefficient of friction were averaged over 20 forward passes and these values were plotted on the graphs. For long term tests, the lateral tape motion peak-to-peak amplitude was calculated during each forward and reverse pass and coefficient of friction was averaged over each forward pass and these values were plotted on the graphs.

6.2.4 Tape edge analysis

Methodology to measure the quality of the magnetic tape edges has been developed by Goldade and Bhushan [2003] after initial attempts by Topoleski and Bhushan [2000]. The methodology is based on characterization of the two tape edges by means of optical microscopy, atomic force microscopy (AFM) and scanning electron microscopy (SEM). Figure 6.3 (a) shows the definition of the views examined in the paper. Optical microscopy was used to image the magnetic coating side and backcoat side at the tape edges and these images were used to quantify the quality of the tape edges using an image analysis technique. AFM was used to analyze single tape layer (edge

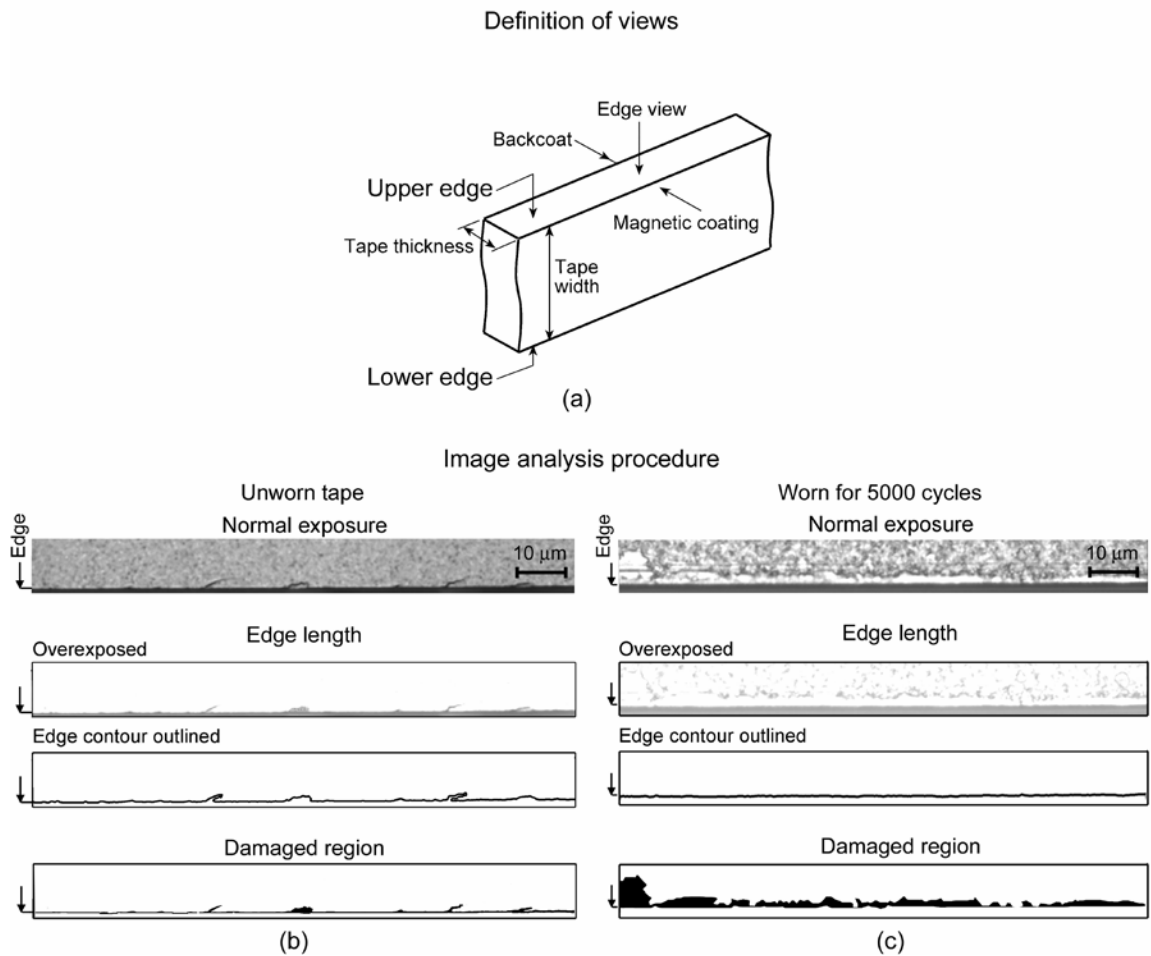


Figure 6.3: (a) Definition of tape edge views used for imaging. Sample optical micrographs illustrating edge quality measurement technique: (b) unworn tape and (c) tape worn for 5000 cycles.

view) to obtain height information. SEM was used to analyze the edges at high resolution to learn about deformation mode. The edges of the unworn (factory-slit) and worn for 5000 cycles tapes were analyzed.

The measures of the tape edge quality are the relative edge contour length and the damaged region near tape edge (number of pixels per unit length). Optical microscopy has been used to photograph magnetic coating and backcoat at the tape edge and these images have been analyzed to measure the edge quality of magnetic coating and backcoat. It is the tape edge view which comes into contact with the guides and is the key to proper guiding. It has been observed that there is a good relationship between the quality of the tape edge at the magnetic coating and backcoat sides and the edge view. Since it is easier to measure edge quality using optical microscopy, this technique is recommended.

For further illustration of the technique, Figure 6.3 (b) shows an optical image of magnetic coating at the lower edge for the unworn tape. By increasing the brightness of the image using image processing software an overexposed image is obtained. There is a distinct border in the overexposed image between the bright white (tape surface) and gray (sample mount) areas, which represents edge contour. With the use of the image processing software, this border is outlined, so that the line constituting the border (edge contour) is continuous and one pixel wide and the length of the edge contour is calculated using the image analysis software. It is also observed from Fig.6.3 (b), that damaged region (cracks and tears) near the tape edge can be easily identified from the overexposed image as dark areas. By applying threshold to the image in the image analysis software (Fig. 6.3 (b), bottom image) these areas (damaged region) are selected and their area is

calculated. However, using threshold option brings in some subjectivity to the measurements. It should also be mentioned, that it was not always possible to identify damaged region by applying the threshold. This was usually true for the tapes used in a tape drive. Figure 6.3 (c) shows the backcoat at the lower tape edge of the tape sample run for 5000 cycles in a tape drive. In this case the damaged region (Fig. 6.3 (c), bottom) was selected manually by outlining it in the image with normal exposure using an appropriate tool in the image processing software, prior to applying threshold in the image analysis software. The relative edge contour length and the damaged region in pixels per unit length were normalized with respect to the length of the optical micrographs analyzed. The numbers reported in the paper are based on the average of ten measurements.

For optical imaging, tape samples cut into 50 mm strips were mounted on a glass microscope slide by using double-sided adhesive tape. Tape was placed such that its edge was approximately 0.3 mm from the adhesive edge of the mounting. Care was taken to assure flatness of the tape sample areas close to the edge. For AFM mapping, maps of the edge view were taken in contact mode. For mapping, a 50 mm piece of tape was pinched between two glass microscope slides with the edge sticking out by about 0.3-0.5 mm over the slides and placed into the AFM (Dimension 3100, Santa Barbara, CA). For SEM analysis, 5-10 mm long tape strips were mounted on a sample holder using conducting adhesive such that the tape edge is sticking over the edge of the holder by 0.3-0.5 mm. SEM images of the edge view were taken at an acceleration voltage of 5 kV (Philips XL30 ESEM). Secondary electrons were collected for imaging.

6.2.5 Head and tape specimens

Commercially available two module read/write head (Travan NS 20, Seagate Technology, Ireland) were used in the study. The schematic of the head along with the thin-film structure are shown in Fig. 6.4 (a). The two read/write modules are embedded in aluminum housing. The thin-film region containing the magnetoresistive (MR) read and inductive write elements is located on the Al_2O_3 -TiC bumps. The length of the head is 16.5 mm and the width is 2.5 mm.

A commercial Ultrium 1 and two experimental tapes on substrates of different thickness were used in the study. All tapes are dual-layer metal particle tapes and are 12.7 mm wide. The overall thickness of the commercial and one of the experimental tapes on a “thick” substrate was 9 μm with magnetic layer and backcoat thicknesses of 0.25 μm and 0.50 μm , respectively; a substrate thickness of about 6.35 μm . The overall thickness of the second experimental tape on a “thin” substrate was 6.4 μm with magnetic layer and backcoat thicknesses of 0.08 μm and 0.55 μm , respectively; a substrate thickness of about 4.57 μm . Figure 6.4 (b) shows a schematic diagram of the tapes. All measurements were performed on commercial tape samples unless mentioned otherwise.

6.3 Results and discussion

We study the effect of tape path geometry (head zenith and wrap angles) on tape guiding (lateral tape motion). The effect of drive operating parameters (tape speed and tension) as well as effect of edge quality of factory-slit tapes from different cartridges on guiding performance of the single flanged guides with low-flow-rate porous ceramic air bearings is evaluated. Long term wear tests are performed to study the effect of continuous sliding on tape guiding and edge damage.

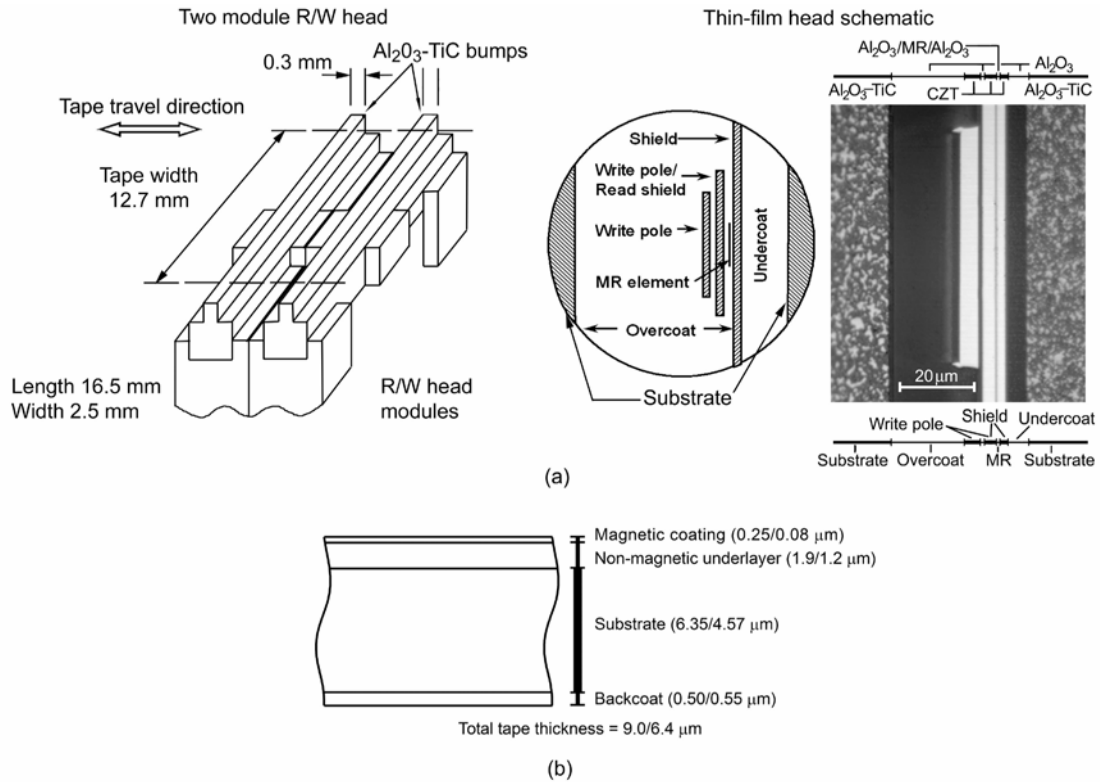
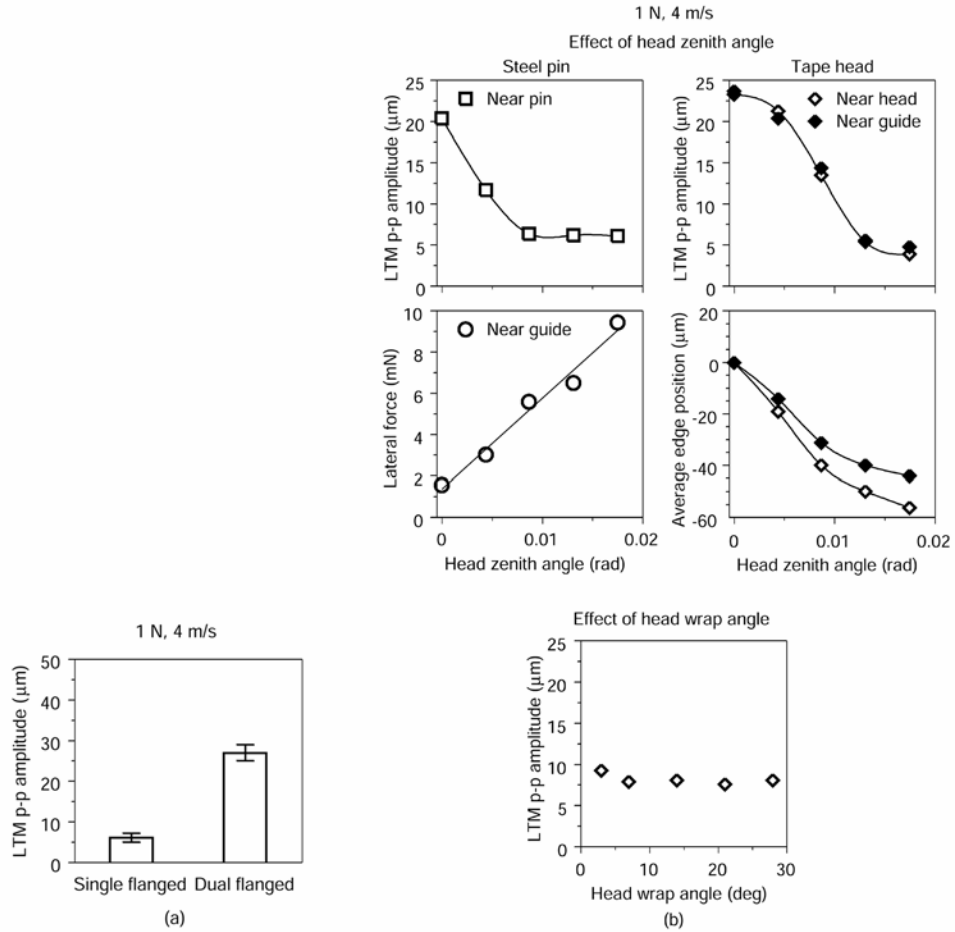


Figure 6.4: (a) General view and thin-film region of the tape head. (b) Schematic diagram of MP tape.

6.3.1 Effect of tape path geometry during short term tests

6.3.1.1 Single flanged vs. dual flanged guides

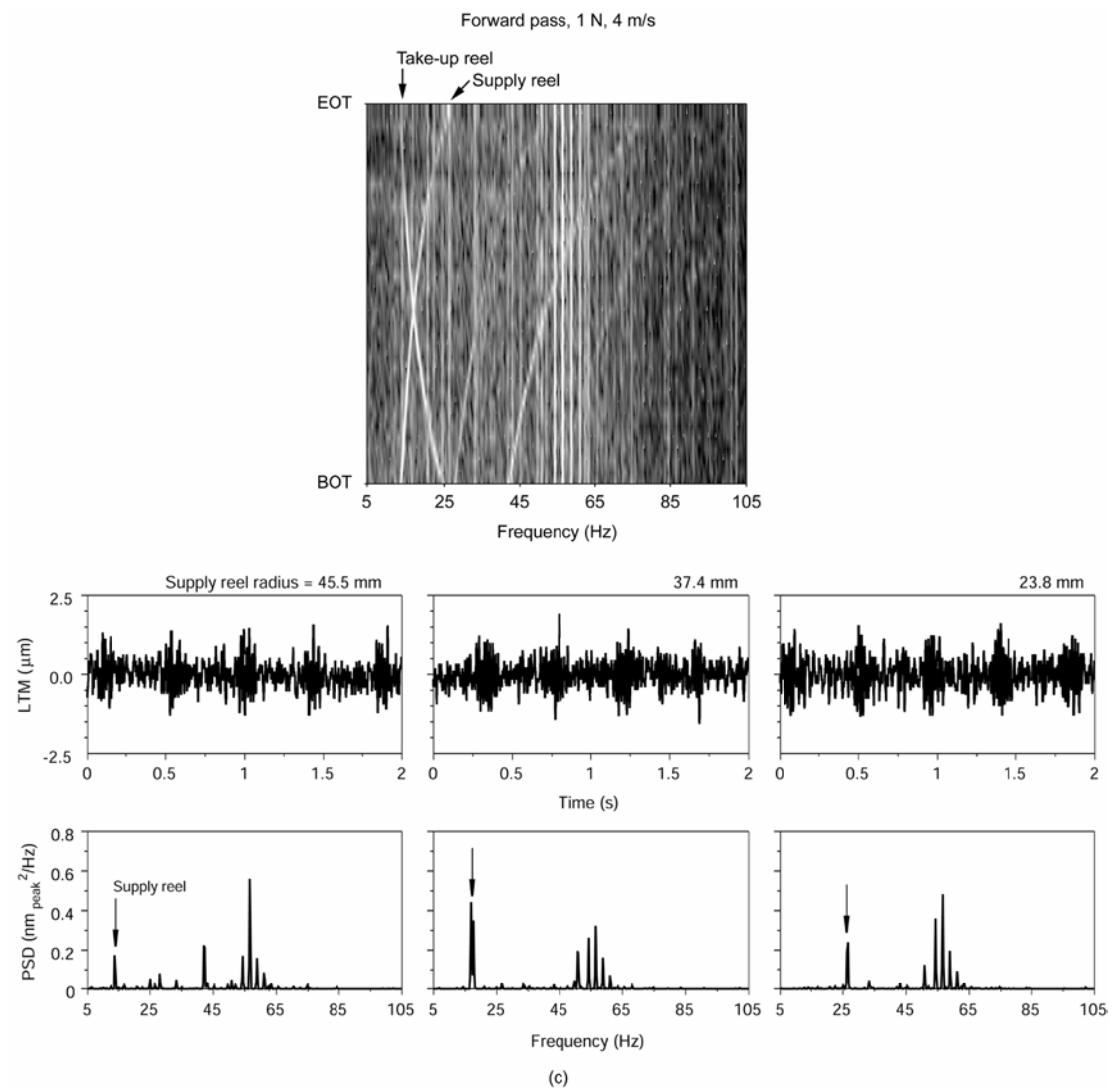
Guide type is one of the factors affecting LTM. Figure 6.5 (a) shows LTM measured on the tape transports with single flanged guides. The data for the tape transport equipped with dual flanged stationary guides reported by the authors [Goldade



Continued

Figure 6.5: (a) Comparison of guiding performance of drives with different guide types. (b) Effect of tape path geometry (head zenith and wrap angles) on lateral tape motion peak-to-peak amplitude and lateral (guiding) force at 1 N and 4 m/s. (c) Power spectral density of the lateral tape motion. Transition from black to white on the spectral map covers range from 10^{-5} $\text{nm}_{\text{peak}}^2/\text{Hz}$ to $1 \text{ nm}_{\text{peak}}^2/\text{Hz}$ in logarithmic scale. Brighter areas correspond to higher values of power spectral density.

Figure 6.5 continued



and Bhushan, 2003] is also presented for comparison. As observed from Fig. 6.5 (a), LTM peak-to-peak amplitude is less for the tape transport with single flanged porous air bearing guides as compared to the dual flanged guides because of the lateral force that keeps the tape at the flange and thus LTM is low.

6.3.1.2 Effect of head orientation

As described earlier (Fig. 6.2 (b)), the tape, wrapped over the guides, is pushed downward and is pressed against the datum flange when the tape is in motion. The magnitude of the lateral force governs the stress distribution at the tape edge – guide flange interface which determines the amount of wear the tape edge experiences during normal drive operation. We measured the lateral force exerted by the guide flange on the tape edge with a steel pin replacing the head (as shipped from the manufacturer) using the technique for lateral force measurements. Figure 6.5 (b) shows the effect of steel pin zenith angle on the LTM peak-to-peak amplitude and lateral force at tape tension of 1 N and tape speed of 4 m/s. Zero zenith angle corresponds to the pin aligned parallel to the tape. As observed from Fig. 6.5 (b), with zenith angle increasing (top of the pin penetrating deeper into the tape path) from zero to 0.087 radians (0.5 degrees) the LTM peak-to-peak amplitude decreases from 20.4 μm to 6.4 μm and remains at that level with further increase in zenith angle. The lateral force increases linearly from 1.5 mN to 9.5 mN with the zenith angle increasing from zero to 0.0175 radians (1 degree). A simple model can be used to explain the observed linear increase of the lateral force with zenith angle increase. The magnitude of the lateral force can be expressed as

$$F_{\text{lateral}} = N \sin(\theta_{\text{zenith}}), \quad (6.2)$$

where N is normal force acting on the tape and θ_{zenith} is the head zenith angle. If the angle is small, then $\sin(\theta_{\text{zenith}}) \approx \theta_{\text{zenith}}$, this gives linear relationship between the magnitude of the lateral force and zenith angle.

Figure 6.5 (b) also shows variation of the LTM peak-to-peak amplitude and average edge position measured at the guided edge for the head zenith angles in the range from zero to 0.0175 radians (1 degree) at two locations: near the tape head and near the guide. Zenith angle of zero radians is selected as a reference for the average edge position and all other numbers reflecting average edge position are determined with respect to this reference. As observed from Fig. 6.5 (b), the LTM peak-to-peak amplitude decreases and average edge position becomes more negative (the edge moves down) at both locations with the head zenith angle increasing. It is also observed, that by increasing the head zenith angle from 0.0131 radians to 0.0175 radians (0.75 degrees to 1 degree) the LTM peak-to-peak amplitude changes only from 5.5 μm to 4 μm near the head. It is further observed, that the average edge position near the head is below that near the guide. Tape velocity gradient and lateral force increase with zenith angle increasing. As there is no flange to support the tape at the head, the tape deforms and slides down farther over the head. Thus, taper angle of the air bearing can be increased to minimize LTM; however, larger angle will result in higher lateral force, so an optimal value should be selected to minimize both LTM and tape edge wear.

The effect of head wrap angle on LTM peak-to-peak amplitude was studied (Fig. 6.5 (b)). The measurements were performed with head zenith angle of 1 degree at tape tension of 1 N and tape speed of 4 m/s. No significant change in LTM peak-to-peak amplitude was found in the range of wrap angles from 3 to 28 degree. In order to

minimize LTM, all further measurements as well as long term wear tests were performed with the head zenith angle and head wrap angle of 0.0175 radians (1 degree) and 21 degree, respectively.

Figure 6.5 (c) shows power spectral density (PSD) of the lateral tape motion. The measurements were performed during the 580 m forward pass at 1 N and 4 m/s. LTM was measured during the pass and the signal was captured at a sampling rate of 1000 Hz. Thirty four spectra were taken during the pass and those are mapped in Fig. 6.5 (c). The transition from black to white on the spectral map covers range from $10^{-5} \text{ nm}_{\text{peak}}^2/\text{Hz}$ to $1 \text{ nm}_{\text{peak}}^2/\text{Hz}$ in logarithmic scale. Brighter areas correspond to higher values of power spectral density. The bottom of the map corresponds to the beginning of tape (BOT) with all tape wound on the supply reel (supply reel radius is 45.5 mm). At the top of the map, designated as end of tape (EOT), all tape is wound on the take-up reel (supply reel radius is 23.8 mm). The plots in Fig. 6.5 (c) shows real time LTM and corresponding PSD at specified radii of the tape remaining on the supply reel. As observed from Fig. 6.5 (c), that there are two peaks in the range of frequencies from 14 Hz to 28 Hz, which shift as the tape is unwound from the supply reel. These peaks were found to be at the instantaneous rotational frequencies of the reels. Motor shaft run out, reel hub eccentricity and reel misalignment are among possible causes for these frequencies to show up in the spectra. It is also observed from Fig. 6.5 (c), that the peaks in the range of frequencies from 50 Hz to 65 Hz were present in all spectra, which we believe result from the tape width variation.

6.3.1.3 Different cartridges and reel locations

Commercially available tape samples were used in the study. We characterized the quality of the tape samples by performing initial measurements of LTM peak-to-peak amplitude at 1 N and 4 m/s for which 600 m of tape from a cartridge was loaded onto the transport and measurements were performed over 100 m tape segments with different amount of tape on the supply reel. Figure 6.6 shows LTM peak-to-peak amplitude versus different cartridges, different reel radial locations and relative edge contour length. The reel radius on the plot designates the radius of tape on the supply reel in the beginning of the 100 m pass. As observed from Fig. 6.6, the variation of LTM peak-to-peak amplitude for different cartridges is on the range from 4.5 μm to 7.8 μm . It is further observed from Fig. 6.6, that LTM peak-to-peak amplitude is higher, when the amount of the tape on the supply and the take-up reels is the same and tape vibrations are excited at rotational frequencies of the reels that are close to each other.

In order to explain the variation of the LTM peak-to-peak amplitude for different cartridges, we performed analysis of the edge quality of the unworn tape samples from each cartridge. Figure 6.7 (a) shows sample optical images of magnetic coating and backcoat at tape edges for the two tapes from different cartridges. The quality of the magnetic coating at upper and lower edges of both tapes is different, which agrees with the results reported by the authors [Goldade and Bhushan, 2003]. Cracks and/or tears can be identified at the upper edge. The magnetic coating at the lower edge seems to have fewer cracks and tears. No significant difference can be found for the backcoat at both edges from optical micrographs. It is further observed from Fig. 6.7 (a), that one of the

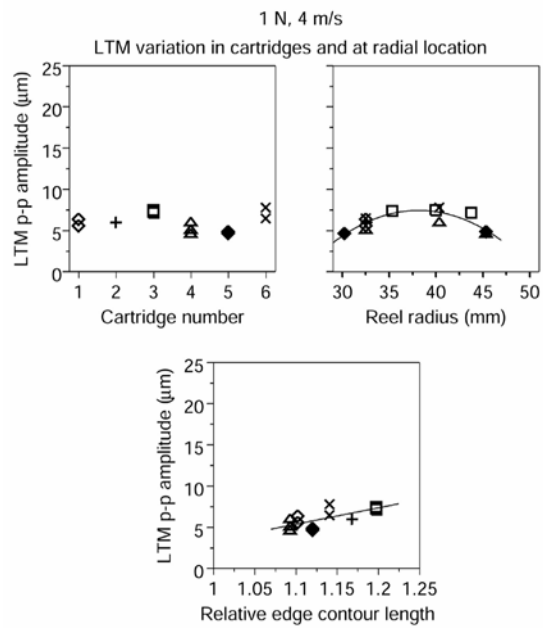


Figure 6.6: LTM variation versus cartridges, radial reel locations and edge quality of unworn tape at 1 N and 4 m/s. The relative edge contour length was averaged over four tape edges for each tape sample.

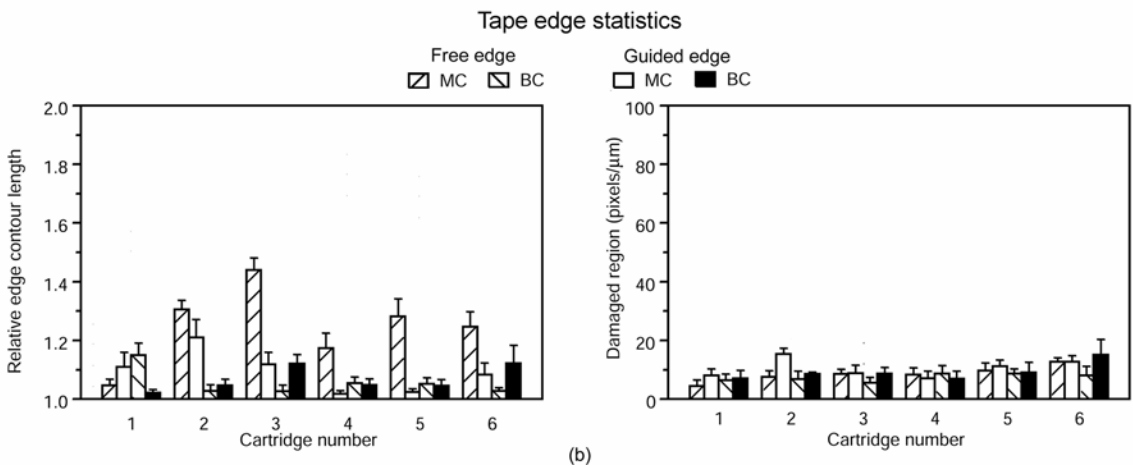
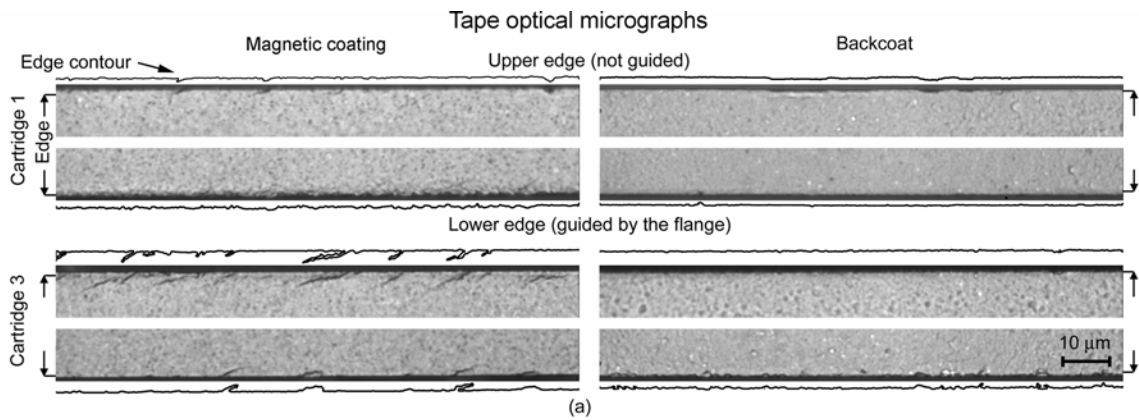


Figure 6.7: (a) Sample optical micrographs of unworn tape edges from two different cartridges. (b) Tape edge statistics. Optical micrographs of 112 μm along length (640 pixels) and 11.2 μm along width (64 pixels) were analyzed. MC - magnetic coating, BC - backcoat.

tapes (from cartridge 3) has more defects at the edges. Some variation in edge quality from one cartridge to another exists.

The quality of the magnetic coating and the backcoat at the tape edges was quantified next. Figure 6.7 (b) shows tape edge statistics for the unworn samples of the commercial tape used in the study. Optical micrographs of 112 μm along length (640 pixels) and 11.2 μm along width (64 pixels) were analyzed. The relative edge contour length and number the damaged region in pixels per unit length are presented in Fig. 6.7 (b). Each number reported is based on ten measurements. Based on the quantitative results, magnetic coating at one of the edges experiences most of the damage during factory-slitting. Cracking of magnetic coating at one edge occurs during manufacturing. This supports the notion, that the difference in stress distribution for the two edges during tape slitting governs the formation of two different edges [Goldade and Bhushan, 2003]. It is also observed from Fig. 6.7 (b) that the edge contour length is generally increases with edge damage increasing.

Therefore, the observed variation of the LTM peak-to-peak amplitude from one cartridge to another can be attributed to the variation in edge contour length. Figure 6.6 shows the effect of edge quality (relative edge contour length) on LTM peak-to-peak amplitude. Relative edge contour length in this specific figure was averaged over four tape edges (two for magnetic coating and two for backcoat) for each tape sample. As observed from Fig. 6, with the relative edge contour length increasing, LTM peak-to-peak amplitude tends to increase.

6.3.1.4 Effect of speed and tension

Figure 6.8 shows effect of tape speed and tension on LTM peak-to-peak amplitude and coefficient of friction for the tape sample from one cartridge. As observed from Fig. 6.8, LTM peak-to-peak amplitude does not change significantly over the range of speeds and tensions evaluated. It is also observed from Fig. 6.8, that coefficient of friction decreases at constant tension with speed increasing, and increases at constant speed with tension increasing. As the tape speed is increased, the air bearing effect at the head-tape interface becomes more pronounced, which results in a decrease in the friction force and coefficient of friction. As tape tension is increased, the air bearing effect diminishes, which increases friction force.

6.3.2 Changes in LTM during long term testing

6.3.2.1 Effect of speed and tension

We studied the effect of tape speed and tape tension on variation of LTM peak-to-peak amplitude and coefficient of friction at the head-tape interface during long term wear tests. It should be noted that the tests were performed using tape from different cartridges, so the variation in LTM peak-to-peak amplitude in the beginning of sliding is not because of the tape speed/tension, but rather due to the variation in tape edge quality from one cartridge to another.

Fig. 6.9 (a) shows the effect of tape speed at constant tension of 1 N on LTM peak-to-peak amplitude and coefficient of friction. As observed from Fig. 6.9 (a), at low (4 m/s) and moderate (6 m/s) speed LTM peak-to-peak amplitude does not change with sliding through the test. LTM peak-to-peak amplitude is about 6 μm at 4 m/s and 7.5 μm

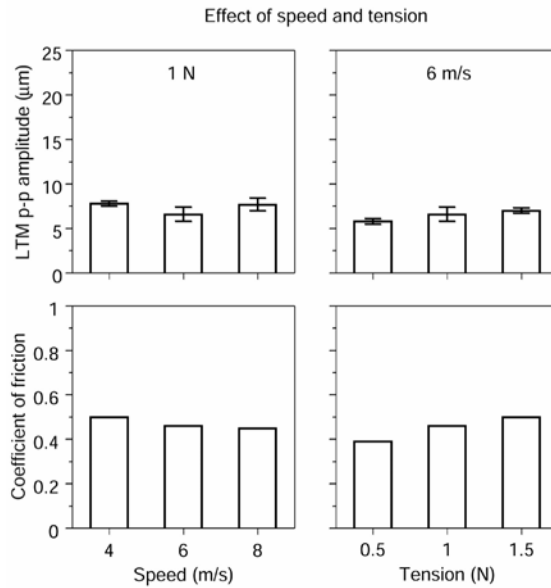


Figure 6.8: Effect of tape tension and speed on lateral tape motion peak-to-peak amplitude and coefficient of friction.

at 6 m/s during both forward and the reverse passes. It is further observed from Fig. 6.9 (a) that at 8 m/s the LTM peak-to-peak amplitude remains low ($5 \mu\text{m}$) during the first 200 cycles, after which it gradually increases with the number of cycles increasing. At 1600 cycles, a sudden increase in LTM peak-to-peak amplitude from $8 \mu\text{m}$ to $12 \mu\text{m}$ occurs during the reverse pass, which is accompanied by a gradual increase during the forward pass. With further sliding, some sporadic variation in LTM peak-to-peak amplitude during both passes is observed, however the trend is increasing. In the end of

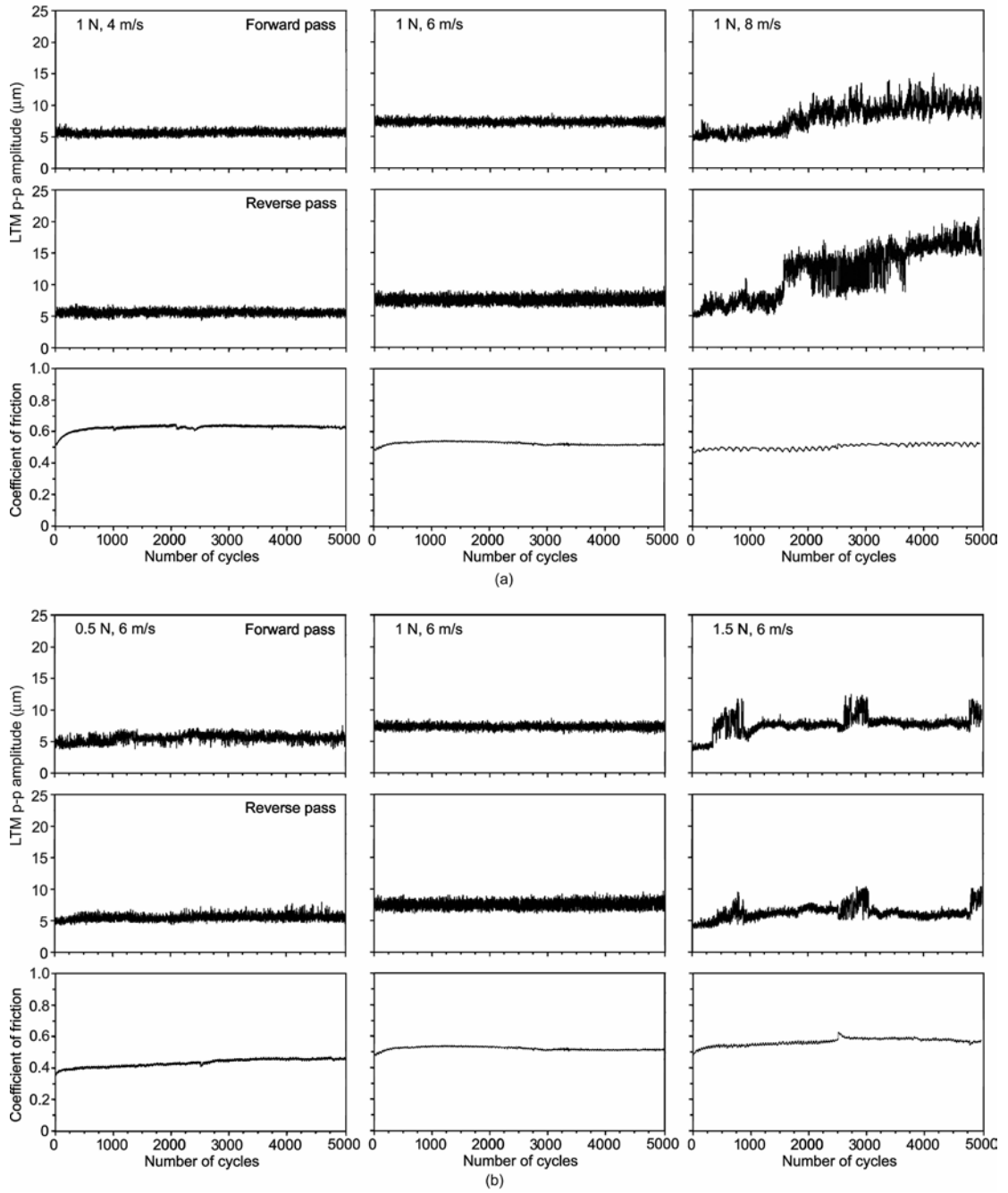


Figure 6.9: Variation of lateral tape motion peak-to-peak amplitude and coefficient of friction as a function of number of cycles. Effect of (a) tape speed and (b) tape tension.

testing the LTM peak-to-peak amplitude reaches the values of 10 μm and 18 μm during the forward and reverse passes respectively.

As observed from Fig. 6.9 (a), at constant tension coefficient of friction noticeably increases in the beginning of sliding during the tests performed at 4 m/s and 6 m/s, after which it remains constant. It increases from 0.52 to 0.62 during the first 800 cycles at 4 m/s and from 0.49 to 0.52 during the first 400 cycles at 6 m/s. The coefficient of friction slowly increases from 0.47 at the beginning of sliding to 0.53 at the end of testing for the test performed at 8 m/s.

Figure 6.9 (b) the effect of tape tension at constant speed of 6 m/s on LTM peak-to-peak amplitude and coefficient of friction. At low (0.5 N) and moderate (1 N) tension LTM peak-to-peak amplitude does not change significantly with sliding through the test. LTM peak-to-peak amplitude is about 5.0 μm at 0.5 N and 7.5 μm at 1 N during both forward and the reverse passes. However, at lower tension, variation of LTM peak-to-peak amplitude through the duration of the test is higher. It is further observed from Fig. 6.9 (a) that at 1.5 N the LTM peak-to-peak amplitude remains low (4.5 μm) during the first 400 cycles, after which it abruptly increases to 7 μm during the forward pass and remains at this level for the next 400 cycles. During the reverse pass a gradual increase is observed. At about 800 cycles LTM peak-to-peak amplitude drops to 6 μm for both forward and reverse passes. With the number of cycles increasing, LTM peak to peak amplitude increases to 8 μm and 7 μm for the forward and reverse pass, respectively, and at 2600 cycles another abrupt increase in LTM peak-to-peak amplitude occurs. With further sliding, LTM peak-to-peak amplitude drops to 8 μm and 6.5 μm for the forward

and reverse pass, respectively. At the end of testing, another sporadic increase in LTM peak-to-peak amplitude is observed.

According to Stahl and Gavit [2001] formation of the staggered wraps (tape layers sticking above the surrounding pack on the reels) increases LTM. Figure 6.10 shows optical photographs of the supply reel after the wear tests at 1 N and 4 m/s and at 1 N and 8 m/s were completed. The upper reel flange was removed in order to take the photograph. The tape pack on the reel had no winding defects after the test performed at 1 N and 4 m/s. Staggered wraps formed at high tape speed. During winding hydrodynamic air film is formed between the incoming tape and that already wound on the reel. Part of the air is squeezed out at the next wrap but part of it is locked in. The

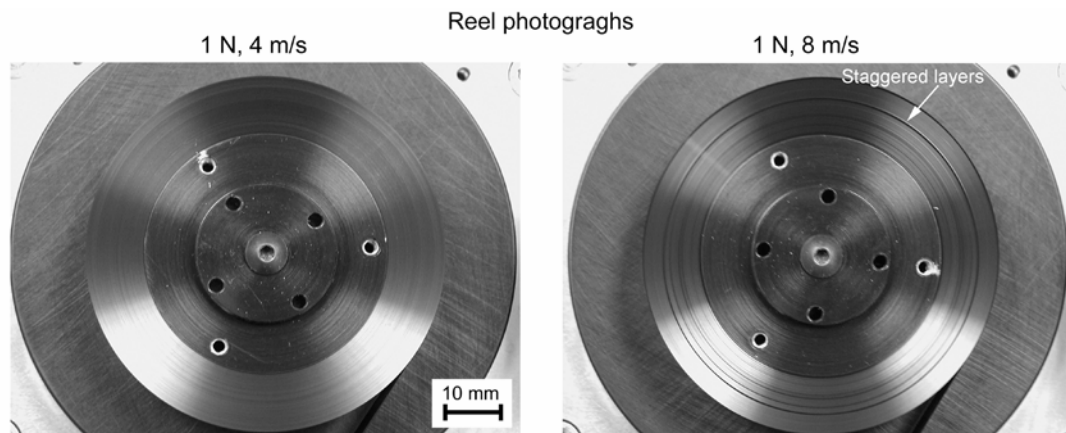


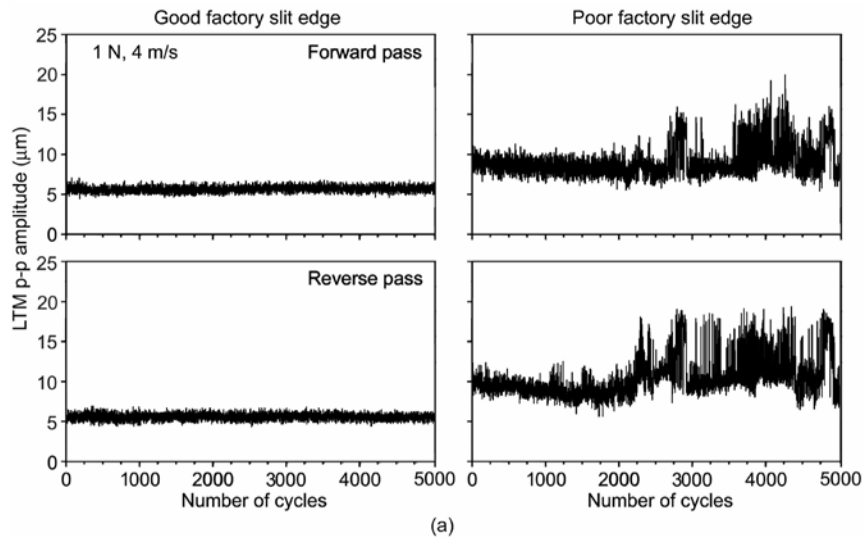
Figure 6.10: Sample optical photographs taken at the end of testing showing formation of staggered layers at high tape speed.

thickness of the air film increases with the tape speed increasing and tape tension decreasing [Bhushan, 2000, p. 435-436]. During winding at high tape velocities this air film prevents from formation of a tight pack on reel, which allows adjacent tape layers to slip against each other. At high tension, tension ridges can appear and air pockets can form in the pack making interlayer slip possible.

The trends observed for the coefficient of friction can be explained as follows. In the beginning of sliding the larger asperities on the tape surface wear down (tape burnishes). Burnishing of the tape asperities [Bhushan and Mokashi, 2001; Patton and Bhushan, 1997] may result in an increase in the real area of contact responsible for an increase in friction [Bhushan, 1996, p. 239]. The rate at which asperities wear down depends on the tape flying height governed by the air bearing effect at the head-tape interface. As the tape speed is decreased and/or tension is increased, the air bearing effect at the head-tape interface becomes less pronounced and a larger number of tape asperities interact with the head surface. This results in a larger real area of contact and higher coefficient of friction at low sliding velocities and/or higher tension.

6.3.2.2 Effect of edge quality of factory-slit tapes

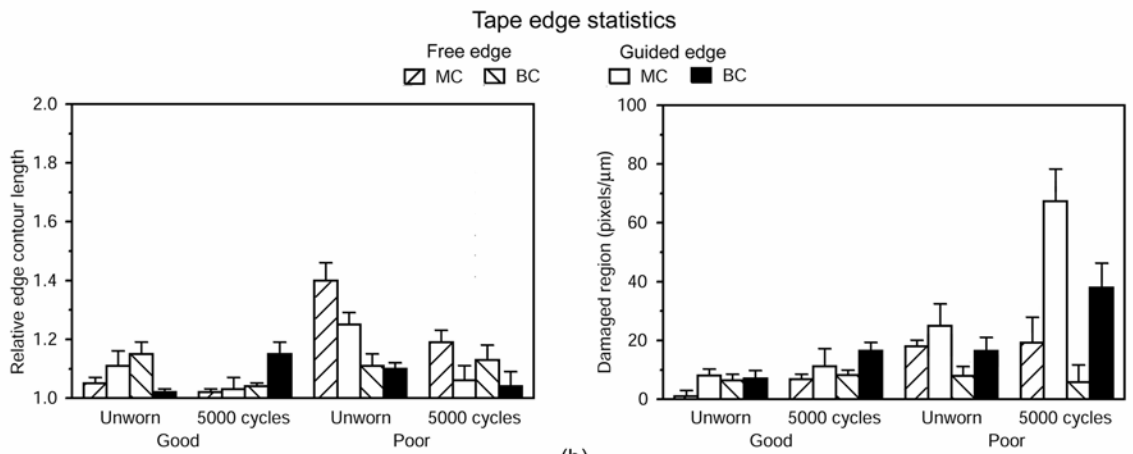
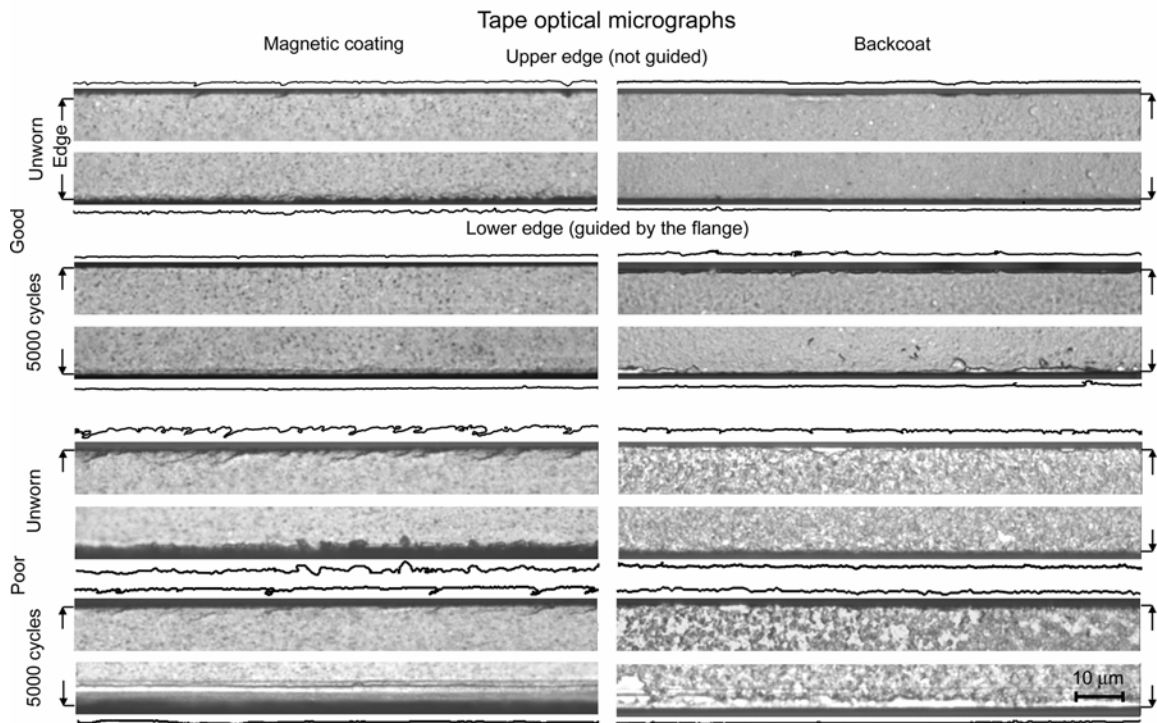
It was established in the present study that edge quality of the factory-slit tape affects guiding performance in a linear tape transport. In the current section we studied the effect of initial edge quality on long term guiding performance. Two tape samples with different initial edge quality were used (Fig. 6.11 (b), to be presented later). One of the tape samples was the commercial tape; the other was the experimental tape on “thick” substrate. The total thickness of both tapes was 9 μm . Figure 6.11 (a) shows variation of the LTM peak-to-peak amplitude for the two tapes during the test performed at 1 N and



Continued

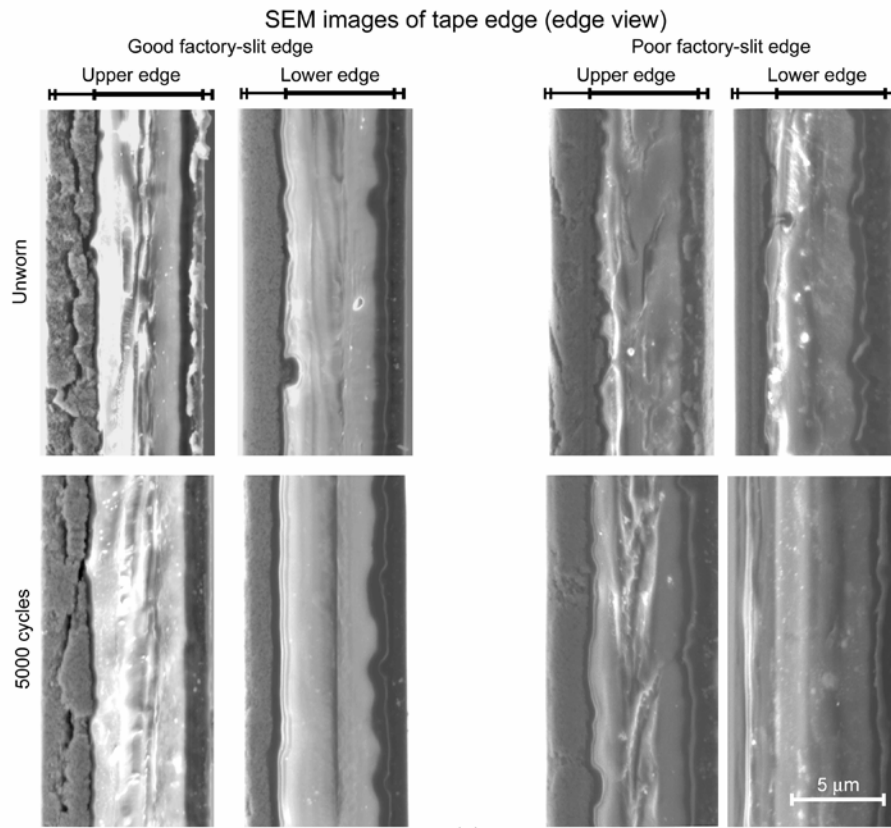
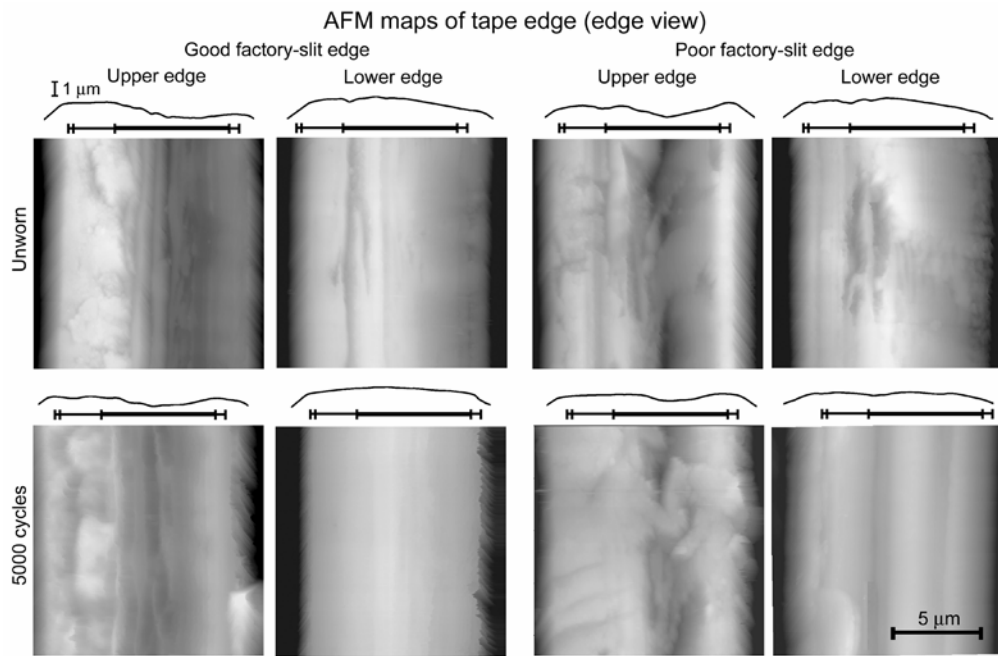
Figure 6.11: Effect of edge quality of factory-slit tape on lateral tape motion during long term wear tests. (a) Variation of lateral tape motion peak-to-peak amplitude as a function of number of cycles for two tapes with different initial edge quality. (b) Tape edge statistics. Optical micrographs of 112 μm along length (640 pixels) and 11.2 μm along width (64 pixels) were analyzed. MC - magnetic coating, BC - backcoat. (c) AFM maps and SEM images of tape edge (edge view). Surface profiles presented for AFM images were averaged over the entire scan. (d) Measured cupping profiles at 0 N and 1 N tensions. Magnetic coating is at the bottom (negative cupping). (e) Head contamination close to tape edges after 5000 cycles.

Figure 6.11 continued



Continued

Figure 6.11 continued



(c)

Continued

4 m/s. As observed from Fig. 6.11 (a), LTM peak-to-peak amplitude does not change during the test with commercial (good factory-slit edge) tape. It remains at about 6 μm for both forward and the reverse passes. The LTM peak-to-peak amplitude for the experimental tape (poor factory-slit edge) is high in the beginning of sliding (9 μm and 10 μm for the forward and reverse pass, respectively). It slightly decreases with the number of cycles increasing. At about 1900 cycles the variation in LTM peak-to-peak amplitude from one cycle to another starts to increase and at 2200 cycles it reaches 10 μm . With further sliding the LTM peak-to-peak amplitude reaches 19 μm .

Figure 6.11 (b) shows sample optical micrographs of the tape edges and tape edge statistics for the unworn tapes and after use in the tape drive. Cracks and tears can be identified on the magnetic coating at the upper edge of both tapes for the unworn tapes. The area of the damaged region at the edges is higher for the tape with poor factory-slit edges. Magnetic coating at the lower edge of the tape with poor factory-slit edges has a rough contour with chunks of material missing. The relative edge contour length is high for the magnetic coating at both edges of the tape with poor edge quality. It is further observed from Fig. 6.11 (b), that the damaged region at the free edges of both tapes did not increase significantly after use in the tape drive. The damage to the guided edge of the tape with poor initial edge quality can be easily characterized by using AFM and SEM of the edge view. Figure 6.11 (c) shows AFM analysis and SEM images of the edge view of the factory-slit tapes and after use in the tape drive. In the AFM maps of a tape single layer brighter areas correspond to higher points. Surface heights information should be read from the averaged profile presented for each image. As observed from Fig. 6.11 (c) the edge views of factory-slit (unworn) tapes are not flat. After the use in tape drive the

upper (not guided) edge of both tapes did not change and the edge view at the guided edge got smoothened. The tape thickness at the lower (guided) edge of the poor factory-slit tape increased due to the formation of the ridge at the backcoat. The SEM image of the guided edge of poor factory-slit tape (Fig. 6.11 (c)) in the end of sliding shows that magnetic coating and underlayer were partially removed at the edge.

Magnetic tape is not a flat strip. A tendency of tape to curl about an axis perpendicular to the direction of travel along the tape width exists [Bhushan, 2000; Scott and Bhushan, 2003]. This tendency is called tape cupping. In negative cupping the edges of tape are farther from the head. Tape cupping can be one of the factors affecting LTM. Cupping measurements were performed using an optical microscope an optical microscope as described earlier. Figure 6.11 (d) shows profiles along the width of the tape for the unworn tapes with different quality of the factory-slit edges with 0 N and 1 N tension applied. As observed from Fig. 6.11 (d), the commercial tape (good factory-slit) has negative cupping at tension of 0 N. However, cupping of both tapes is zero with tension 1 N applied, which implies that tape cupping is insignificant factor to be responsible for the observed changes in LTM.

Optical micrographs of the head after the use in tape drive with tapes with different factory-slit edge quality were taken over the head area that was in contact with tape edges, Fig. 6.11(e). As observed from Fig. 6.11 (e) there is a bias in debris distribution over the tape width. The upper part of the head was in contact with upper (not guided) tape edge, which did not experience damage during sliding and no debris were found over this area. Small amount of loose debris (they were easily removed with dry cotton swab) appeared over the area of the head that was in contact with the guided

edge of the good factory-slit tape. The guided edge of the poor factory-slit tape experienced severe damage during the test which resulted in accumulations of significant amount of debris at the bottom part of the head.

6.3.2.3 Effect of tape thickness

With the thickness of the media decreasing, the stresses developed in the tape during drive operation increase. It was established in the present study that LTM is high during drive operation at high tension (high stress applied to the media), Fig. 6.9 (b). We studied the effect of tape thickness on changes in LTM and coefficient of friction during long term test, Fig. 6.12 (a). The tape sample used was an experimental media with the overall tape thickness of 6.4 μm . The test was performed at tape tension and speed of 1 N and 6 m/s, respectively. As observed from Fig. 6.12 (a) the LTM peak-to-peak amplitude is on the range of 5 μm to 6 μm during the forward pass for the duration of test. During the reverse pass sporadic increases in the LTM peak-to-peak amplitude up to 8 μm are observed. The coefficient of friction gradually increases from 0.56 in the beginning of sliding to 0.72 at the end of testing (Fig. 6.12 (a)). The rate of increase slows down with increasing sliding distance. Burnishing of the tape asperities [Patton and Bhushan, 1997] may result in an increase in the real area of contact responsible for an increase in friction [Bhushan, 1996, p. 239].

Following the wear test, we performed optical analysis of magnetic coating and backcoat of unworn tape and tape worn for 5000 cycles and quantified quality of the edges. The relative edge contour length and the damaged region were measured. Figure 12 (b) shows sample optical micrographs of the tape edges and tape edge statistics for the unworn tape and after 5000 cycles in the tape drive. As observed from Fig. 6.12 (b),

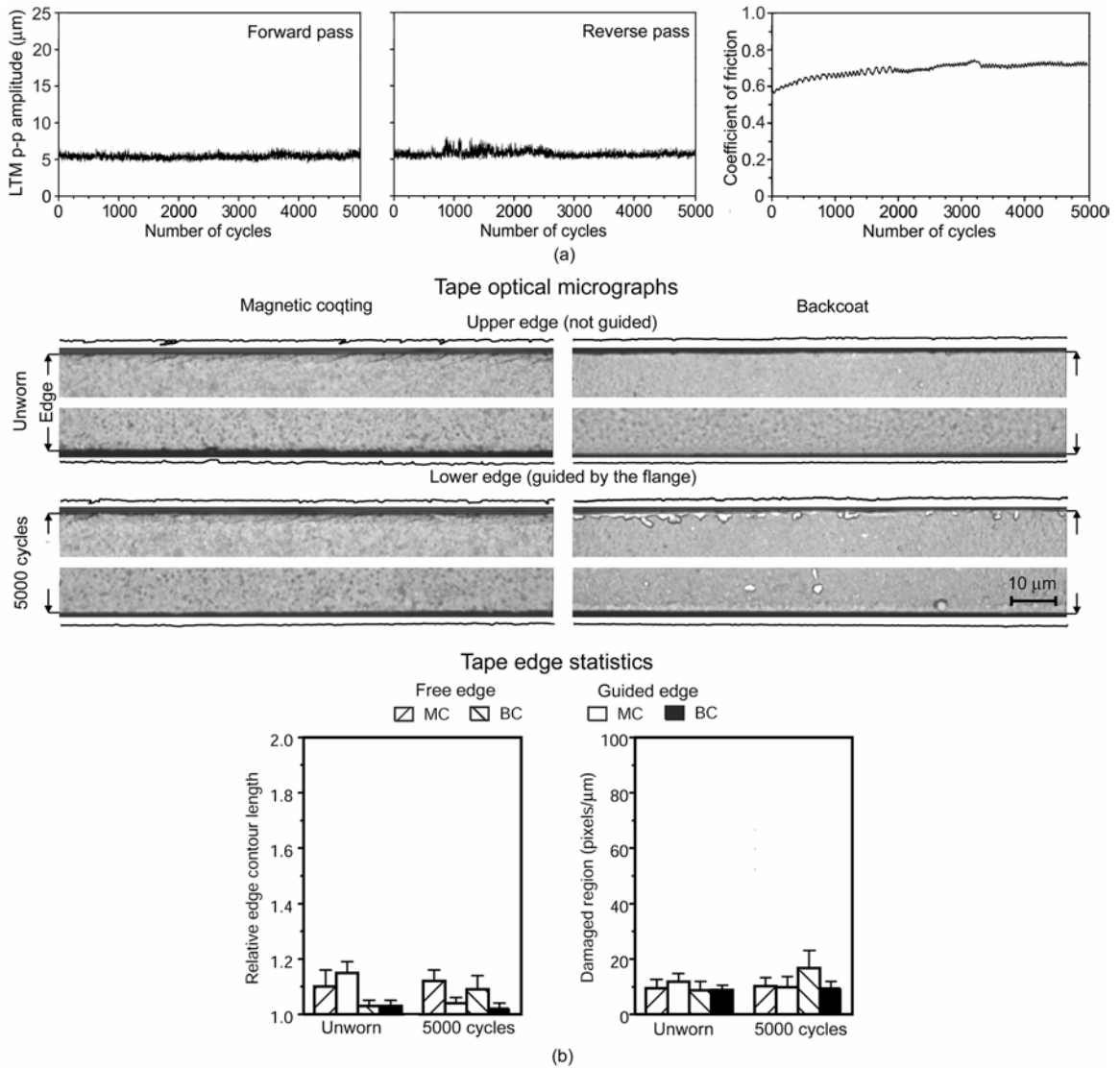


Figure 6.12: (a) Variation of lateral tape motion peak-to-peak amplitude as a function of number of cycles for thin media. (b) Tape edge statistics. Optical micrographs of 112 μm along length (640 pixels) and 11.2 μm along width (64 pixels) were analyzed. MC - magnetic coating, BC - backcoat.

cracks and tears can be identified on the magnetic coating at the upper (not guided) edge for the unworn and worn tape, which implies that no damage occurred after use in the tape drive. The edge contour length of the magnetic coating at the lower (guided) edge decreased after 5000 cycles. The guided edge got smoothed after use in the tape drive. The backcoat at the upper edge experienced damage during the test, which we believe resulted from interaction with reel flanges.

6.4 Summary

LTM is lower for the tape drive with single flanged guides with porous air bearings as compared to that with dual flanged stationary guides.

Effect of tape path geometry (head zenith and wrap angles) on LTM and lateral force was studied. LTM decreases and lateral force increases with the head zenith increasing. The tape path geometry can be optimized to minimize lateral tape motion and increase media longevity.

Edge quality of a batch of commercial tapes was evaluated and quantified. There is variation in edge quality for tape samples from different cartridges. Low edge quality of the factory-slit media results in poor guiding in a drive and excessive damage during drive operation.

The effect of drive operating parameters (tension and speed) on LTM was studied during long term wear tests. Lateral tape motion remains low at moderate tape tension and speed. With either tension or speed increasing, staggered wraps in tape pack on a reel occur and LTM increases.

With the tape thickness decreasing LTM remains low.

CHAPTER 7

CONCLUSIONS

7.1 Kelvin Probe Microscopy measurements of surface potential change under wear at low loads

A Kelvin probe microscope (nano-Kelvin probe technique) was successfully employed for study of early stages of wear at ultralow loads on a variety of samples of different nature. Even in the case of “zero wear” (no measurable deformation of the surface), there can be a significant change in surface potential inside the wear mark. This allows for the study of the onset of wear in the ultralow wear regimes that is not possible with other techniques. We found that the technique allows only qualitative measurements of surface potential change.

Negative wear was registered for single crystal silicon (100) and single crystal silicon (100) lubricated with fully bonded Z-DOL at ultralow loads and low number of cycles. The initial surface potential change can result from removal of a thin contaminant layer, natural oxide or lubricant, during the few first wear cycles. Structural changes occurring beneath the surface due to subsurface fatigue wear are believed to be responsible for the subsequent potential change and Kelvin probe microscopy is sensitive to them. The results obtained for gold suggest the KPM is sensitive to the change of

material work function under plastic deformation. In the case of aluminum no significant trend in surface potential change is observed. This might be explained by the presence of a mechanically modified layer on the sample surface resulting from polishing. In the case of dielectrics, isolated surface charges and polarization dominate the surface potential components; therefore, this technique is not suitable for measurements of dielectrics.

The measurements were performed in ambient air and we can not exclude the possibility of production of chemical compounds by reaction with molecules in air on the sample surface, except for gold. Further research is required with controlled environmental conditions to obtain quantitative nano-Kelvin probe results.

7.2 Effect of operating environment on failure mechanism of a head-tape interface

Magnetic and tribological performance of the head-tape interface in a linear tape drive with a belt driven cartridge is the best at low temperature and low relative humidity. Increase in both temperature and humidity results in performance degradation with the worst performance at the highest temperature. High humidity results in formation of meniscus bridges and hydrolytic binder degradation after sliding for several days, which is responsible for high friction and wear. High temperature results in binder softening and hydrolytic degradation at high humidity, which is responsible for high friction and wear.

7.3 Effect of particulate contamination on pole tip recession

The results of the study support the notion that three-body abrasion is the cause of pole tip recession (PTR) in tape heads. The experimental studies with the controlled injection of three-body particles into the head-tape interface has shown that PTR increases with increases in one of the following: particle concentration, size, and

hardness. The experimental results agree well with the predictions of the analytical model for the micro/nano-scale differential wear.

The presence of a small amount of large particles at the head-tape interface can decrease PTR. High concentration of the large particles leads to continuous PTR growth. Small particles drastically accelerate PTR growth at the beginning of sliding and increase the recession at saturation.

7.4 Tape edge studies

A methodology has been developed for evaluation of magnetic tape edge quality. The proposed methodology allows quantitative evaluation of edge damage. The measures of the tape edge quality are the relative edge contour length and the damaged region near tape edge (the number pixels of the per unit length).

Using the methodology developed, it has been established that factory-slit edges are imperfect and that the two edges differ from each other. The difference in stress distribution for the two edges during tape slitting governs the formation of two different edges. Cracking of magnetic coating at one edge occurs during manufacturing.

During normal drive operation edge quality degrades and one of the tape edges is prone to produce more debris than the other. A possible mechanism of the tape edge wear under normal drive operation has been proposed. Cross-section of both edges gets smoothed after use in tape drive with dual flanged stationary guides. Chunks of magnetic coating are removed at the edges. Continuous sliding results in plastic flow of material from the top of the cross-section to tape sides. This material forms a ridge over backcoat at one edge. The ridge partially tears during sliding and debris particles are formed.

Edge quality of a batch of commercial tapes was evaluated and quantified. There is variation in edge quality for tape samples from different cartridges. Low edge quality of the factory-slit media results in poor guiding in a drive and excessive damage during drive operation.

LTM is lower for the tape drive with single flanged guides with porous air bearings as compared to that with dual flanged stationary guides.

For the tape drive with single flanged guides with porous air bearings the effect of head zenith and wrap angles on LTM and lateral force was studied. LTM decreases and lateral force increases with the head zenith increasing. The tape path geometry can be optimized to minimize lateral tape motion and increase media longevity.

The effect of drive operating parameters (tension and speed) in tape drive with single flanged guides with porous air bearings on LTM was studied during long term wear tests. Lateral tape motion remains low at moderate tape tension and speed. With either tension or speed increasing, staggered wraps in tape pack on a reel occur and LTM increases. With the tape thickness decreasing LTM remains low.

REFERENCES

- Anderson, R. M. and Bhushan, B. (1996), "Concurrent Measurement of In Situ Friction Force and Head Signal Amplitude During Dropouts in Rotary Head Tape Drives," *Wear*, **202**, 35-49.
- Anderson, R. M. and Bhushan, B. (1997), "Effect of Environment on Dropouts in Rotary-Head Tape Drives," *Proc. Inst. Mech. Eng., Part J: J. Eng. Tribol.*, **211**, 349-363.
- Baumgärtner, H. and Liess, H. D. (1988), "Micro Kelvin Probe for Local Work-Function Measurements," *Rev. Sci. Instrum.*, **59**, 802-805.
- Bhushan, B. (1996), *Tribology and Mechanics of Magnetic Storage Devices*, 2nd Edition, Springer, New York.
- Bhushan, B. (1999a), *Handbook of Micro/Nanotribology*, 2nd Ed., CRC, Boca Raton, FL.
- Bhushan, B. (1999b), *Principles and Applications of Tribology*, Wiley, New York.
- Bhushan, B. (2000), *Mechanics and Reliability of Flexible Magnetic Media*, 2nd Edition, Springer, New York, NY.
- Bhushan, B. and Hahn, F. W. (1995), "Stains on Magnetic Tape Heads," *Wear*, **184**, 193-202.
- Bhushan, B. and Koinkar, V. N. (1994), "Nanoindentation Hardness Measurements Using Atomic Force Microscopy," *Appl. Phys. Lett.*, **64**, 1653-1655.
- Bhushan, B. and Mokashi, P.S. (2001), "Effect of Cycling on Debris Propensity in a Linear Tape Transport," *J. Info. Storage Proc. Syst.*, **3**, 267-275.
- Bhushan, B. and Zhao, Z. (1999), "Macroscale and Microscale Tribological Studies of Molecularly Thick Boundary Layers of Perfluoropolyether Lubricants for Magnetic Thin-Film Rigid Disks," *J. Info. Storage Proc. Syst.*, **1**, 1-21.
- Bhushan, B., Chandra, S., and Smallen, M. (1999), "Analysis of Drive-Level Contaminant Particles," *J. Info. Storage Proc. Syst.*, **1**, 115-124.

Bhushan, B., Hinteregger, H.F., and Rogers, A. E. E. (1994), "Thermal Considerations for the Edge Guiding of Thin Magnetic Tape in a Longitudinal Tape Transport," *Wear*, **171**, 179-193.

Binggeli, M. and Mate, C. M. (1995), "Influence of Water Vapor on Nanotribology Studied by Friction Force Microscopy," *J. Vac. Sci. Technol.* **B13**, 1312-1315.

Binnig, G. and Rohrer, H. (1982), "Scanning Tunneling Microscopy," *Helv. Phys. Acta*, **55**, 726-735.

Bobji, M. S. and Bhushan, B. (2001), "In-Situ Microscopic Surface Characterization Studies of Polymeric Thin Films during Tensile Deformation Using Atomic Force Microscopy," *J. Mater. Res.*, **16**, 844-855.

Condon, E. U. and Odishaw, H. (1967), *Handbook of Physics*, 2nd Ed., McGraw-Hill, New York.

Devecchio, D. and Bhushan, B. (1998), "Use of a Nanoscale Kelvin Probe for Detecting Wear Precursors," *Rev. Sci. Instrum.*, **69**, 3618-3624.

Fawcett, F., Gviessen, R., Joss, W., Lee, M. J. G., and Perz, J. M. (1980), "The Effect of Strain on the Fermi Surfaces," In *Electrons at the Fermi Surfaces*, Ed. By M. Springford, Cambridge University Press, Cambridge, U.K.

Fomenko, V. S. (1966), *Handbook of Thermoionic Properties*, Plenum Press, NY.

Gavit, S.E. (1998), "Tape Transport Apparatus Incorporating Porous Air Bearings," US Patent No. 5,777,823, July 7.

Goldade, A. V. and Bhushan, B. (2002), "Effect of Operating Environment on Failure Mechanism of a Head-Tape Interface in a Linear Tape Drive with a Belt Driven Cartridge," *Proc. Inst. Mech. Eng., Part J: J. Eng. Tribol.*, **216**, 159-176.

Goldade, A. V. and Bhushan, B. (2003), "Measurement and Origin of Tape Edge Damage in a Linear Tape Drive," *Tribol. Lett.*, **14**, 167-180.

Handbook of Auger Electron Spectroscopy (1995), 3rd Ed., Physical Electronics, Inc., Eden Prairie, MN, P. 14.

Harrison, M. J. K., Sullivan, J. L., and Theunissen, G. S. A. M. (1998), "Pole Tip Recession in Sandwiched Heads Incorporating a Fetan Soft Magnetic Track," *Tribol. Int.*, **31**, 491-500.

Hempstock, M. S., Wild, M. A., and Sullivan, J. L. (2000), "Interactions at the Head-Tape Interface of a Linear Tape System," *Tribol. Int.*, **33**, 391-399.

- Hunter, S. J. and Bhushan, B. (2001), "Debris Propensity of Magnetic Metal Particle Tapes," *J. Info. Storage Proc. Syst.*, **3**, 143-159.
- Jacobs, H. O., Knapp, H. F., Müller S., and Stemmer, A. (1997), "Surface Potential Mapping: A Qualitative Material Contrast in SPM," *Ultramicroscopy*, **69**, 39-49.
- Jacobs, H. O., Leuchtmann, P., Homan, O. J., and Stemmer, A. (1998), "Resolution and Contrast in Kelvin Probe Force Microscopy," *J. Appl. Phys.*, **84**, 1168-1173.
- Kattner, M. and Bhushan, B. (2000a), "Analysis of Stain Formation and Wear Mechanisms in a Linear Tape Drive," *Proc. Inst. Mech. Eng., Part J: J. Eng. Tribol.*, **214**, 561-581.
- Kattner, M. and Bhushan, B. (2000b), "Analysis of Stain Formation and Wear Mechanisms of MR Heads and MP Tape in a Linear Tape Drive," *J. Info. Storage Proc. Syst.*, **2**, 193-205.
- Kelvin, L., Fitzgerald, G. F., and Lassabatere, L. (1898), *Philos. Mag.*, **46**, 80.
- Li, X. and Bhushan, B. (1997), "Micromechanical Characterization of Magnetic Tapes," *IEEE Trans. Magn.*, **33**, 3208-3210.
- Li, X. and Bhushan, B. (2001), "Micro/Nanomechanical and Tribological Studies of Bulk and Thin-Film Materials Used in Magnetic Recording Heads," *Thin Solid Films*, **398-399**, 313-319.
- Luk, A. and Bhushan, B. (2001), "Durability and Failure Mechanisms of Digital Tapes in a Rotary Tape Drive," *Proc. Inst. Mech. Eng., Part J: J. Eng. Tribol.*, **215**, 77-101.
- Ma, T., Bhushan, B., Murooka, H., Kobayashi, I., and Osawa, T. (2002), "A Novel Technique to Measure the Poisson's Ratio and Submicron Lateral Dimensional Changes of Ultrathin Polymeric Films," *Rev. Sci. Instrum.*, **73**, 1813-1820.
- Martin, Y., Abraham, D. W., and Wickramasinghe, H. K. (1988), "High-Resolution Capacitance Measurement and Potentiometry by Force Microscopy," *Appl. Phys. Lett.*, **52**, 1103-1105.
- Michels, W. C., Correll, M., and Patterson, A. L. (1968), *Foundations of Physics*, D. Van Nostrand Company, Inc., New York.
- Nonnenmacher, M., O'Boyle, M. P., and Wickramasinghe, H. K. (1991), "Kelvin Probe Force Microscopy," *Appl. Phys. Lett.*, **58**, 2921-2923.
- Novotny, V. J., Karis, T. E., and Whitefield, R. J. (1997), "Surface Potential and Magnetic Recording Media Tribology," *Trib. Trans.*, **40**, 69-74.

- Patton, S. T. and Bhushan, B. (1996), "Environmental Effects on the Pause Mode Performance of Metal-Evaporated and Metal-Particle Tapes," *J. App. Phys.*, **79**, 5802-5804.
- Patton, S. T. and Bhushan, B. (1997a), "Friction, Wear and Magnetic Performance of Metal Evaporated and Particulate Magnetic Tapes," *Proc. Inst. Mech. Eng., Part J: J. Eng. Tribol.*, **211**, 327-348.
- Patton, S.T. and Bhushan, B. (1997b), "Environmental Effects on the Streaming Mode Performance of Metal Evaporated and Metal Particle Tapes," *IEEE Trans. Magn.*, **33**, 2513-2530.
- Rienau, J. (1979), *Techniques for Slitting and Winding*, John Dusenbery, Randolph, NJ.
- Sarid, D. (1994), *Scanning Force Microscopy with Applications to Electric, Magnetic and Atomic Forces*, Oxford University Press, New York.
- Scott, W. W. and Bhushan, B. (1999), "Pole Tip Recession in Linear Tape Heads: Measurement Technique and Influence of Head Materials, Tape Speed and Tape Tension," *Proc. Instn. Mech. Eng., Part J: J. Eng. Tribol.*, **213**, 139-150.
- Scott, W. W. and Bhushan B. (2000), "Loose Debris and Head Stain Generation and Pole Tip Recession in Modern Tape Drives: A Critical Review," *J. Info. Storage Proc. Syst.*, **2**, 221-254.
- Scott, W.W. and Bhushan, B. (2002), "Micro/Nano-Scale Differential Wear of Multiphase Materials: Pole Tip Recession in Magnetic-Tape Heads," *Wear*, **252**, 103-122.
- Scott, W. W. and Bhushan, B. (2003), "Measurement and Prediction of Tape Cupping under Mechanical and Hygrothermal Loads and Its Influence on Debris Generation in Linear Tape Drives," *ASME J. Tribol.*, **125**, 364-376.
- Scott, W. W., Bhushan, B., and Lakshmikumar, A. V. (2001), "Effect of Magnetic-Head Slot Orientation on Pole Tip Recession and Debris Generation in Linear Tape Drives," *Tribol. Trans.*, **44**, 263-269.
- Stahl, K. J. and Gavit, S.E. (2001), "Flying and Tracking Stability of Porous Air Bearing Systems," *J. Info. Storage Proc. Syst.*, **3**, 3-10.
- Taylor, R., Strahle, P., Stahl, J., Dugas, M., and Talke, F. (2000), "Measurement of Cross-Talk Motion of Magnetic Tapes," *J. Info. Storage Proc. Syst.*, **2**, 255-2262.
- Topoleski, J. J. and Bhushan, B. (2000), "Qualitative and Quantitative Evaluation of the Quality of Factory-Slit Magnetic Tape Edges," *J. Info. Storage Proc. Syst.*, **2**, 109-116.

- Tsuchiya, T. and Bhushan, B. (1995), "Metal Core Recession and Head Stain Studies of MIG Heads Sliding against Cobalt-Doped Gamma Iron Oxide and Metal Particle Tapes," Tribol. Trans., **38**, 941-949.
- Wallace, R. L. (1951), "The Reproduction of Magnetically Recorded Signals," The Bell System Tech. J., **30**, 1145-1173.
- Weaver, J. M. R. and Abraham, D. W. (1991), "High Resolution Atomic Force Microscopy Potentiometry," J. Vac. Sci. Tech., **B9**, 1559-1561.
- Woodruff, D. P. and Delchar, T. A. (1994), Modern Techniques of Surface Science, 2nd Ed., Cambridge University Press, Cambridge, U.K.
- Xie, Y. and Bhushan, B. (1996), "Fundamental Wear Studies with Magnetic Particles and Head Cleaning Agents Used in Magnetic Tapes," Wear, **202**, 3-16.
- Xu, J. and Bhushan, B. (1998), "Pole Tip Recession Studies of Thin-Film Rigid Disk Head Sliders I. Mechanisms of Pole Tip Recession Growth," Wear, **219**, 16-29.
- Yokoyama, H. and Inoue, T. (1994), "Scanning Maxwell Stress Microscope for Nanometer-Scale Surface Electrostatic Imaging of Thin Films," Thin Solid Films, **242**, 33-39.
- Zanoria, E. S., Danyluk, S., and Zharin, A. L. (1995), "Kelvin Probe Measurements of Wear of a Magnetic Hard Disk," Advances In Information Storage And Processing Systems, ISPS, 1, ASME, New York, 49-55.
- Zharin, A. L. and Rigney, D. A. (1998), "Application of the Contact Potential Difference Technique for On-Line Rubbing Surface Monitoring," Trib. Lett., **4**, 205-213.
- Zharin, A. L., Fishbein, E. I., and Shipitsa, N. A. (1995), "Effect of Contact Deformation upon Surface Electron Work Function," Journal of Friction and Wear," **16**, 66-78.
- Zisman, W. A. (1932), Rev. Sci. Instrum., **3**, 367.

APPENDIX A

TAPE EDGE QUALITY MEASUREMENT METHODOLOGY

Methodology to measure the quality of the magnetic tape edges is based on characterization of the two tape edges by means of optical microscopy, atomic force microscopy (AFM) and scanning electron microscopy (SEM). Figure A.1 shows the definition of the views to be examined. Optical microscopy is used to image the magnetic coating side and backcoat side at the tape edges and these images are used to quantify the quality of the tape edges using an image analysis technique. AFM is used to analyze single tape layer (edge view) to obtain height information. SEM is used to analyze the edges at high resolution to learn about deformation mode. Figure A.2 shows a sample set of optical micrographs, AFM maps and SEM images, which completely characterize tape edges.

For optical imaging, tape samples cut into 50 mm strips are mounted on a glass microscope slide by using double-sided adhesive tape. Tape is placed such that its edge is approximately 0.3 mm from the adhesive edge of the mounting. Care has to be taken to assure flatness of the tape sample areas close to the edge. For AFM mapping, maps of the edge view can be taken in contact mode. For mapping, a 50 mm piece of tape is pinched between two glass microscope slides with the edge sticking out by about 0.3-0.5 mm over the slides and placed into the AFM. For SEM analysis, 5-10 mm long tape strips are

Definition of views

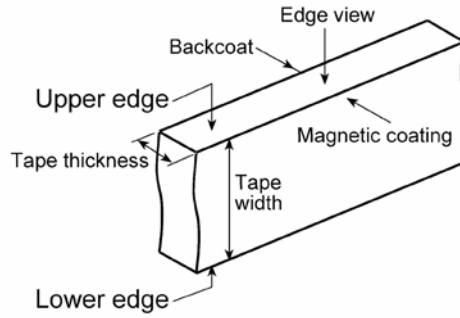


Figure A.1: Definition of tape edge views.

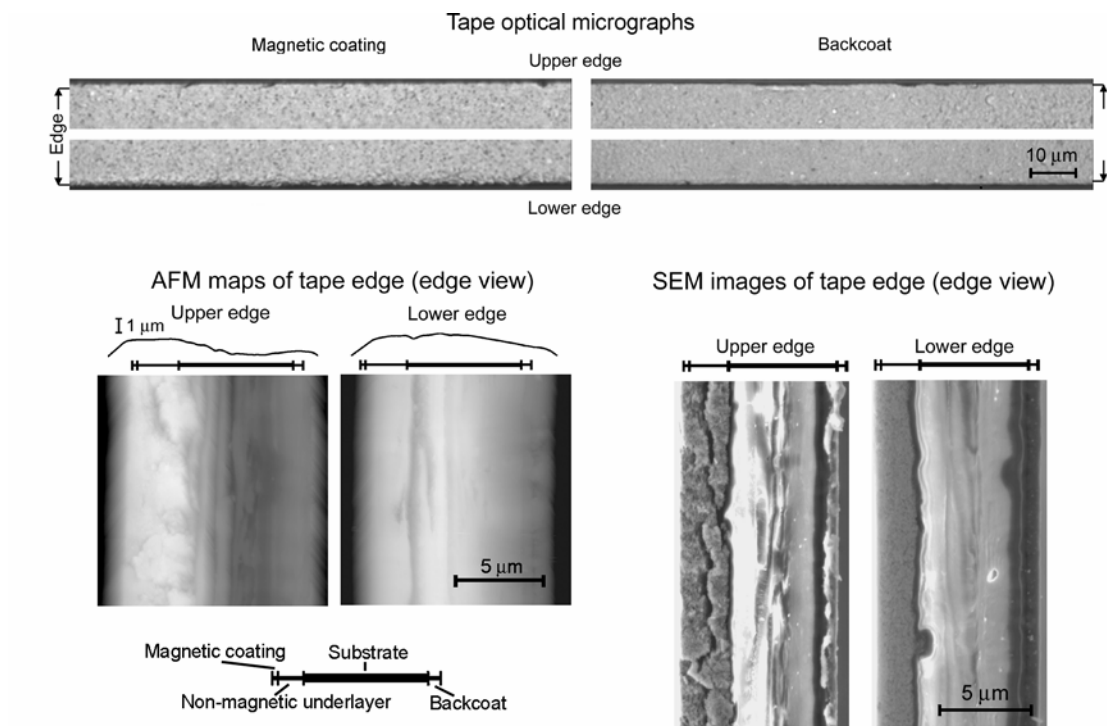


Figure A.2: Sample optical micrographs, AFM maps and SEM images of tape edges.

mounted on a sample holder using conducting adhesive such that the tape edge is sticking over the edge of the holder by 0.3-0.5 mm.

The measures of the tape edge quality are the relative edge contour length and the damaged region near tape edge in pixels per unit length. Optical microscopy is used to photograph magnetic coating and backcoat at the tape edge and these images are analyzed to measure the edge quality of magnetic coating and backcoat. It is the tape edge view which comes into contact with the guides and is the key to proper guiding. It has been observed that there is a good relationship between the quality of the tape edge at the magnetic coating and backcoat sides and the edge view. Since it is easier to measure edge quality using optical microscopy, this technique is recommended. To perform the measurements Adobe Photoshop (Adobe Systems Inc., version 4.0 or higher for IBM PC) and Scion Image (Scion Corporation, version 3.0 or higher for IBM PC) software are required. An optical microscope equipped with digital camera and frame grabber and capable of capturing images at 500x-700x magnification is required.

For further illustration of the technique, Figure A.3 (a) shows an optical image of magnetic coating at the lower edge for the unworn tape. By increasing the brightness of the image using Adobe Photoshop an overexposed image is obtained. There is a distinct border in the overexposed image between the bright white (tape surface) and gray (sample mount) areas, which represents edge contour. With the use of Adobe Photoshop, this border is outlined, so that the line constituting the border (edge contour) is continuous and one pixel wide and the length of the edge contour is calculated using Scion Image software. It is also observed from Fig. A.3 (a), that damaged region (cracks and tears) near the tape edge can be easily identified from the overexposed image as dark

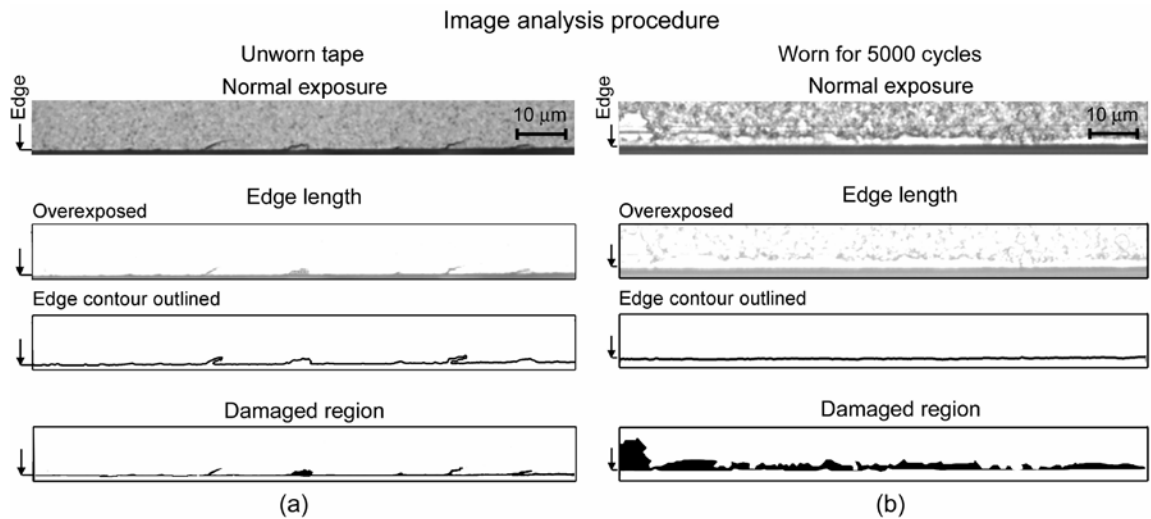


Figure A.3: Sample optical micrographs illustrating edge quality measurement technique: (a) unworn tape and (b) tape worn for 5000 cycles.

regions. By applying threshold to the image in Scion Image software (Fig. A.3 (a), bottom image) these areas (damaged region) can be selected and their area can be calculated. However, using threshold option brings in some subjectivity to the measurements. It should also be mentioned, that it is not always possible to identify damaged region by applying the threshold. This is usually true for the tape used in a tape drive. Figure A.3 (b) shows the backcoat at the lower tape edge of the tape sample run for 5000 cycles in a tape drive. In this case the damaged region (Fig. A.3 (b), bottom) should be selected by manually outlining it in the image with normal exposure using free lasso tool option in Adobe Photoshop, prior to applying threshold in the Scion Image software.

To measure the relative edge contour length and damaged region, perform the following steps.

- Mount 50 mm piece of tape on microscope glass slide.
- Capture ten optical images of each view (a total of 40 images for one tape sample) of the tape edges at normal exposure and magnification of 500x-700x. Adjust brightness of each image by using Adobe Photoshop and save overexposed images in TIFF format.
- Using Adobe Photoshop crop the images to the desired size (10:1 or 5:1 length to width ratio) and select the border between the bright white area (tape surface) and gray area (glass slide) and made the border one pixel wide. Save as new files in TIFF format.
- Using Scion Image software, open the file and set the scale. Select “Perimeter/Length” to be calculated. Perform the measurements and normalize the measured edge contour length with the length of the optical micrograph to obtain relative edge contour length for each view.
- Using Scion Image software, open the overexposed image and set the scale. Select number of pixels to be calculated. Apply threshold to the image and calculate the area of the damaged region near the tape edge. In case the damaged region can not be identified in the overexposed image, manually outline it in the image with normal exposure using Adobe Photoshop and calculate the area using Scion Image software. Divide the area of the damaged region by the length of the optical micrograph to obtain the number in pixels per unit length units.

Figure A.4 presents a sample of the tape edge statistics for two tapes with different edge quality.

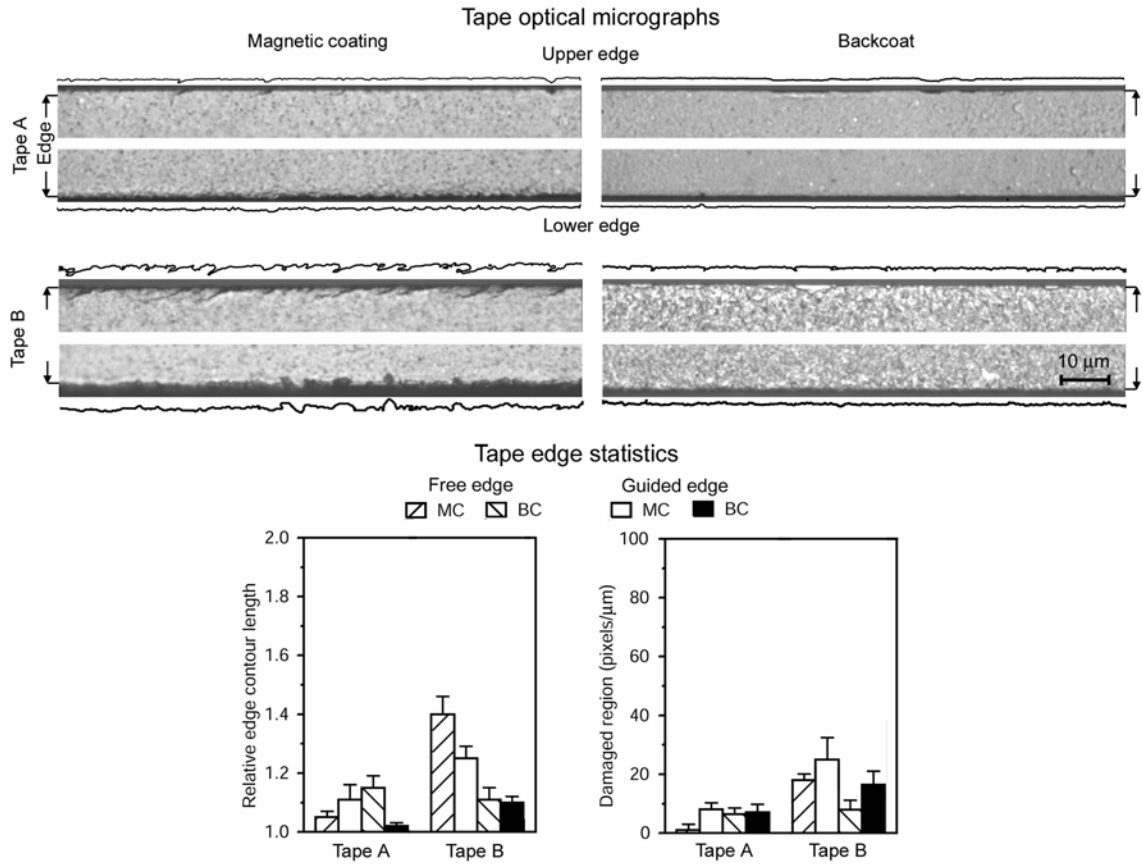


Figure A.4: Sample optical micrographs of tape edges and tape edge statistics for two tapes with different edge quality.

APPENDIX B

TAPE CUPPING MEASUREMENTS

Tape cupping is the natural tendency of the tape to curl about an axis perpendicular to the direction of travel along the tape width [Bhushan, 2000; Scott and Bhushan, 2003]. Prior to measurements, 1 m long tape strips should be conditioned for 24 hours at ambient conditions (typically 22 °C and 45 % RH) by hanging them so that surfaces of both magnetic coating and backcoat are freely exposed to the test environment. Residual cupping, i.e., cupping at zero tension, is measured as follows. A 200 mm long tape sample is cut from the center portion of the conditioned tape and placed on an optically flat surface (microscope slide) under the microscope lens with the magnetic coating facing the lens. The measurement is completed by bringing the edge of the tape into focus, and then traversing across the tape width in 1-mm increments while the focus is adjusted and the fine focus scale reading is recorded. The microscope should be calibrated such that to know the vertical depth for one full revolution of fine focus. Care must be taken to assure that the microscope slide is not tilted and both upper and lower edges of the tape touch the slide surface while measurements are performed.

Cupping of the tapes with tension applied can be measured as follows. The head should be mounted in the middle of a rectangular plate and placed under the microscope

lens. The length of the plate should be selected to provide a proper wrap angle for the tape over the head. The tape is put on the head with the backcoat facing the microscope lens and two ends hanging over the ends of the plate. Dead weights are clamped to the tape ends to provide the desired tape tension. The cupping measurements are then made over the area of the head-tape contact using an optical microscope as described earlier for the residual cupping measurements.

Tape cupping for each sample should be calculated by averaging the results of five measurements performed at a distance of 20 mm from each other over tape length. Figure B.1 shows sample cupping profiles for two tapes at 0 N applied tension (residual cupping) and cupping of the one of the tapes under tension of 1 N supported over a head with 21° wrap angle.

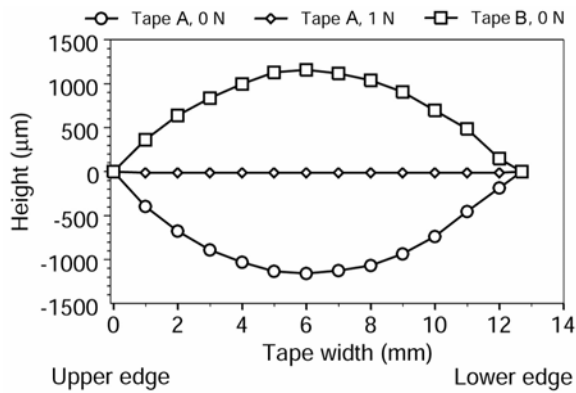


Figure B.1 Sample cupping profiles. Magnetic coating is at the bottom.